

APPROVAL SHEET

Title of Dissertation: Analysis of Stability and Noise in Passively Modelocked
Comb Lasers

Name of Candidate: Shaokang Wang
Doctor of Philosophy, 2008

Dissertation and Abstract Approved: Curtis R. Menyuk
Curtis R. Menyuk
Professor
Computer Science and Electrical Engineering

Date Approved: July 5, 2018

ABSTRACT

Title of dissertation: Analysis of Stability and Noise in
Passively Modelocked Comb Lasers

Shaokang Wang, Doctor of Philosophy, 2018

Dissertation directed by: Curtis R. Menyuk, Professor,
Department of Computer Science and Electrical
Engineering, University of Maryland, Baltimore County

The search for robust, low-noise modelocked comb sources has attracted significant attention during the last two decades. Passively modelocked fiber lasers are among the most attractive comb sources. The most important design problems for a passively modelocked laser include: (1) finding a region in the laser's adjustable parameter space where it operates stably, (2) optimizing the pulse profile within that region, and (3) lowering the noise level. Adjustable parameters will typically include the cavity length, the pump power, and the amplifier gain, which may be a function of the pump power, the pump wavelength, and both the material and geometry of the gain medium.

There are two basic computational approaches for modeling passively modelocked laser systems: the evolutionary approach and the dynamical approach. In the evolutionary approach, which replicates the physical behavior of the laser, one launches light into the simulated laser and follows it for many round trips in the laser. If one obtains a stationary or periodically-stationary modelocked pulse, the laser is deemed stable and, if no such pulse is found, the laser is deemed unstable. The effect of noise can be studied by using a random number generator to add computational noise. In the dynamical approach, one first obtains a single modelocked pulse solution either analytically or by using the evolutionary approach. Next, one finds the pulse parameters as the laser parameters vary by solving a root-finding algorithm. One then linearizes the evolution equations about the steady-state solution and determines the eigenvalues of the linearized equation, which we refer to as

the equation's dynamical spectrum. If any eigenvalue has a positive real part, then the modelocked pulse is unstable. The effect of noise can be determined by calculating the noise that enters each of the modes in the dynamical spectrum, whose amplitudes are described by either a Langevin process or a random walk process.

The evolutionary approach is intuitive and straightforward to program, and it is widely used. However, it is computationally time-consuming to determine the stable operating regions and can give ambiguous results near a stability boundary. When evaluating the noise levels, Monte Carlo simulations, which are based upon the evolutionary approach, are often prohibitively expensive computationally. By comparison, the dynamical approach is more difficult to program, but it is computationally rapid, yields unambiguous results for the stability, and avoids computationally expensive Monte Carlo simulations. The two approaches are complementary to each other. However, the dynamical approach can be a powerful tool for system design and optimization and has historically been under-utilized.

In this dissertation, we discuss the dynamical approach that we have developed for design and optimization of passively modelocked laser systems. This approach provides deep insights into the instability mechanisms of the laser that impact or limit modelocking, and makes it possible to rapidly and unambiguously map out the regions of stable operation in a large parameter space. For a given system setup, we can calculate the noise level in the laser cavity within minutes on a desktop computer.

Compared to Monte Carlo simulations, we will show that the dynamical approach improves the computational efficiency by more than three orders of magnitude. We will apply the dynamical approach to a laser with a fast saturable absorber and to a laser with a slow saturable absorber. We apply our model of a laser with a slow saturable absorber to a fiber comb laser with a semiconductor absorbing mirror (SESAM) that was developed at National Institute of Standards and Technology (NIST), Boulder, CO. We optimize its parameters and show that it is possible to increase its output power and bandwidth while lowering the pump power that is needed.

ANALYSIS OF STABILITY AND NOISE IN
PASSIVELY MODELOCKED COMB LASERS

by

Shaokang (Jerry) Wang

Dissertation submitted to the Faculty of the Graduate School of the
University of Maryland, Baltimore County in partial fulfillment
of the requirements for the degree of
Doctor of Philosophy
2018

Advisory Committee:
Professor Curtis R. Menyuk, Chair/Advisor
Dr. Thomas F. Carruthers
Professor Yan Li
Professor Yanhua Shih
Professor Andrei Draganescu
Professor Anthony M. Johnson

© Copyright by
Shaokang Wang
2018

Acknowledgments

First of all, I could not have achieved what I have today without my research advisor, Professor Menyuk, who has given me an invaluable life experience. His intelligence, determination and passion to explore the truth, his persistent guidance, and his motivation have been invaluable lessons to a junior researcher like myself. It has been an honor to work with him and learn from him.

Along the way, I have another two individuals who merit particular thanks: Dr. Andrew Docherty and Dr. Brian S. Marks. They have been my mentors in scientific computing, which is the foundation of my Ph.D research and also probably my future career.

I would also like to express special thanks to our research collaborators at the Fiber Sources and Applications Group at National Institute of Standard and Technology, Boulder, CO: Dr. Nathan R. Newbury, Dr. Ian Coddington, Dr. Laura Sinclair, and Dr. Stefan Droste. I thank them for bringing up interesting questions, helping my colleagues and I to validate our models, and ensuring that our computational tools answer the most important design questions.

In addition, my colleagues at the Technology Research Center at UMBC have accompanied my graduate life in many ways and deserve mention.

I owe my deepest thanks to my family: my mother, my father, my sister, my two baby nieces, and my aunt and uncle, who have always supported me throughout my long stay at UMBC. I deeply appreciate their love and generosity—and at the

same time, feel guilty that I have not spent more time with them. Their well-being is the impetus behind and the goal of both my career and my life.

To my loved one: Life has always been unpredictable. But I know that I can always count on you being there as my anchor. I cannot possibly be here without your company. Thank you for being there for me every step of the way.

Lastly, “Was mich nicht umbringt, macht mich stärker.”

Contents

List of Figures	vi
1 Introduction	1
1.1 Passively Modelocked Lasers	3
1.2 Saturable Absorption	5
1.3 Laser Models and Computational Approaches	7
1.4 Outline of the Dissertation	9
List of Abbreviations	1
2 Stability of Passively Modelocked Lasers with Fast Saturable Absorbers	11
2.1 The Cubic-Quintic Modelocking Equation	12
2.1.1 Finding a Pulse Solution	14
2.1.2 Linear Stability Analysis	15
2.1.3 Tracking Stability Boundaries	18
2.1.4 Stable Regions of the CQME	19
2.2 On the High-amplitude Solution	23
2.2.1 Appearance of New Discrete Modes	24
2.2.2 Stability Boundary of the Hopf Bifurcation	27
2.3 Agreement with Experiments	28
2.4 Comparison of Different Models of Fast Saturable Absorption	31
2.5 Summary	32
3 Modelocking with Slow Saturable Absorption	33
3.1 Modeling the Laser Cavity	35
3.1.1 Output Coupling	36
3.1.2 Single-mode fiber	38
3.1.3 Erbium-Doped Fiber	39
3.1.4 Semiconductor Saturable Absorption Mirror (SESAM)	40
3.2 Output of the Comb Laser	41
3.3 RF Spectrum Analysis	42
3.3.1 The Heterodyne Spectrum Analyzer	43
3.3.2 The output RF spectrum	47
3.4 Summary	48

4	Stability of Passively Modelocked Lasers with Slow Saturable Absorbers	50
4.1	An Averaged Model	51
4.2	Wake Mode Instability	54
4.3	Summary	60
5	Evaluating the Impact of Noise	62
5.1	The Dynamical Method	65
5.1.1	Discretization	66
5.1.2	Spectral Decomposition	67
5.1.3	Noise Evolution	68
5.1.4	Noise Impact on Statistical Quantities of Interest	70
5.2	Noise Level Evaluation and Computational Efficiency Tests	73
5.2.1	Calculation Methods	74
5.2.1.1	The Haus-Mecozzi Method	74
5.2.1.2	The Monte Carlo Simulation Method	77
5.2.1.3	The Dynamical Method	77
5.2.2	Application to Modelocked Systems	77
5.2.2.1	The Haus Modelocking Equation	78
5.2.2.2	The SESAM Laser	83
5.3	Conclusions	89
6	Laser Cavity Design Optimization	90
6.1	Optimizing the Laser Cavity	91
6.1.1	When $t_{oc} = 9\%$	94
6.1.1.1	Variation of Pulse Profiles When g_0 Changes	94
6.1.1.2	Variation of Pulse Profiles When β'' Changes	96
6.1.2	When t_{oc} Changes	98
6.1.2.1	Adjusting the Unsaturated Gain	99
6.1.2.2	Adjusting the Group Delay Dispersion	102
6.2	Validating the Optimization Study	106
6.3	Increasing the Power Efficiency	109
6.4	Conclusions	112
7	Conclusion	114
A	Variables	116
	Bibliography	123

List of Figures

1.1	An illustration of the output of a passively modelocked laser.	3
1.2	Illustration of gain and loss dynamics due to (a) a pulse train. The laser is assumed to include slow saturable gain and either (b) a fast saturable absorber or (c) a slow saturable absorber.	6
2.1	Illustration of the dynamical spectrum when the pulse solution of the modelocking equation is linearly stable.	17
2.2	Illustration of tracking the stability boundary of the continuous eigenmodes using boundary tracking algorithms. In this case, the most unstable continuous eigenmodes we track correspond to an eigenvalue λ that satisfies $\text{Re}(\lambda) = g - l$	18
2.3	The stability regions of the pulse solutions of the CQME.	20
2.4	The pulse solution profiles of the low-amplitude solution (LAS) and the high-amplitude solution (HAS) of the CQME with $(\sigma, \delta) = (0.004, 0.8036)$	22
2.5	Illustration of the emergence and destabilization of the corresponding eigenmodes of new discrete eigenvalues as δ grows: from (a) an edge bifurcation to (b) a Hopf bifurcation.	24
2.6	The eigenmodes corresponding to λ_e with $\sigma = 0.003$ and (a) $\delta = 9.509$, $\lambda_e = -0.40 + 1.05 \times 10^4 i$; (b) $\delta = 13$, $\lambda_e^* = (0.31 + 1.33i) \times 10^4$	25
2.7	Stability boundary of the high-amplitude solution due to the edge bifurcation as illustrated in Fig. 2.5.	27
2.8	Comparison of the computational stationary pulses with the experimental pulses using parameters in (a) set 1 [1,2] and (b) set 2 [3].	30
3.1	Illustration of the SESAM fiber laser.	34
3.2	Propagation of the modelocked pulse inside the laser cavity. The black dot indicates the location at which we compare the pulse profile to determine stability.	35
3.3	The allocation of the loss at the output coupler.	38
3.4	(a) The computational evolution of the stationary pulse, in which color indicates the pulse's amplitude; (b) the stable pulse's amplitude and phase in the time domain and the frequency domain, where $f = 0$ corresponds to $\lambda = 1570$ nm.	41

3.5	Illustration of unwrapping the optical field $u(t, T)$ to obtain $u_p(T)$ and $I(t)$, where T_w is the computational time window and T_R is the round trip time.	43
3.6	Illustration of a heterodyne spectrum analyzer.	44
3.7	Comparison of the experimentally-observed and the computationally-calculated RF spectrum. The agreement is excellent.	48
4.1	Starting from noise, the system of Eq. (1.1) evolves to a stable profile in the (a) time domain and (b) frequency domain, where $\tilde{u}(f) = \int_{-T_R/2}^{T_R/2} u(t) \exp(-2i\pi ft) dt$	53
4.2	The stationary pulse u_0 and the net gain, $G_n = \exp [g(u_0) - l - \rho n(t)]$, which exhibits an asymmetric profile due to the SESAM. A net gain window exists when $G_n > 1$	53
4.3	The evolution profile of the wake mode instability (a) in the time domain, and (b) in the frequency domain, (see Visualization 1), and the pulse amplitude profile at (c) $T = 823$, (d) $T = 948$, (e) $T = 1073$, and (f) $T = 1198$. The locations of profiles (c), (d), (e), and (f) are marked by white lines in (a).	55
4.4	The variation of the dynamical spectrum when the unsaturated gain g_0 increases from 1.90 to 2.70. We find that $\lambda_{w\pm} = -7.75 \times 10^{-4} \pm 0.352i$ when $g_0 = 7.74$ and $\lambda_{w\pm} = 9.09 \times 10^{-3} \pm 1.19i$ when $g_0 = 13.5$. The dashed arrows indicate how the spectrum shifts as g_0 increases from 7.74 to 13.5. The eigenvalue $\lambda_a < -0.90$ is not shown here.	57
4.5	Stability boundaries in the parameter space of the unsaturated gain g_0 and the group velocity dispersion β'' . The points (i) and (ii) indicates the cases $g_0 = 7.74$ and $g_0 = 13.5$, respectively, with $\beta'' = -0.0144 \text{ ps}^2$	59
4.6	The variation of the output power P_{out} and the sidebands' frequency offset f_{sb} as the unsaturated gain g_0 increases. The stationary pulse becomes unstable when $g_0 = 8.5$	60
5.1	Comparison between the Haus-Mecozzi and Monte Carlo methods, where $\sigma_w^2(T)$, $\sigma_{f_c}^2(T)$, and $\sigma_{t_c}^2(T)$ are propagation-dependent variances of the pulse energy w , central frequency f_c , and the central time t_c . The Haus-Mecozzi method results are from Eq. (5.38).	81
5.2	Noise spectra of (a) the energy jitter, (b) the frequency jitter, and (c) the timing phase jitter that we obtain from the Monte Carlo, Haus-Mecozzi, and dynamical methods. The agreement is excellent and the results in (c) agree with Fig. 1 in [4].	82
5.3	Comparison between the Haus-Mecozzi and Monte Carlo methods for the SESAM fiber laser, where $\sigma_w^2(T)$, $\sigma_{f_c}^2(T)$, and $\sigma_{t_c}^2(T)$ are propagation-dependent variances of the pulse energy Δw , central frequency Δf_c , and the central time Δt_c . We obtain the Haus-Mecozzi method results by substituting the computational stationary pulse solution parameter from Table 5.3 into Eq. (5.38).	85

5.4	The power spectral density of (a) the energy jitter, (b) the frequency jitter, and (c) the timing phase jitter that we obtain from the Monte Carlo, Haus-Mecozzi, and dynamical methods.	87
6.1	When the output coupling ratio $t_{oc} = 9\%$, the stability boundaries in the parameter space of the unsaturated gain g_0 and the group delay dispersion β'' . The purple dot indicates the cases $g_0 = 7.74$ and $\beta'' = -0.0144 \text{ ps}^2$ which corresponds to the experimental pulse as $P_{\text{pump}} = 237 \text{ mW}$. In Sec. 6.1.1, we perform parameter studies along the directions as indicated by the blue arrows.	92
6.2	An illustration of the parameter space and an example of the search directions that we used to perform the optimization study in Sec. 6.1.2.	93
6.3	(a) The intra-cavity pulse energy w_0 and (b) the FWHM pulse duration τ_p as a function of the unsaturated gain g_0 , for three values of group delay dispersion β''	95
6.4	Variation of the wake mode sidebands when the unsaturated gain g_0 increases with $\beta'' = -0.015 \text{ ps}^2$	96
6.5	The intra-cavity pulse energy w_0 and the FWHM pulse duration τ_p as a function of the group delay dispersion β'' with $g_0 = 7.74$	97
6.6	Variation of the wake mode sidebands when the group delay dispersion increases with $g_0 = 7.74$	97
6.7	The output pulse profiles when the unsaturated gain g_0 varies for given values of the group delay dispersion β'' and the output coupling ratio t_{oc} . We set the output coupling ratio t_{oc} equal to (a) 10%, (b) 20%, (c) 40%, and (d) 60%. The black dots indicate the onset of the wake mode instability. The magenta and the green circles correspond respectively to the reference pulse and Pulse 1, which we show in Fig. 6.9.	100
6.8	The energy PSD when g_0 , β'' , and t_{oc} vary. The green line in (b) shows the energy PSD that corresponds to Pulse 1, shown in Fig. 6.9.	101
6.9	The optimal pulse profiles that we find using the averaged model.	103
6.10	Variation of the stable output pulse profile when the group delay dispersion β'' , approaches zero for given values of unsaturated gain g_0 and output coupling ratio t_{oc} : (a) $t_{oc} = 10\%$, (b) $t_{oc} = 20\%$, (c) $t_{oc} = 40\%$, and (d) $t_{oc} = 60\%$. The black dots indicate the onset of the wake mode instability. The blue circles correspond to Pulse 2, shown in Fig. 6.9.	104
6.11	Variation of the wake mode sidebands when the output coupling ratio t_{out} changes. The blue line in (b) shows the energy jitter profile corresponding to Pulse 2, shown in Fig. 6.9.	105

6.12	(a) The calculated optimal pulses and (b) their RF spectra using the lumped model. The reference pulse and its RF spectrum are consistent with our results in Sec. 6.1. In order to provide sufficient cavity gain, we set the doping concentration N_e of the erbium fiber equal to $5.21 \times 10^{25} \text{ cm}^{-3}$ when $\beta_2 = -0.0534 \text{ ps}^2$ and $\beta_2 = -0.0730 \text{ ps}^2$	108
6.13	The calculated average output power P_{out} and power efficiency η_{out} with different levels of pump power P_{pump} and output coupling ratios t_{oc} , where the lengths of erbium-doped fiber $L_{\text{EDF}} = 15.0 \text{ cm}$ in (a) and (b), $L_{\text{EDF}} = 25.0 \text{ cm}$ in (c) and (d), and $L_{\text{EDF}} = 32.5 \text{ cm}$ in (e) and (f).	111

CHAPTER 1

Introduction

Since their invention in the 1960s, passively modelocked lasers have played an important role in a wide range of fields [5, 6]. The scope of potential applications has increased drastically in the past two decades and spans commercial, basic science, and military applications. These applications include particle accelerators, light detection and ranging, optical coherence tomography and other medical applications, spectroscopy and chemical analysis, micromachining, communications, and the generation and transfer of highly accurate time and frequency. Compact, robust, and inexpensive modelocked sources are in high demand, which has led to the development of fiber laser sources that are competitive with solid state lasers for many applications.

Despite their importance, computational tools that are sufficiently accurate to do *a priori* design of passively modelocked fiber lasers have not received the attention that they deserve. Most theoretical studies either use computationally time-consuming solutions of the evolution equations [7, 8] or highly-approximate analytical models [4, 9]. These approaches are intuitive and straightforward. However,

they are inadequate to address the key problems of determining the laser parameter ranges within which a comb exists stably, understanding the physical sources of instability, finding the limits on peak pulse powers and durations, and calculating the power spectral density over a broad parameter range to optimize the system performance. One goal of this dissertation is to describe the computational tools that we have developed [10, 11] and which are sufficiently accurate and efficient for *a priori* design.

There are three basic tasks in designing a passively modelocked laser. The first task is to determine the parameter ranges where stable pulses exist within the set of the laser's adjustable parameters. Adjustable parameters typically include the length of the gain medium, the output coupling ratio, and the magnitude of the chromatic dispersion. More than one region of stable operation can exist, and they can overlap. If two regions overlap, then stable modelocked pulses with different pulse parameters can be found with the same laser parameters. Which pulse appears depends on the history of the pulse generation. Once a stable modelocked pulse has been found, the second task is to determine the impact of noise on the pulse. Amplified spontaneous emission noise from the gain medium will always be present. This noise will lead to fluctuations in the power spectral density of the pulse's amplitude and phase. It is usually desirable to minimize this noise. The third task is to optimize the pulse parameters by adjusting the laser parameters. The appropriate metric for optimization depends on the application. In some cases, high power is desirable. In other cases, low noise is desirable.

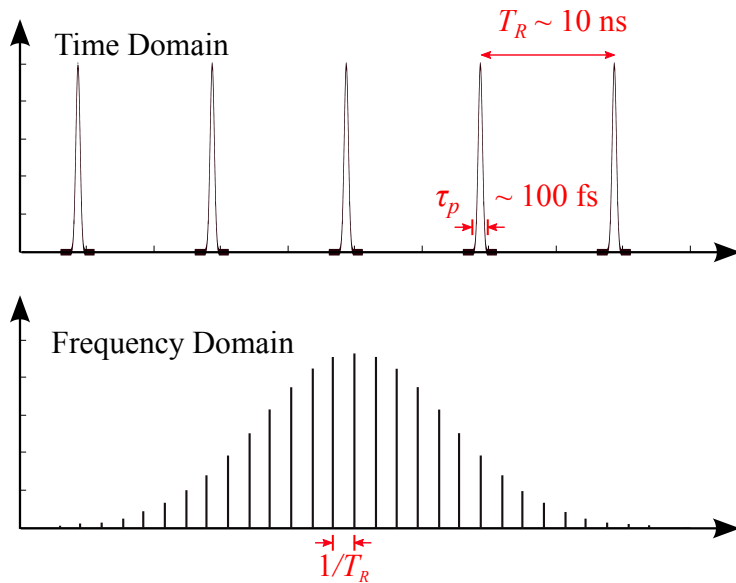


Figure 1.1: An illustration of the output of a passively modelocked laser.

1.1 Passively Modelocked Lasers

Passively modelocked lasers are attractive sources of ultra-short, high-energy, and stable optical pulses. In Fig. 1.1, we show a schematic illustration of the output of a passively modelocked laser. The duration of the output modelocked pulses τ_p are typically on the order of 100 fs, and the time interval between two consecutive pulses, which equals the round-trip time of the laser T_R , is typically on the order of 10 ns. Passively modelocked lasers have been important source of frequency combs since the 1990s [12, 13]. In the frequency domain, the output spectrum consist of a set of comb teeth [14]. The envelope of the comb teeth is the Fourier transform of a single output pulse. When there only exists a single pulse in each round trip, the separation of two successive comb teeth is the free spectral range, which equals

$1/T_R$.

The Haus modelocking equation (HME) is one of the oldest and most widely used models for passively modelocked lasers. The HME is an averaged model in which all cavity components that contribute to modelocking are homogenized over a single round trip. The HME may be written as

$$\frac{\partial u}{\partial T} = \left[-i\phi - \frac{l}{2} - \frac{i\beta''}{2} \frac{\partial^2}{\partial t^2} + t_s \frac{\partial}{\partial t} + \frac{g(|u|)}{2} \left(1 + \frac{1}{2\omega_g^2} \frac{\partial^2}{\partial t^2} \right) + i\gamma|u|^2 + f_{\text{sa}}(|u|) \right] u, \quad (1.1)$$

where $u(t, T)$ is the complex field envelope, t is the retarded time, T is the slow time, ϕ is the phase rotation per unit time T , l is the linear loss coefficient, $g(|u|)$ is the saturated gain, t_s is the shift in t of the pulse centroid

$$t_c = \frac{\int t' |u(t')|^2 dt'}{\int |u(t')|^2 dt'}, \quad (1.2)$$

β'' is the group delay dispersion, γ is the Kerr coefficient, ω_g is the gain bandwidth, and $f_{\text{sa}}(|u|)$ is the fast saturable absorption. In the HME, it is assumed that the gain response of the medium is much longer than the round-trip time T_R , in which case the saturable gain becomes

$$g(|u|) = g_0 / [1 + P_{\text{av}}(|u|) / P_{\text{sat}}], \quad (1.3)$$

where g_0 is the unsaturated gain, $P_{\text{av}}(|u|)$ is the average power, and P_{sat} is the saturation power. We may write $P_{\text{av}}(|u|) = \int_{-T_R/2}^{T_R/2} |u(t, T)|^2 dt / T_R$. In the HME, we have

$$f_{\text{sa}}(|u|) = \delta|u|^2, \quad (1.4)$$

where δ is the fast saturable absorption constant.

It is useful to normalize Eq. (1.1) [15, 16]. The complex field envelope $u(t)$ is normalized with respect to its peak U_0 , the propagation variable T is normalized with respect to the round-trip time T_R , and the retarded time t is normalized with respect to a characteristic pulse time t_0 . Letting $u_n = u/U_0$, $T_n = T/T_R$, and $t_n = t/t_0$, Eq. (1.1) becomes

$$\begin{aligned} \frac{\partial u_n}{\partial T_n} = & \left[-i\phi T_R - \frac{lT_R}{2} + t_s T_R \frac{\partial}{\partial t_n} + \frac{g(|u|)T_R}{2} \left(1 + \frac{1}{2\omega_g^2 T_R^2} \frac{\partial}{\partial t_n^2} \right) \right. \\ & \left. - \frac{i\beta'' T_R}{2t_0^2} \frac{\partial}{\partial t_n^2} + i\gamma T_R U_0^2 |u_n|^2 + \delta T_R U_0^2 |u_n|^2 \right] u_n. \end{aligned} \quad (1.5)$$

Defining normalized parameters, $\phi_n = \phi T_R$, $l_n = lT_R$, $g_n(|u|) = g(|u|)T_R$, $\omega_{gn} = \omega_g T_R$, $\beta''_n = \beta'' T_R / t_0^2$, $\gamma_n = \gamma T_R U_0^2$, and $\delta_n = \delta T_R U_0^2$, we obtain a normalized version of Eq. (1.1). From hereon, we will use these normalized parameters, and we drop the subscript “ n .”

1.2 Saturable Absorption

Saturable absorption, which preferably attenuates the lower amplitude part of a pulse, plays an important role in passively modelocked lasers. By compressing the pulse in the time domain, a saturable absorber balances spectral narrowing in the frequency domain. Saturable absorbers are classified by their response time T_A relative to the pulse duration τ_p . Fast saturable absorbers are those for which $T_A < \tau_p$, while slow saturable absorbers are those for which $T_A > \tau_p$ [17–19].

We illustrate the two types of saturable absorption in Fig. 1.2. For both the fast and the slow saturable absorption, we assume that the system gain obeys

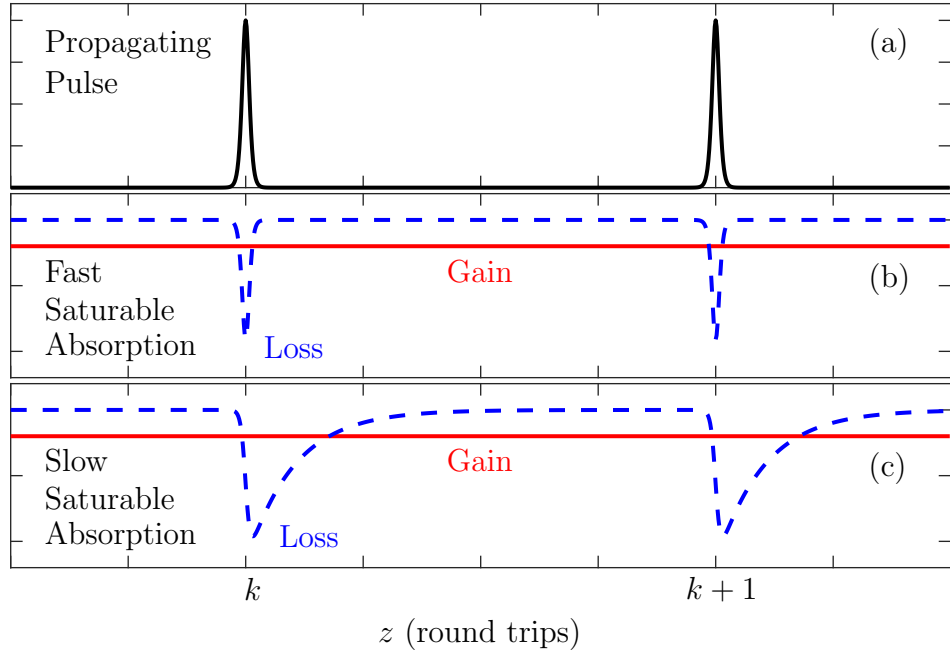


Figure 1.2: Illustration of gain and loss dynamics due to (a) a pulse train. The laser is assumed to include slow saturable gain and either (b) a fast saturable absorber or (c) a slow saturable absorber.

Eq. (1.3), which implies that the recovery time is longer than the round trip time so that the average gain appears to remain unchanged, as illustrated in Fig. 1.2. With a fast saturable absorber, the loss instantaneously saturates and recovers once the pulse is gone. So, the gain window in which the local gain is greater than the local loss has the same time duration as the pulse, as shown in Fig. 1.2(b). By comparison, as shown in Fig. 1.2(c), the loss of a slow saturable absorber has a long recovery time, which leads to a gain window after the pulse passes through, and the gain window is longer than the pulse duration. As a consequence, background noise

can grow in the wake of the pulse.

Examples of a passively modelocked laser with a fast saturable absorber include fiber lasers that use nonlinear polarization rotation [1,20] and solid-state lasers that use a Kerr lens [21,22]. The saturable absorption in the HME, which is given by Eq. (1.4), is fast. By comparison, examples of passively modelocked lasers with a slow saturable absorber include lasers that use semiconductor saturable absorber mirrors (SESAMs) [23], nanotubes [24], and graphene [25]. In this dissertation, we will analyze stability and noise in passively modelocked lasers with both fast and slow saturable absorbers.

1.3 Laser Models and Computational Approaches

Laser models	full/lumped distributed/averaged
Computational approaches	evolutionary dynamical/spectral

Table 1.1: A summary of the terminology for laser models and computational approaches.

The two computational approaches that we will use are the evolutionary approach and the dynamical approach. The models and approaches are summarized in Table 1. In the evolutionary approach, which replicates the physical behavior of

the laser, one launches light into the simulated laser and follows it for many round trips in the laser. If one obtains a stationary or periodically-stationary modelocked pulse, the laser is deemed stable and, if no such pulse is found, the laser is deemed unstable. The effect of noise can be studied by adding computational noise from a random number generator on each pass through the amplifier in a lumped model, in which all the laser devices are treated independently, or on each propagation step in an averaged model.

Modelocked pulses can be treated as equilibria (or fixed-points) of high-dimensional dynamical systems. We will take advantage of algorithmic advances that have been made within the past two decades in determining the stability and optimizing the performance of such systems, while carrying out further advances as needed to accurately model passively modelocked laser systems. The first step of the dynamical approach is to obtain a single steady-state solution either analytically or by using the evolutionary approach. Next, we find the pulse parameters as the laser parameters vary by solving a root-finding problem. We then linearize the evolution equations about the stationary solution and determine the eigenvalues of the linearized equation, which we refer to as the equation's dynamical spectrum. If any eigenvalue has a positive real part, then the modelocked pulse is unstable. The effect of noise can be determined by calculating the noise that enters each of the modes in the dynamical spectrum, whose amplitudes are described by either a Langevin process or a random walk process.

The evolutionary approach is intuitive and straightforward to program, and it is widely used. However, it is computationally time-consuming to determine the

stable operating regions and can give ambiguous results near a stability boundary [10]. When evaluating the laser’s output noise, Monte Carlo simulations, which are based upon the evolutionary approach, are often prohibitively expensive computationally. By comparison, the dynamical approach is more difficult to program, but it is computationally rapid, yields unambiguous results for the stability, and avoids computationally expensive Monte Carlo simulations. The two approaches are complementary to each other. However, the dynamical approach can be a powerful tool for system design and optimization and has historically been under-utilized.

1.4 Outline of the Dissertation

In Chapter 2, we present the stability analysis for a passively modelocked laser with fast saturable absorption. This analysis is built on dynamical systems theory—in particular linear stability analysis. This analysis is the basis of the boundary tracking algorithms, which we use to map the regions of stable operation in a wide range of parameter space, as well as the calculation of the dynamical spectrum and the corresponding modes, which we use to analyze the noise impact on statistical quantities of interest like the timing jitter and the power spectral density of the energy and phase. In Chapter 3, we model a SESAM fiber comb laser that was developed by our collaborators at NIST. The SESAM fiber laser is locked using a SESAM, which is a slow saturable absorber. Using a lumped model, we simulate the laser output pulse and the radio-frequency (RF) spectrum in which the wake mode sidebands appear. The wake modes sidebands corresponds to amplitude

modulations to the output pulse train, which is due to that the absorption recovery of the SESAM is slow comparing the pulse duration. In Chapter 4, we discuss the wake mode instability in the SESAM fiber comb laser. Using the boundary tracking algorithms to the SESAM laser model, we find its region of stable operation in the system parameter space. In Chapter 5, we describe the algorithmic details of analyzing the noise impact for both the dynamical and Monte Carlo approaches. In Chapter 6, we present an optimization study in which we present a design of the SESAM fiber comb laser in which the output power of the laser is increased by a factor of five, while the pulse duration is decreased by 10%, and the wake mode sidebands are well suppressed compared to the current experiments.

CHAPTER 2

Stability of Passively Modelocked Lasers with Fast Saturable Absorbers

Despite the vast quantity of both experimental and theoretical work that has been published on passively modelocked laser systems [5,6,26], little theoretical work has been done to investigate the stability of these systems over a broad parameter range. Typical theoretical studies solve the evolution equation, starting from noise or some other initial conditions and allow the solution to evolve until it either settles down to a stationary or periodically-stationary state or fails to settle down after a long evolution time [7]. This approach is ambiguous, since it is often not clear how long it is necessary to wait for a pulse to settle down, and the computation times approach infinity in principle when the system parameters approach a stability boundary.

In this section, we describe the boundary tracking algorithms, which we have developed [10] based on dynamical systems theory [27] to address this issue. A modelocked pulse can be viewed as a stationary solution or an equilibrium of a

nonlinear dynamical system. If any possible perturbation grows exponentially, then the system is unstable. The stability can be determined by solving a linear eigenvalue problem. Once a single modelocked solution has been found for a single set of parameters either analytically or using the evolution equations, we can rapidly trace the solution as parameters vary by solving a root-finding problem and determine the solution's stability without solving the evolution equations. Once a stability boundary is encountered, we can then track its location in the parameter space. This approach allows us to rapidly determine the existence and stability of pulses over a broad parameter range.

This dynamical approach has been used with great success in other areas of physics and engineering—including in particular fluids and plasmas [28, 29]—but it has not been systematically applied to modelocked laser systems. To our knowledge, it has only been applied to modelocked laser pulses in special cases with known analytical solutions [15].

In this chapter, we discuss the stability analysis of passively modelocked laser models with fast saturable absorption using the boundary tracking algorithms. Hence, we will focus on the HME and the cubic-quintic modelocking equation (CQME) [10].

2.1 The Cubic-Quintic Modelocking Equation

The HME only predicts a narrow stability range in the pulse parameters that is inconsistent with what has been observed experimentally [15, 30]. Motivated by

this observation—and in an effort to more accurately model the laser physics—other models of the fast saturable absorption have been introduced. A model whose stability range is more consistent with experiments is the cubic-quintic modelocking equation (CQME) [16], which is an extension to the HME, described in Eqs (1.1)–(1.4). In this equation, the fast saturable absorption is modeled as

$$f_{\text{sa,cq}}(|u|) = \delta|u|^2 - \sigma|u|^4, \quad (2.1)$$

with $\sigma > 0$. As a consequence, the gain saturates as $|u|^2$ increases.

There are two physics-based models of fast saturable absorption from which the cubic-quintic model in Eq. (2.1) is derived [31]. The first and oldest of these models is due to Haus [26, 32]. In this model, it is assumed that the absorbing medium is a two-level system in which the response time of the medium is fast compared to the pulse duration, so that the population of the upper state is proportional to $|u(t)|^2$. In this case, we find that [26, 32]

$$\left. \frac{\partial u}{\partial T} \right|_{\text{ab}} = f_{\text{ab}}(|u|)u = -\frac{f_0 u}{1 + |u(t)|^2/P_{\text{ab}}}, \quad (2.2)$$

where $\partial u/\partial T|_{\text{ab}}$ is the contribution to the loss from the absorbing mechanism, f_0 is a constant, and P_{ab} is the saturation power of the absorber. If $|u(t)|^2 \ll P_{\text{ab}}$, then we find

$$f_{\text{ab}}(|u|) = -f_0 + \frac{f_0}{P_{\text{ab}}}|u(t)|^2 - \frac{f_0}{P_{\text{ab}}^2}|u(t)|^4 - \dots \quad (2.3)$$

If we truncate this expansion at the order $|u|^4$, we find that $l/2$ in Eq. (1.1) equals $\alpha + f_0$, where α denotes the total loss that is not due to the material absorber,

such as losses from the end mirrors and couplers. We also find $\delta = f_0/P_{\text{ab}}$ and $\sigma = f_0/P_{\text{ab}}^2$.

The second physics-based model, due to Chen et al. [33], assumes that saturable absorption is due to a combination of nonlinear polarization rotation and polarization selective elements that attenuate low intensities more than high intensities. In this model, we find that [33–36]

$$\left. \frac{\partial u}{\partial T} \right|_{\text{ab}} = f_{\text{ab}}(|u|)u = -f_0u + f_1 \cos(\mu|u|^2 - \nu)u, \quad (2.4)$$

where the constants f_0 , f_1 , μ , and ν depend on the settings of the polarization selective elements and the amount of nonlinear polarization rotation in one pass through the laser. If we may assume $\mu|u|^2 \ll 1$, then

$$f_{\text{ab}}(|u|) = -f_0 + f_1 \cos \nu + \mu f_1 (\sin \nu) |u|^2 - (\mu^2 f_1 / 2) (\cos \nu) |u|^4 - \dots \quad (2.5)$$

The combination $-f_0 + f_1 \cos \nu$ may be absorbed into the total linear loss, and we find $\delta = \mu f_1 \sin \nu$ and $\sigma = (\mu^2 f_1 / 2) \cos \nu$.

We first develop the boundary tracking algorithms to computationally study the stability of pulse solutions of the CQME [10]. Our study focuses on the anomalous dispersion regime, i.e., $\beta'' < 0$, and we allow the strength of both the cubic coefficient δ and the quintic coefficient σ to vary relative to the chromatic dispersion.

2.1.1 Finding a Pulse Solution

The boundary tracking algorithms begin by finding a modelocked pulse solution (a stationary or equilibrium solution) at a single point in the (σ, δ) plane

by starting from an initial condition that we expect is close to a modelocked pulse solution. We do that by solving the evolution equation using the split-step Fourier method that we have described in [37]. We then find solutions at nearby points in (σ, δ) by solving a root-finding problem, which is roughly three orders of magnitude faster than solving the evolution equations. We can then rapidly track the solution as (σ, δ) varies over a broad parameter range. With the equilibrium solution, we have $\partial u / \partial T = 0$ in Eq. (1.1), and we find that Eq. (1.1) becomes

$$\left[-i\phi_0 - \frac{l}{2} + \frac{g(|u_0|)}{2} \left(1 + \frac{1}{2\omega_g^2} \frac{d^2}{dt^2} \right) - \frac{i\beta''}{2} \frac{d^2}{dt^2} + (i\gamma + \delta)|u_0|^2 - \sigma|u_0|^4 \right] u_0 = 0, \quad (2.6)$$

where $[u_0(t), \phi_0]$ denotes the equilibrium solution, and $g(|u_0|)$ is given by Eq. (1.3). Note that in the CQME, the function of saturable absorption $f_{\text{sa}}(|u|)$ is an even function in t , and thus we know *a priori* that $t_{s0} = 0$, where t_{s0} is the value of t_s in Eq. (1.1) for the equilibrium solution.

2.1.2 Linear Stability Analysis

To determine the linear stability of the system, once $[u_0(t), \phi_0]$ has been found for a given set of parameters, we linearize Eq. (1.1). We write $u(t, T) = u_0(t) + \Delta u(t, T)$, $\bar{u}(t, T) = u_0^*(t) + \Delta \bar{u}(t, T)$, and we obtain

$$\begin{aligned} \frac{\partial \Delta u}{\partial T} = & \left[-i\phi_0 - \frac{l}{2} + \frac{g(|u_0|)}{2} \left(1 + \frac{1}{2\omega_g^2} \frac{\partial^2}{\partial t^2} \right) - \frac{i\beta''}{2} \frac{\partial^2}{\partial t^2} + 2(i\gamma + \delta)|u_0|^2 \right. \\ & \left. - 3\sigma|u_0|^4 \right] \Delta u - \frac{g^2(|u_0|)}{2g_0 T_R P_{\text{sat}}} \llbracket u_0, \Delta u \rrbracket \left(1 + \frac{1}{2\omega_g^2} \frac{\partial^2}{\partial t^2} \right) u_0 \\ & + [(i\gamma + \delta)u_0^2 - 2\sigma|u_0|^2 u_0^2] \Delta \bar{u}, \end{aligned} \quad (2.7)$$

where $[[u_0, \Delta u]] = \int_{-T_R/2}^{T_R/2} (u_0^* \Delta u + u_0 \Delta u^*) dt$. We obtain a similar expression for $\partial \Delta \bar{u} / \partial T$. We now write $\Delta \mathbf{u}(t, T) = \exp(\lambda T) \Delta \mathbf{u}(t)$, where λ is a constant and $\Delta \mathbf{u} = [\Delta u, \Delta \bar{u}]^T$, where T denotes the transpose. Substituting this expression into the equation for $\partial \Delta u / \partial T$ and $\partial \Delta \bar{u} / \partial T$, we obtain an eigenvalue equation

$$\frac{\partial}{\partial T} \Delta \mathbf{u} = \mathbf{L}_0 \Delta \mathbf{u} = \lambda \Delta \mathbf{u}, \quad (2.8)$$

where the linear operator \mathbf{L}_0 is formulated using the corresponding operations on Δu and $\Delta \bar{u}$,

$$\mathbf{L}_0 = \begin{bmatrix} \mathbf{L}_{11} & \mathbf{L}_{12} \\ \mathbf{L}_{21} & \mathbf{L}_{22} \end{bmatrix}, \quad (2.9)$$

where $\mathbf{L}_{11} = \delta F / \delta u$, $\mathbf{L}_{12} = \delta F / \delta u^*$, $\mathbf{L}_{21} = \delta F^* / \delta u$, and $\mathbf{L}_{22} = \delta F^* / \delta u^*$ are functional derivatives. A detailed discussion of our computational implementation for solving this eigenvalue problem is given in [10].

The quantity λ is an eigenvalue and $\Delta \mathbf{u} = \mathbf{e}_\lambda = [\mathbf{e}_\lambda, \bar{\mathbf{e}}_\lambda]^T$ is the eigenmode corresponding to λ . We are also assuming that \mathbf{L}_0 can be decomposed into a complete set of eigenmodes, *i.e.*, it is not defective. That is not necessarily the case; for example, the operator for the linearized nonlinear Schrödinger equation is defective [38]. However, this situation never occurs in the laser models that we have studied. In these laser models, the linear stability of the equilibrium solution is determined by the dynamical spectrum of all the eigenvalues on the complex plane. If $\Delta u(t, T = 0) = \Delta u^*(t, T = 0)$, so that $\Delta \bar{u}$ and Δu are initially complex conjugates, then they remain complex conjugates at all z . However, it is not generally the case that $\bar{\mathbf{e}}_\lambda = \mathbf{e}_\lambda^*$.

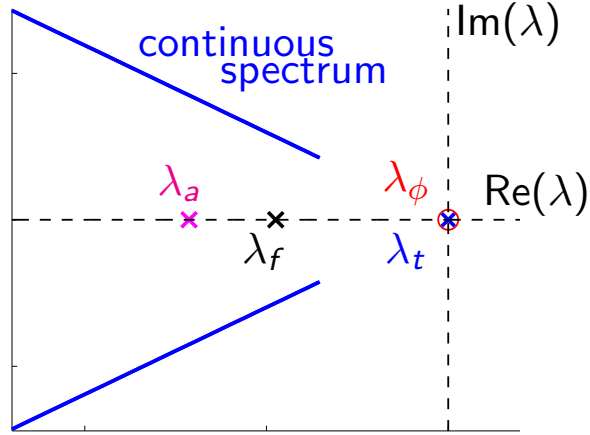


Figure 2.1: Illustration of the dynamical spectrum when the pulse solution of the modelocking equation is linearly stable.

Figure 2.1 shows an illustration of the distribution of the eigenvalues that is evaluated for a given stable pulse solution. The eigenvalues include the two branches of the continuous spectrum that are complex conjugates and four real discrete eigenvalues that correspond physically to the perturbations of the pulse solution's central time (λ_t), central phase (λ_ϕ), amplitude (λ_a), and central frequency (λ_f) [9, 38]. When the system is stable, the real part of all the eigenvalues are non-positive. The system becomes unstable if any eigenvalue becomes positive as the system parameters vary. It is also possible for a stationary solution to cease to exist due to a saddle-node bifurcation. The CQME is invariant when time and phase are shifted, so that $\lambda_t = 0$ and $\lambda_\phi = 0$ in all cases.

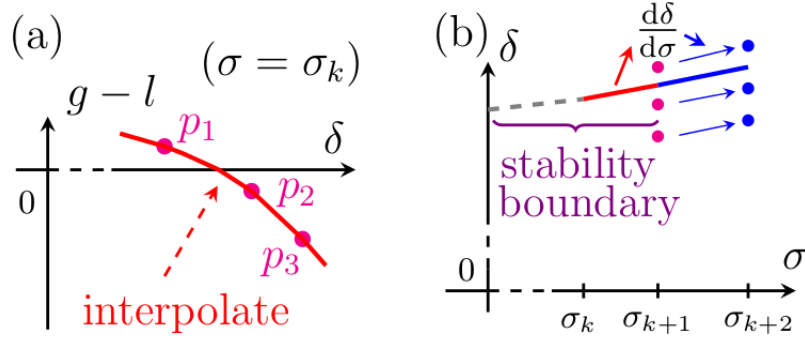


Figure 2.2: Illustration of tracking the stability boundary of the continuous eigenmodes using boundary tracking algorithms. In this case, the most unstable continuous eigenmodes we track correspond to an eigenvalue λ that satisfies $\text{Re}(\lambda) = g - l$.

2.1.3 Tracking Stability Boundaries

We vary (σ, δ) until we encounter a stability boundary, and we then track the boundary of stable operation. The boundary tracking algorithms track the stability boundaries by determining the variation of the target eigenvalue as the system parameters vary. In Fig. 2.2, we show schematically how to apply boundary tracking algorithms to track a stability boundary in the case that unstable stationary solutions exist on the opposite side of the boundary from the stable solutions. We implement the boundary tracking algorithm in this case by first varying the cubic coefficient δ , while the quintic coefficient σ remains fixed ($\sigma = \sigma_k$), and determining the variation of the λ_k . Eventually, we encounter a case $p_1 = (\sigma_1, \delta_1)$ in

which we cross the stability boundary, as shown schematically in Fig. 2.2(a), indicating that the corresponding equilibrium solution has become unstable via a Hopf bifurcation [10, 27]. We may then use two nearby stable points, here denoted by $p_2 = (\sigma_k, \delta_2)$ and $p_3 = (\sigma_k, \delta_3)$, to find the boundary using quadratic interpolation. At a nearby value of σ , σ_{k+1} , we once again find one unstable and two stable points and again interpolate to find the stability boundary. From these two points on the stability boundary, we obtain an estimate for the slope of the boundary $d\delta/d\sigma$, which allows us to predict where the three points surrounding the boundary will be when $\sigma = \sigma_{k+2}$. We quadratically interpolate to find the boundary at $\sigma = \sigma_{k+2}$, we correct these predictions, and we obtain a new prediction for the slope. In this way, we accurately and rapidly map out the entire boundary.

If the solution ceases to exist on the other side of the boundary, then we use three points on the same side of the boundary and extrapolate to the boundary location. Otherwise, the algorithm remains the same.

A detailed description of the boundary tracking algorithms can be found in [10].

2.1.4 Stable Regions of the CQME

Figure 2.3 shows the stability regions of the CQME. One pulse solution is stable in the blue-hatched region $[2_l]$, and another is stable in the red-hatched region $[2_h]$. Two solutions co-exist in a triangular-shaped region (marked by [3]) in the middle, in which the energy of the solution in the red-hatched region is always greater than

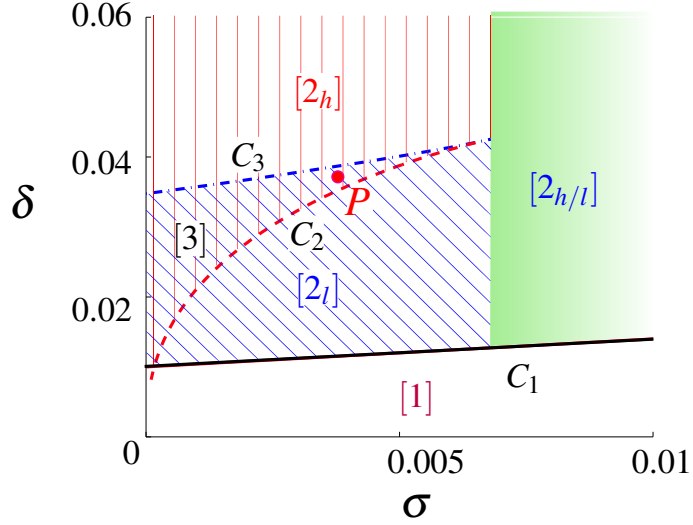


Figure 2.3: The stability regions of the pulse solutions of the CQME.

the solution in the blue-hatched region. We refer to the solution in the blue-hatched region as the low-amplitude solution (LAS) and the solution in the red-hatched region as the high-amplitude solution (HAS). The LAS and the HAS merge together in region $[2_{h/l}]$ that is colored green so that there is only one solution. In region $[1]$, which is unhatched, the radiation modes are unstable. In general, we have found that the stability regions are characterized by three curves C_1 , C_2 , and C_3 in the parameter range that we studied. Each curve indicates a different instability mechanism, which we summarize in Table 2.1. The δ -axis of Fig. 2.3 corresponds to the HME in which the quintic nonlinearity is zero ($\sigma = 0$). A known analytical solution is stable with $0.01 < \delta < 0.0348$ [15]. In [10], the equilibrium solution that we refer to as the low-amplitude solution (LAS) is a continuation of this HME solution when $\sigma > 0$, and it is stable in the blue-hatched region that is labeled $[2_l]$.

The LAS becomes unstable in region [1] (below the curve C_1), where the continuous modes become unstable via a Hopf bifurcation or the essential instability [39]. The amplitude eigenmode becomes unstable when we cross C_3 from region [2_l], which corresponds to a saddle-node bifurcation in which the equilibrium solution ceases to exist. By contrast, the HAS does not exist for the HME even though the blue-hatched region extends to $\sigma = 0$, so that the behavior of the CQME is qualitatively different from the HME. We note, however, that the HAS becomes increasingly singular as $\sigma \rightarrow 0$, which we show in detail in [40].

Curve	Equilibrium	Instability Mechanism
C_1	LAS	Essential
C_2	HAS	Saddle-node
C_3	LAS	Saddle-node

Table 2.1: Instability mechanisms of the CQME shown in Fig. 2.3, where LAS stands for the low-amplitude solution, and HAS stands for the high-amplitude solution.

Figure 2.4 shows an example of the pulse profiles of both the LAS and the HAS when $\sigma = 0.004$ and $\delta = 0.036$, which is at the point P in Fig. 2.3. The pulse envelopes of both the LAS and the HAS have a nearly hyperbolic secant profile, in which the amplitude decays exponentially as $t \rightarrow \pm\infty$. Compared to the LAS, the amplitude of the HAS is visibly higher, and the pulse duration is smaller.

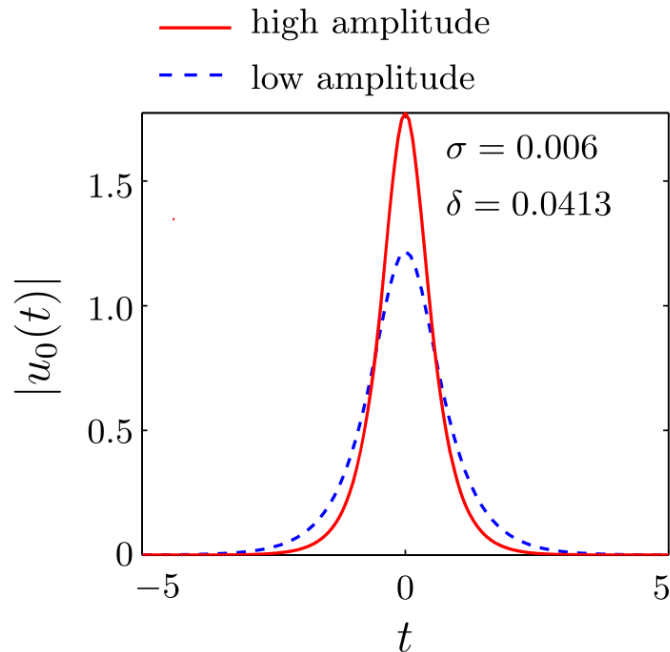


Figure 2.4: The pulse solution profiles of the low-amplitude solution (LAS) and the high-amplitude solution (HAS) of the CQME with $(\sigma, \delta) = (0.004, 0.8036)$.

In summary, we have developed a boundary tracking algorithm that allows us to rapidly and accurately find the stability boundaries in a passively modelocked laser system as the system parameters vary. We have applied this approach to determine the stability boundaries for the CQME as the parameters that govern the saturable absorption, σ and δ , are allowed to vary. This model is one of the most commonly used models for passively modelocked lasers and includes the even more commonly used Haus modelocking equation as a special limit corresponding to $\sigma = 0$.

We have found a rich dynamical structure in which, depending on the parame-

ter, no stable solutions exist, one stable solution exists, or two stable solutions exist. Additionally, we have found that in some extreme parameter ranges, new discrete modes appear in the dynamical spectrum, which then become unstable via a Hopf bifurcation, and which we will describe in Sec. 2.2.1.

The boundary tracking algorithm enables us to track the stability boundary of modelocked lasers with much better computational efficiency than is possible using the evolutionary approach. On a desktop computer, tracing the stability boundary for the amplitude eigenmode requires a few hours (about 1.5–2 hours in our case) in two parameter dimensions due to the rapid variation of the equilibrium solution at the boundary. By contrast, tracing the other stability boundaries typically requires only minutes on a desktop computer. However, our estimate of the time that would be required to find the boundaries using the evolutionary method is in the order of days.

2.2 On the High-amplitude Solution

A significant difference between the CQME and the HME is that (by adding a quintic nonlinearity) the stability region of the modelocked pulse is broadened significantly as shown in Fig. 2.3. This result is consistent with previous claims that the stability region for the HME is unrealistically small [16, 41]. The low-amplitude solution that appears is an extension of the previously reported HME solution, while the high-amplitude solution is a new solution that only exists when the quintic nonlinearity coefficient $\sigma \neq 0$. Here, we describe some unique features

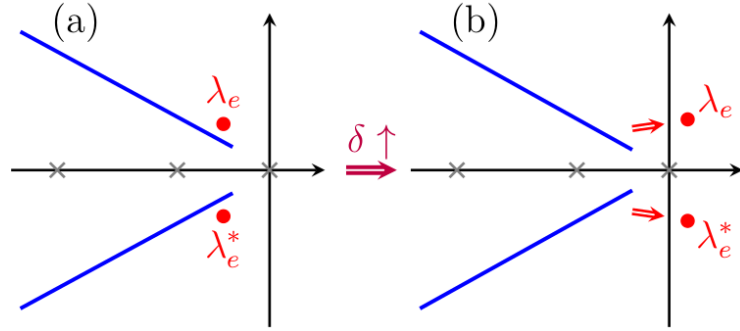


Figure 2.5: Illustration of the emergence and destabilization of the corresponding eigenmodes of new discrete eigenvalues as δ grows: from (a) an edge bifurcation to (b) a Hopf bifurcation.

of the high-amplitude solution.

2.2.1 Appearance of New Discrete Modes

The high-amplitude solution is stable over a range of δ that is hundreds of times larger than the range over which the LAS is stable. However, when $\delta \approx 9.51$, we find that a pair of new discrete eigenvalues, λ_e and λ_e^* , emerge via an edge bifurcation from the continuous spectrum. Here, we will use λ_e to denote the new discrete eigenvalue whose imaginary part is positive and λ_e^* to denote its complex conjugate. With a small additional increase in δ , $\Delta\delta \approx 0.001$, the eigenmodes become unstable via a Hopf bifurcation. We show this process schematically in Fig. 2.5. As δ increases, further edge bifurcations occur, so that more discrete eigenmodes appear and then go unstable via Hopf bifurcations.

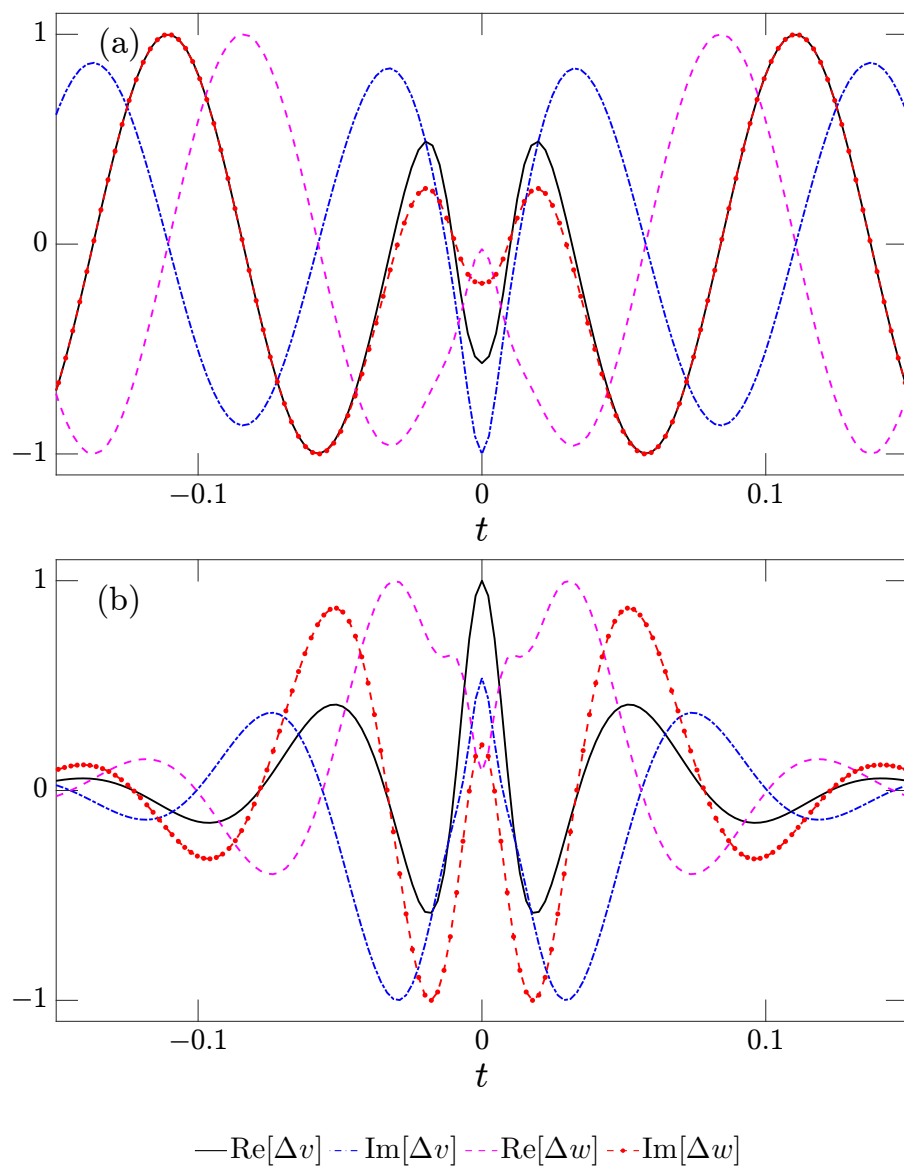


Figure 2.6: The eigenmodes corresponding to λ_e with $\sigma = 0.003$ and

(a) $\delta = 9.509$, $\lambda_e = -0.40 + 1.05 \times 10^4 i$; (b) $\delta = 13$,

$\lambda_e^* = (0.31 + 1.33i) \times 10^4$.

As δ continues to increase, so do the real parts of λ_e and λ_e^* , and these corresponding eigenmodes become increasingly narrow. In Fig. 2.6 we show a comparison

of the corresponding eigenmodes for λ_e respectively when $(\sigma, \delta) = (0.003, 9.509)$ and $(\sigma, \delta) = (0.003, 13)$. We note parenthetically that it is more computationally efficient to use $\Delta v = (\Delta u + \Delta \bar{u})/2$ and $\Delta w = (\Delta u - \Delta \bar{u})/2i$ in place of Δu and $\Delta \bar{u}$ since both Δv and Δw are real when $\Delta u^* = \Delta \bar{u}$ [10]. We note that both Δv and Δw are even and complex in contrast to the original four discrete eigenmodes for which the eigenmodes corresponding to λ_t and λ_ω are odd and real, while those corresponding to λ_ϕ and λ_a are even and real. When $\delta = 9.509$, which is shortly after the edge bifurcation has occurred, the decay as $|t|$ increases is barely visible. By contrast, the decay as $|t|$ increases is clearly visible when $\delta = 13$.

Accurately finding the eigenmodes and eigenvalues that appear right after the edge bifurcation is a difficult computational problem. Very large computational windows are needed to obtain accurate results—too large to be feasible. If the linear eigenvalue problem could be formulated as a differential equation, then we could use shooting methods. However, that is also not possible in this case because of the gain dependence on the pulse energy, so that the linear equation is an integro-differential equation that is non-local in t . We avoid these difficulties by formulating the eigenvalue problem as an overdetermined set of linear equations $\mathcal{H}[\lambda_e, \Delta u(t); \sigma, \delta] = 0$, where we demand that the solution is exponentially decaying as $t \rightarrow \pm\infty$. Given a pair (σ, δ) and a choice of λ_e that matches these boundary conditions, the equation $\mathcal{H} = 0$ will not, in general, have a solution. However, if we have a good initial guess for $[\lambda_e, \Delta u(t)]$, we can find this pair iteratively using a root-finding procedure. The details of this computational approach are described in [10].

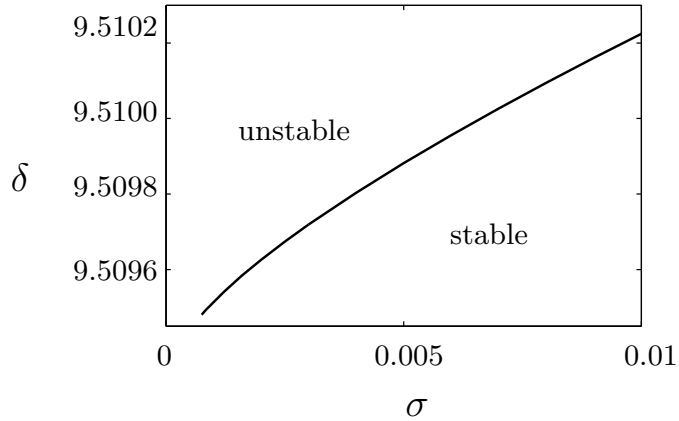


Figure 2.7: Stability boundary of the high-amplitude solution due to the edge bifurcation as illustrated in Fig. 2.5.

2.2.2 Stability Boundary of the Hopf Bifurcation

We find that the high-amplitude solution remains stable for a very large range of both σ and δ . The lower bound of the stability region is shown by the curve C_2 as in Fig. 2.3, and is bounded on the left by the δ -axis. We have discussed this boundary in [40]. The upper bound of the stability region of the high-amplitude solution is the onset of edge bifurcation, followed shortly thereafter as δ increases by a Hopf bifurcation of the new discrete modes. We show this stability boundary in Fig. 2.7, and we see that the boundary for δ increases slightly as σ increases. We do not show the stability boundary for $\sigma < 7 \times 10^{-4}$ because the equilibrium pulse shape change rapidly as δ and σ vary, and tracking the boundary becomes computationally time-consuming. Indeed, the parameter set at this relatively large value of δ is sufficiently extreme that it seems unlikely that it corresponds to any

physical laser system. However, our results show that modelocked pulses with high energy can be obtained if the quintic coefficient σ is decreased. Additionally, these results show the power of the algorithms that we have developed.

2.3 Agreement with Experiments

In Sec. 2.1.4, we showed that two stable stationary pulse solutions of the CQME coexist with an arbitrarily small value of σ , as long as $\sigma > 0$, in contrast to the HME, where there is only one stable solution in a very limited range of the cubic nonlinearity δ . Since any real system is likely to have a quintic component in its saturable absorber [42], the solutions of the CQME with higher nonlinearities should provide a better approximation to output pulses that have been observed in experiments than does the HME. In this section, we will perform this comparison.

We show in Table 2.2 the parameters that we use in the comparative study. Set 1 of the parameters corresponds to a fiber laser with nonlinear polarization rotation [1, 2], and set 2 of the parameters corresponds to a Cr:LiSAF laser that uses Kerr-lens modelocking [3].

We show a comparison of the computational stationary pulses and the corresponding experimental results in Fig. 2.8. The fiber laser in [1] generates a comb output with chirped pulses that have a duration of 210 fs and a peak power of 435 W. Using the CQME, we are able to obtain a computational pulse duration an FWHM duration of 271 fs and peak power of 421 W. By comparison, using the HME, we achieve the closest match to the experimental pulse by setting $\delta = 0.705 \text{ kW}^{-1}$,

Parameter		g_0	l	γ	ω_g	β''	$T_R P_{\text{sat}}$	δ	σ
set 1	value	2.00	1.65	4.10	8.66	-0.04	0.30	0.87	0.55
	unit	1	1	kW ⁻¹	rad/ps	ps ²	nJ	kW ⁻¹	kW ⁻²
set 2	value	0.241	0.045	0.65	1257	-8.0	3.4	0.043	0.114
	unit	1	1	MW ⁻¹	rad/ps	10 ⁻⁵ ps ²	nJ	MW ⁻¹	MW ⁻²

Table 2.2: Values of the parameters that we use to validate the computational results.

where the stationary pulse has a FWHM duration of 32.8 fs and a peak power of 287 W. When δ further increases, a saddle-node bifurcation occurs, and the HME solution ceases to exist. The match of the CQME solution to the experimental pulse is visibly better than the HME solution. The accuracy of the CQME model can be further improved by a more accurate measurement of the parameters. In particular, the value of dispersion given in [1] neglects the contribution from some cavity components.

In Fig. 2.8(b), we show a comparison of the computational pulse with the experimental pulse corresponding to the solid state laser of [3]. In the experiment, a gain-matched output coupler is used to overcome the gain filtering effect. Using the transmission profile of the output coupler given in [3], we are able to obtain accurately the pulse profile inside the laser cavity, where the pulse energy is 14.8 nJ and the FWHM width is 30 fs. We estimate that the saturation power of the saturable absorption P_{ab} is 363 kW, and the saturable loss f_0 is 3%. The system

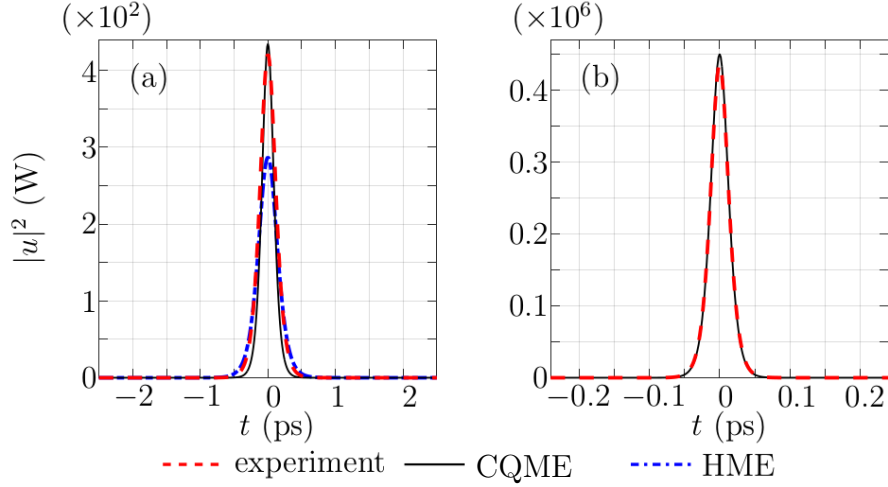


Figure 2.8: Comparison of the computational stationary pulses with the experimental pulses using parameters in (a) set 1 [1,2] and (b) set 2 [3].

parameters are estimated following the approach in [43]. An algebraic model was used to model the fast saturable absorption. By matching the cubic and the quintic coefficients, as seen from Fig. 2.8(b), we are able to obtain a computational pulse of 14.9 nJ with an FWHM width 29.2 fs, for which the match is excellent. By comparison, no stable solution exists for the HME when we set $\sigma = 0$.

Compared to the HME, where at most only one stable solution exists for any set of system parameters, the CQME can have two stable stationary pulse solutions that both exist for the same set of system parameters with an arbitrarily small value of σ , as long as $\sigma > 0$. When $\sigma \rightarrow 0$, the low amplitude solution tends to the stable solution of the HME, where an analytical expression is available, as long as δ is below the HME's stability limit. By comparing our calculations with experimental

results, we show that the CQME can provide a better approximation to the pulse shape than does the widely-used HME model. This result is not surprising since a quintic nonlinearity appears in any real fast saturable absorber. Combined with the existence of a large stability region for the CQME, which is consistent with the existence of a large region of stability that has been reported in modelocked lasers [44], we conclude that models of the fast saturable absorption that include high-order nonlinearities should be preferred to the HME.

2.4 Comparison of Different Models of Fast Saturable Absorption

As previously noted, there has been considerable controversy concerning which model is “best” to use in the sense that it best reproduces the large stability region that is observed in experiments [30, 44]. We mentioned in Sec. 2.1 that the CQME is derived from two physics-based models of saturable absorption: the algebraic model in Eq. (2.2) and the sinusoidal model in Eq. (2.4). We have compared the stability regions that are predicted by these models of fast saturable absorption,

$$\begin{aligned}
 f_{\text{sa,cq}}(|u|) &= \delta|u|^2 - \sigma|u|^4, \\
 f_{\text{sa,al}}(|u|) &= \frac{\delta|u|^2}{1 + (\sigma/\delta)|u|^2}, \\
 f_{\text{sa,sn}}(|u|) &= \frac{\delta^2}{2\sigma} \left[\sqrt{2} \sin \left(\frac{2\sigma}{\delta}|u|^2 + \frac{\pi}{4} \right) - 1 \right].
 \end{aligned}
 \tag{2.10}$$

A comprehensive stability study is described in [31] that applies the boundary tracking algorithms that we described in Sec. 2.1.3 to Eq. (1.1) with these three different models of saturable absorption, i.e., $f_{\text{sa}}(u)$ in Eq. (2.10). For each of the three models, we found that the stability region is greatly increased relative to the

HME. The behaviors of these models are qualitatively similar but quantitatively different, and the difference becomes more significant as the input power increases. The applicability of the boundary tracking algorithm to different laser models indicates that it can be extended to experimental systems whose physical components can be characterized with sufficient accuracy. The details of this comparison can be found in [31].

2.5 Summary

In this chapter, we have shown that the CQME provides a more general description of passively modelocked lasers with fast saturable absorption than does the HME. More importantly, we have shown that the boundary tracking algorithms can find the regions of stable operation in a wide range of the parameter space both rapidly and unambiguously. Next, we will perform a stability analysis of a comb laser with a slow saturable absorber.

CHAPTER 3

Modelocking with Slow Saturable Absorption

We introduced two different types of saturable absorption models depending on the ratios of saturable absorber response time T_A to the modelocked pulse duration τ_p . In Chapter 2, we discussed the stability of a passively modelocked laser with a fast saturable absorber. In this chapter, we will focus on a passively modelocked laser with a slow saturable absorber. In particular, we will focus on a modelocked fiber comb laser that uses a semiconductor saturable absorption mirror (SESAM). This laser was built in the Fiber Sources and Applications Group at National Institute of Standard and Technology (NIST), Boulder, CO, USA [23], led by Dr. N. Newbury. The structure of this laser is illustrated in Fig. 3.1.

The SESAM laser that we will study is built with telecom-grade polarization-maintaining (PM) components, and it is able to generate highly stable 300-MHz combs [23]. The cavity components include a 22.4-cm-long segment of highly-doped erbium-doped fiber, a segment of highly non-linear PM fiber that is 12.2 cm in length,

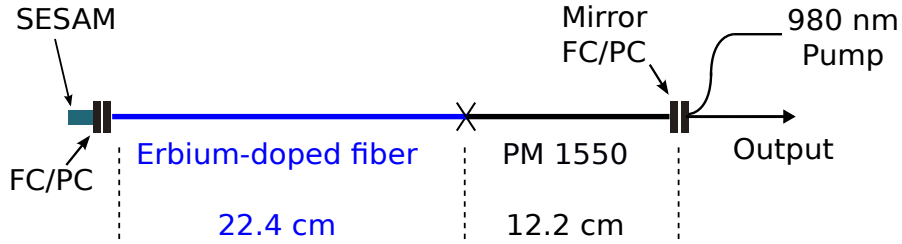


Figure 3.1: Illustration of the SESAM fiber laser.

and a semiconductor saturable absorber mirror (SESAM) with a response time of 2 ps. The pump signal is a 980-nm CW solid-state laser, and the pump is launched into the cavity via a wavelength-division-multiplexing (WDM) coupler. The output pulse duration is about 250 fs, the round trip time is 5 ps, and the gain recovery time is 1–10 ms.

The SESAM is a slow saturable absorber with a response time $T_A = 2$ ps, which is longer than the modelocked pulse duration $\tau_p \approx 311$ fs [45]. We illustrated the two types of saturable absorption in Fig. 1.2, and we described a mechanism by which this laser can become unstable that is not present in lasers with fast saturable absorbers. Background noise can grow in the wake of the pulse due to a long recovery time, which leads to a gain window that follows the pulse and is longer than the pulse duration. We refer to this instability as the wake mode instability [46, 47].

In this chapter, we first model the SESAM fiber laser using a lumped model, from which we extract the set of parameters that we will use in our later modeling, using averaged models. In addition, we will provide an initial stability analysis, and we will then introduce the wake mode instability. We will further show the Fourier

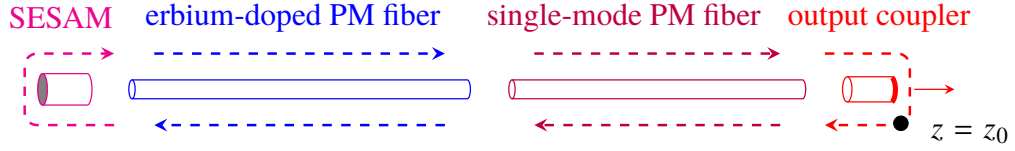


Figure 3.2: Propagation of the modelocked pulse inside the laser cavity. The black dot indicates the location at which we compare the pulse profile to determine stability.

spectrum of the wake mode sidebands. Additionally, we describe a model of the spectrum analyzer, which allows us to calculate the output radio frequency (RF) spectrum of the comb laser, and hence to demonstrate the agreement between our computational model and the experimental observations.

3.1 Modeling the Laser Cavity

In the SESAM fiber comb laser that we show in Fig. 3.1, the light is almost entirely in a single transverse mode because polarization-maintaining fibers are used to construct the laser cavity. Here, we simulate our comb laser using a lumped model, in which the operation of each component on the incoming pulse is considered independently, and the operations are cascaded consecutively [11]. We first characterize each component in the laser cavity, and we present the complete model at the end of this section.

We show a schematic illustration of the laser cavity in Fig. 3.2. We start from a pulse that is close in amplitude and pulse duration to the experimentally-measured

pulse, and we let the pulse be acted on successively by each component. After the output coupler, we compare the pulse amplitude with that of the last round trip

$$\epsilon_n = \frac{\int_{T_R/2}^{-T_R/2} (|u_n(t, z_0)| - |u_{n-1}(t, z_0)|)^2 dt}{\int_{T_R/2}^{-T_R/2} |u_n(t, z_0)|^2 dt}, \quad (3.1)$$

where u_n represents the complex light field at the end of the n th round trip, and z_0 is the location inside the laser cavity where the comparison is made, as shown in Fig. 3.2 as a black dot. We consider the system to be stable if the difference ϵ_n becomes less than 10^{-3} after 4000 round trips in the cavity. We use a hyperbolic-secant pulse as our initial condition,

$$u_0(t) = \sqrt{U_0/\tau_0} \operatorname{sech}(t/\tau_0), \quad (3.2)$$

where the pulse energy $U_0 = 183$ pJ, the full-width-at-half-maximum (FWHM) pulse duration $\tau_0 = 260$ fs, and the pump power is 234 mW. The values of the physical parameters that we use are listed in Table 3.1.

3.1.1 Output Coupling

The reflectance of the output coupler that we used is 91%, while the loss of the output coupler is 12%. Hence, we find that the output coupling ratio is 9%, and there is a 3% loss of cavity energy at the output coupler. Here, we assume that the loss of 3% is evenly distributed between the incident and the reflected waves, as shown in Fig. 3.3. The output power that we use is 4.9 mW.

Parameter		Value	
Roundtrip time		T_R	3.33 ns
Output coupling loss		l_{oc}	12%
Stationary Pulse	FWHM Pulse Duration	τ_0	250 fs
	Pulse Energy	U_0	186 pJ
Single Mode Fiber	Length	L_{SMF}	0.122 m
	Background loss	l_0	$1.15 \times 10^{-4} \text{ m}^{-1}$
	Second-order dispersion	β_2	0.300 ps ² /m
	Kerr nonlinearity coefficient	γ	$1.8 \times 10^{-3} \text{ W}^{-1}\text{m}^{-1}$
Coupling loss at the fiber splice			-0.2 dB
Er-doped Fiber	Length of the erbium fiber	L_{EDF}	0.224 m
	Pump wavelength	λ_p	0.98 nm
	Background loss of the pump	l_p	$2.30 \times 10^{-3} \text{ m}^{-1}$
	Background loss of the pulse	l_s	$5.30 \times 10^{-4} \text{ m}^{-1}$
	Gain spectrum	$g_{p,s}^*$	See [48]
	Absorption spectrum	$\alpha_{p,s}$	See [48]
	Second-order dispersion	β_2	0.300 ps ² /m
	Kerr coefficient	γ	$1.80 \times 10^{-3} \text{ W}^{-1}\text{m}^{-1}$
	Pump power (can vary)	P_p	234 mW
	Density of Er ³⁺	N	$3.47 \times 10^{25} \text{ cm}^{-3}$
	Index-core radius	a	3.50 μm
	Florescent lifetime	τ	14.7 ms
SESAM [49]	Nonsaturable Loss	l_{ns}	6%
	Saturable Loss	ρ	8%
	Response time	T_A	2 ps
	Saturation Energy	w_A	157 mW

Table 3.1: Physical parameters of the laser oscillator.

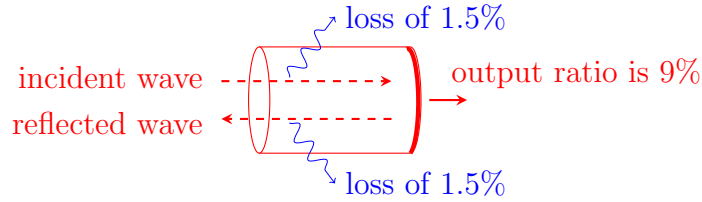


Figure 3.3: The allocation of the loss at the output coupler.

3.1.2 Single-mode fiber

The single mode polarization-maintaining fiber that is used in the experiment is a PANDA PM-1550 fiber. We use a partial differential equation that is based on the nonlinear Schrödinger equation (NLSE) to describe the propagation of the pulse inside the optical fiber,

$$\frac{\partial u(t, z)}{\partial z} = -\frac{l}{2}u - i\frac{\beta_2}{2}\frac{\partial^2 u}{\partial t^2} + i\gamma|u|^2u, \quad (3.3)$$

where u is the pulse envelope, t is the retarded time, z is the propagation distance, l is the linear loss, β_2 is the second-order dispersion of the SMF, and γ is the Kerr nonlinearity coefficient.

In our simulation, we keep a time window T_w surrounding the pulse, and we use the split-step Fourier method [37, 50] to solve Eq. (3.3). In order to eliminate the influence of dispersive waves during the evolution, we use absorbing boundary conditions, setting

$$l(t) = l_0 + A \exp \left[-\left(\frac{t + T_w/2}{\tau_0} \right)^2 \right] + A \exp \left[-\left(\frac{t - T_w/2}{\tau_0} \right)^2 \right], \quad (3.4)$$

where l_0 is the background loss of the single-mode fiber, and we choose values of A

and τ_0 that ensure that the boundary absorption does not affect the evolution of a stationary pulse.

3.1.3 Erbium-Doped Fiber

We describe the propagation of the pulse inside the EDF using a variant of the nonlinear Schrödinger equation

$$\frac{\partial u(t, z)}{\partial z} = -\frac{l}{2}u + \frac{\hat{g}(u, z)}{2}u - i\frac{\beta_2}{2}\frac{\partial^2 u}{\partial t^2} + i\gamma|u|^2u + s(t, z), \quad (3.5)$$

where u is the pulse envelope, t is the retarded time, z is the propagation distance, l is the linear loss, \hat{g} is the saturated gain operator, β_2 is the second-order group velocity dispersion, γ is the Kerr nonlinearity coefficient, and $s(t, z)$ is the amplified spontaneous emission (ASE) noise. The nonlinear gain operator \hat{g} represents a band-limited gain coefficient that is saturated by the forward- and backward-propagating optical signals. We calculate $\hat{g}(u, z)$ and the amplified spontaneous emission (ASE) noise using the Giles-Desurvire model [51]. The model can be written as

$$\begin{aligned} dP_p(z)/dz &= [(\alpha_p + g_p^*)n_2 - (\alpha_p + l_p)] P_p, \\ \pm dP_k^\pm(z)/dz &= [(\alpha_k + g_k^*)n_2 - (\alpha_k + l_k)] P_k^\pm, \\ \pm dP_{sk}^\pm(z)/dz &= [(\alpha_k + g_k^*)n_2 - (\alpha_k + l_k)] P_{sk}^\pm + 2g_k^*n_2h\nu\Delta\nu, \end{aligned} \quad (3.6)$$

where P_p , P_k , and P_{sk} are the pump power, the average pulse power, and the ASE noise power inside the k -th bandwidth, respectively, the indices “p” and “k” indicate the pump and the k -th frequency band, α , g^* , and l are the fiber absorption, gain, and background loss, respectively; n_2 is the propagation dependent normalized upper

state population,

$$n_2 = \frac{P_p \alpha_p / (h\nu_p \zeta) + \sum_k P_k^\pm \alpha_k / (h\nu_k \zeta) + \sum_k P_{sk}^\pm \alpha_k / (h\nu_k \zeta)}{1 + P_p^\pm (\alpha_p + g_p^*) / (h\nu_p \zeta) + \sum_k P_k^\pm (\alpha_k + g_k^*) / (h\nu_k \zeta) + \sum_k P_{sk}^\pm (\alpha_k + g_k^*) / (h\nu_k \zeta)}, \quad (3.7)$$

$\Delta\nu$ is the bandwidth of the frequency bands, $\zeta = \pi a^2 N / \tau$ is the fiber saturation parameter, in which a is the index-core radius; and τ is the metastable lifetime. The saturated gain is written in the frequency domain as

$$\tilde{g}_k(u, z) = (1/2) [(\alpha_k + g_k^*) n_2(u, z) - \alpha_k]. \quad (3.8)$$

We substitute Eq. (3.8) in Eq. (3.5) which we solve using a variant of the split-step method [37]. The ASE noise is added to the signal after the EDF [52]

$$\tilde{s}_k = P_{sk} \exp(i\phi_k), \quad (3.9)$$

where the phase ϕ_k is a random phase for each frequency band.

3.1.4 Semiconductor Saturable Absorption Mirror (SESAM)

We use a two-level model to characterize the dynamics of the upper state population. We assume that it induces loss at a single point in the fiber, so that

$$u_{\text{out}} = \exp \left\{ - \left[\frac{\rho}{2} n(t) + \frac{l_{\text{ns}}}{2} \right] \right\} u_{\text{in}}, \quad (3.10)$$

$$\frac{\partial n}{\partial t} = - \frac{n - 1}{T_A} + \frac{|u|^2}{w_A} n,$$

where ρ is the saturable loss, l_{ns} is the non-saturable loss, n is the normalized lower state population, T_A is the response time, and w_A is the saturation energy of the SESAM. The values of the SESAM parameters that we use in Eq. (3.10) are listed in Table. 3.1.

3.2 Output of the Comb Laser

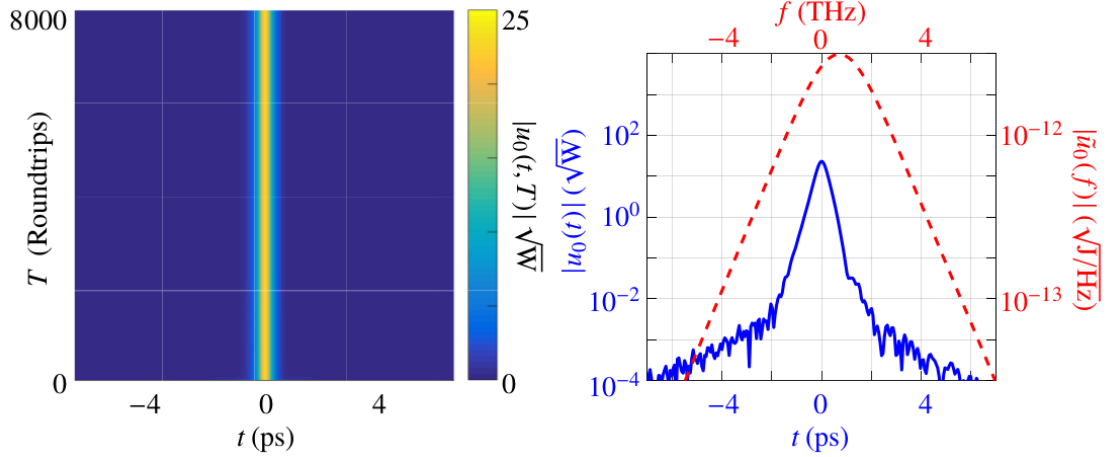


Figure 3.4: (a) The computational evolution of the stationary pulse, in which color indicates the pulse’s amplitude; (b) the stable pulse’s amplitude and phase in the time domain and the frequency domain, where $f = 0$ corresponds to $\lambda = 1570$ nm.

In Fig. 3.4, we show the stationary cavity pulse in both the time domain, $u_0(t)$, and the frequency domain, $\tilde{u}_0(f)$,

$$\tilde{u}_0(f) = \int_{-T_R/2}^{T_R/2} u_0(t) \exp(-2i\pi ft) dt. \quad (3.11)$$

The FWHM pulse duration is 311 fs, and the cavity pulse energy is 186 pJ. The profile of the stationary pulse is visibly asymmetric about $t = 0$; the pulse amplitude when $t > 0$ is visibly higher than when $t < 0$. This asymmetry is due to the slow absorption recovery of the SESAM after the pulse [46]. The wings of the stationary

pulse decay exponentially both in the time domain and the frequency domain, which indicates that we are operating in the soliton regime. The FWHM bandwidth is 2.08 THz or 17 nm, with a central wavelength of 1564 nm, as shown in Fig. 3.4.

3.3 RF Spectrum Analysis

We now describe our model of the RF detection system, illustrated in Fig. 3.5.

We first define the input signal to the spectral analyzer, $I(T)$.

As shown in Fig. 3.4, the stationary pulse has bandwidth of 2.08 THz. The repetition frequency of the comb laser is 300 MHz. By comparison, the response time of a typical photodetector is ~ 10 ps which corresponds to a bandwidth of 100 GHz [53, 54]. However, the cut-off frequency of the low-pass filter in the spectrum analyzer is expected to be no higher than ~ 1 GHz. In addition, during the experiments, the frequency range of interest is only about 30 MHz, which is far below the repetition frequency of the comb laser (300 MHz). Hence, the frequency components that we detect are below 100 MHz, and in our computations, we set the input signal to the spectrum analyzer in Fig. 3.5 equal to the integrated energy over each round trip

$$I(T) = \begin{cases} \eta \int_{-T_R/2}^{T_R/2} |u_p(t, T)|^2 dt, & T = 0, 1, 2, \dots, \\ 0, & \text{otherwise.} \end{cases} \quad (3.12)$$

Since we do not have an absolute calibration available for the output current, we set $\eta = 1$ in our computations for convenience.

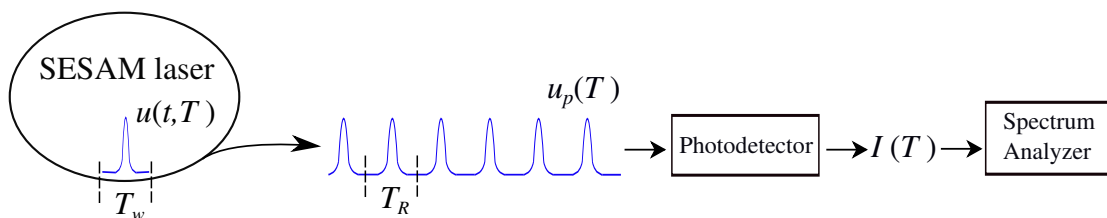


Figure 3.5: Illustration of unwrapping the optical field $u(t, T)$ to obtain $u_p(T)$ and $I(t)$, where T_w is the computational time window and T_R is the round trip time.

3.3.1 The Heterodyne Spectrum Analyzer

In Fig. 3.6, we show a schematic illustration of the heterodyne spectrum analyzer that we model [55].

The spectral analyzer model includes two basic components: (1) the RF signal processing unit and (2) the detection and display unit. During RF signal processing, the input signal $I(T)$ first passes through a low-pass filter to eliminate the fast oscillations that are outside the bandwidth of interest. Then, the filtered signal is mixed with a local oscillator, S_{LO} , whose frequency can be tuned during the measurements. Next, the mixed signal $I_m(T)$ passes through an intermediate-frequency filter (IF), which is a fixed narrow pass-band filter that extracts a single frequency component in the mixed signal. The bandwidth of the IF filter is called the resolution bandwidth (RBW), B_{IF} . The envelope detector and the low-pass video filter detect the magnitude of each signal component that is extracted, and converts the signal to a current signal $I_V(T)$. Finally, the signal $I_V(t)$ is detected and displayed

on the monitor of the spectrum analyzer.

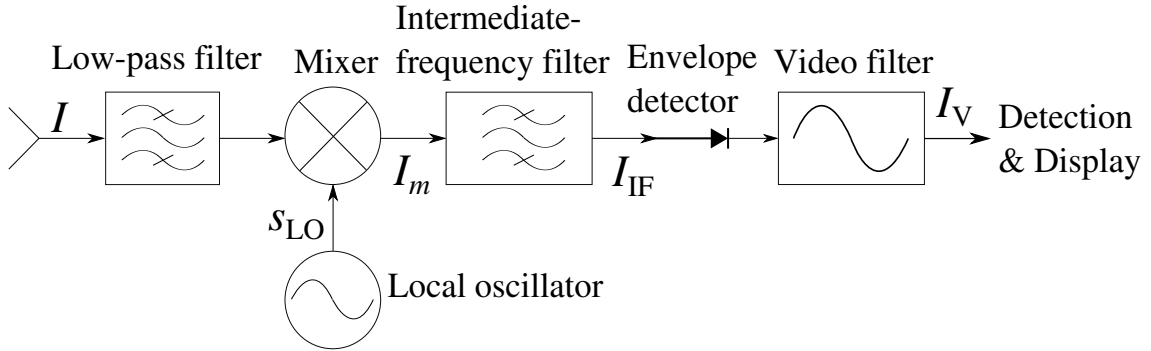


Figure 3.6: Illustration of a heterodyne spectrum analyzer.

Next, we describe in more detail our mathematical model of each of these components. The system parameters of the heterodyne spectrum analyzer that we use in our computations are listed in Table 3.2.

1. RF signal processing

An RF heterodyne spectrum analyzer uses a sweep-tune procedure. By tuning the frequency of the local oscillator in a given time duration, referred to as a time bucket, the magnitude of the corresponding frequency component of the input signal is measured. The duration of the time bucket should be sufficiently long to capture the oscillation within the resolution bandwidth.

The number of trace points N_{tr} on a display screen implies the appropriate time bucket duration

$$\text{Time bucket duration} = T_{\text{sweep}}/N_{tr}, \quad (3.13)$$

Parameter			Value
Sweep time, T_{sweep}			3.33 ms (1×10^6 round trips)
Display trace points, N_{tr}			400
Frequencies of measurement			$F_{\text{min}} = 0, F_{\text{max}} = 100$ MHz
Frequency bucket width			250 KHz
Time bucket			$8.33 \mu\text{s}$ (2500 round trips)
Local oscillator	Frequency tuning range	f_{LO}	7.75 MHz – 100 MHz
	Tuning increment	Δf	125 KHz
IF filter	Center frequency	f_{IF}	100 MHz
	Resolution bandwidth	B_{IF}	300 KHz
Video filter	Center frequency	f_{V}	0
	Video filter bandwidth	B_{V}	300 KHz

Table 3.2: Modeling parameters of the heterodyne spectrum analyzer.

where T_{sweep} is the sweep time, which is the time duration that is required to record the frequency spectrum of interest

$$T_{\text{sweep}} = k (F_{\text{max}} - F_{\text{min}}) / B_{\text{IF}}^2, \quad (3.14)$$

in which $F_{\text{min}} = 0$ and $F_{\text{max}} = 100$ MHz defines the entire frequency range of measurement, $k = 3$ is the proportionality parameter [55, 56], and $B_{\text{IF}} = 300$ KHz is the bandwidth of the IF filter.

As shown in Fig. 3.6, the input signal $I(T)$ is first mixed with a local oscillator

$$I_m(T) = I(T)s_{\text{LO}}(T) = I(T)\cos(2\pi f_{\text{LO}}T), \quad (3.15)$$

where I_m is the mixed signal and f_{LO} is the oscillation frequency. The mixed signal $I_m(T)$ then passes through an intermediate-frequency (IF) filter

$$I_{\text{IF}}(T) = I_m(T) \otimes h_{\text{IF}}(T), \quad (3.16)$$

where $h_{\text{IF}}(T)$ is the impulse response of the IF filter and the symbol \otimes represents convolution. Here, we use a 13th-order Bessel band-pass filter [57] as the IF filter.

The signal $I_{\text{IF}}(T)$ is then converted to a video signal $I_V(T)$ using an envelope detector and a video filter

$$I_V = \text{Re} \left\{ [2 |I_{\text{IF}}(T)|^2 \otimes h_V(T)]^{1/2} \right\}, \quad (3.17)$$

where $h_V(T)$ is the impulse response of the video filter. In our simulation, we set $h_V(T) = h_{\text{IF}}(T)$.

2. Detection and display

The local oscillator is tuned by an increment Δf so that the measurement can cover the entire frequency range of interest. Every increment of the local oscillator will eventually lead to a measurement I_{Vl} , where $l = 1, 2, \dots$. The number of frequency increments from the measurements is usually greater than the screen resolution, i.e., the number of trace points N_{tr} for the frequency components.

The rule that the spectrum analyzer uses to decide the magnitude of the frequency components that are displayed is determined by the detection mode [56]. The frequency range is divided into N_{tr} frequency buckets. Thus, the width of the frequency bucket is set as

$$\text{Frequency bucket width} = (F_{\text{max}} - F_{\text{min}}) / N_{\text{tr}}. \quad (3.18)$$

In our simulations, we set the total number of measurement inside each frequency bucket as $J = 2$. In our simulations, we use the average detection mode, in which the magnitude for the k th trace point is obtained as

$$I_V^{(k)} = \frac{1}{J} \sum_{j=1}^J I_{Vj}, \quad (3.19)$$

where I_{Vj} is the j th measurement inside the k th frequency bucket.

3.3.2 The output RF spectrum

In Fig. 3.7, we show the experimental display trace of the spectrum analyzer in the experiments [58]. We also show the simulated spectrum $I(t, T)$. The sidebands are clearly visible. As the pump power increases, the offset frequency shifts, and the power in the wake mode sidebands increases. The laser becomes unstable when the pump power $P_{\text{pump}} > 255$ mW. When $P_{\text{pump}} = 255$ mW, the sidebands are centered at 19.5 MHz, and the magnitude of the sidebands is about -10 dBm above the background noise.

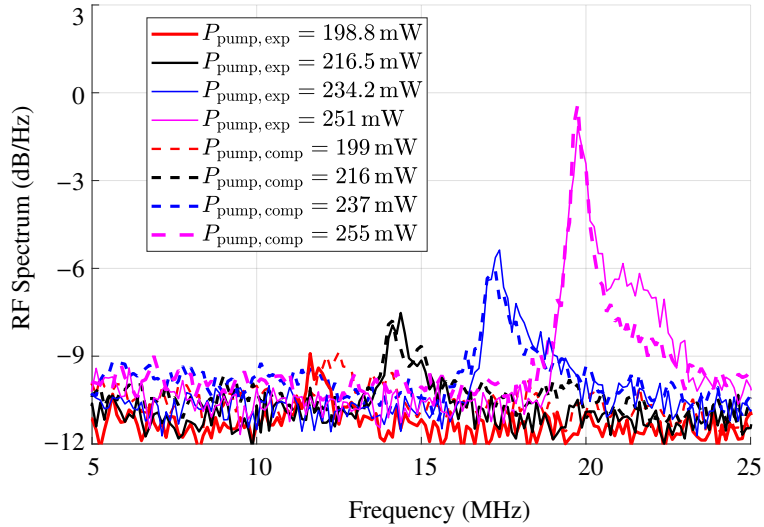


Figure 3.7: Comparison of the experimentally-observed and the computationally-calculated RF spectrum. The agreement is excellent.

3.4 Summary

In this section, we used a lumped model and a heterodyne spectrum analyzer model to compute the RF spectrum for a SESAM laser. We compared the result to the experimentally observed RF spectrum and agreement was excellent. In particular, we reproduced both the frequency shift of the wake mode sidebands, and their relative power.

In principle, we could use this result as the starting point for a detailed system optimization. In practice, the lumped model is too computationally slow to be used for this purpose. Using a high-performance computational cluster [59] in which we used up to 256 computing cores in parallel, we found that calculating the RF

spectrum for one set of parameters requires approximately two hours.

In the next three chapters, we use an averaged model for the SESAM fiber comb laser. In combination with dynamical methods that we described in Chapter. 2, the averaged model allows us to determine the stable operating regime and to optimize the parameters of the SESAM laser system. We then use the lumped model to verify the results of the averaged model in particular cases.

CHAPTER 4

Stability of Passively Modelocked Lasers with Slow Saturable Absorbers

In Chapter 2, we described boundary tracking algorithms to rapidly determine the stability and map out the regions of stable operation for passively modelocked lasers with fast saturable absorption. In Chapter 3, we described passively modelocked lasers with slow saturable absorbers using an example of a SESAM fiber comb laser. In this chapter, we find the conditions for stable operation of this laser.

The SESAM fiber comb laser operates in the soliton regime where, to lowest order, the pulse shape is determined by the balance between the Kerr nonlinearity and chromatic dispersion [45, 60]. Kärtner et al. [45] used soliton perturbation theory to study the stability of this laser, and they first predicted the wake mode instability. We have examined the wake mode instability computationally using realistic pulse parameters [60] in order to determine the parameters at which it sets in and its evolution. We find that this instability leads to a quasi-periodic appearance and disappearance of pulses in which a new pulse grows in the wake of

an already-existing pulse and ultimately steals energy from it, causing it to decay and ultimately disappear. This instability sets a lower limit on the magnitude of the chromatic dispersion and an upper limit on the pump power, which in turn set a lower limit on the pulse duration and an upper limit on the pulse energy.

4.1 An Averaged Model

The starting point for an averaged model of the SESAM laser is Eq. (1.1), where the saturable absorber function $f_{\text{sa}}(|u|)$ becomes [45, 60]

$$f_{\text{sa}}(|u|) = -\frac{\rho}{2}nu, \quad (4.1)$$

and the parameter n obeys the equation

$$\frac{\partial n(t, T)}{\partial t} = \frac{1 - n}{T_A} - \frac{|u(t, T)|^2}{w_A}n, \quad (4.2)$$

where ρ is a constant, and w_A is the saturation energy of the SESAM. This equation is similar to Eq. (3.10), but is averaged over one round trip in the laser. Physically, the parameter n corresponds to the fraction of absorbing ions that are in the lower state of a two-state system, while ρ is the absorption coefficient of the SESAM.

The system parameters are the same as in Chapter 3 and are listed in Table 4.1. The values of parameters T_R and β'' are measured experimentally and the values of l , T_A , and ρ are evaluated based on the SESAM datasheet [49]. The Kerr coefficient is obtained using $\gamma = 2\pi\kappa L/(\lambda A_{\text{eff}})$, where we estimate $\kappa = 2.5 \times 10^{-20} \text{ m}^2/\text{W}$, the total fiber length $L = 70 \text{ cm}$, $\lambda = 1560 \text{ nm}$, and the average beam diameter in the fiber is $9 \mu\text{m}$. We estimate the gain saturation power P_{sat} based on the

T_R	3.33 ns	w_A	157 pJ	P_{sat}	9.01 mW
g_0	7.74	ρ	0.0726	β''	-0.0144 ps ²
ω_g	30 ps ⁻¹	T_A	2.00 ps	γ	0.00111 W ⁻¹
l	1.05				

Table 4.1: Value of parameters we use in Eqs. (1.1), (1.3), (4.1), and (4.2).

the pump power vs. output power (shown later in Fig. 4.6), and we evaluate the SESAM saturation energy using $\omega_A = \Phi_{\text{sat}} A_{\text{eff,SESAM}}$, where the saturation fluence is reported as $\Phi_{\text{sat}} = 50 \mu\text{J}/\text{cm}^2$ [49], and the measured spot area inside the SESAM is $A_{\text{eff,SESAM}} = 314 \mu\text{m}^2$. We select the values for g_0 and ω_g that provide the best agreement with the experimentally-measured average output power.

We use a modified split-step Fourier method [37] to solve Eqs. (1.1) and (4.1) when using the evolution method. Starting from noise, we obtain the evolution profile that is shown in Fig. 4.1. Due to the asymmetric temporal response of the SESAM, the cavity net gain $G_n = \exp[g(|u|) - l - \rho n(t)]$ is also asymmetric, as shown in Fig. 4.2, so that the centroid t_c in the computational time window moves. We have removed the centroid motion in Fig. 4.1. In Fig. 4.1(a) we show that a stable modelocked pulse appears after about 500 round trips (1.67 μs). In the frequency domain, shown in Fig. 4.1(b), only a narrow spectrum is present under the gain peak—corresponding to a noisy continuous wave—for about 250 round trips. At that point, the power in the exponentially growing noise is sufficiently large that

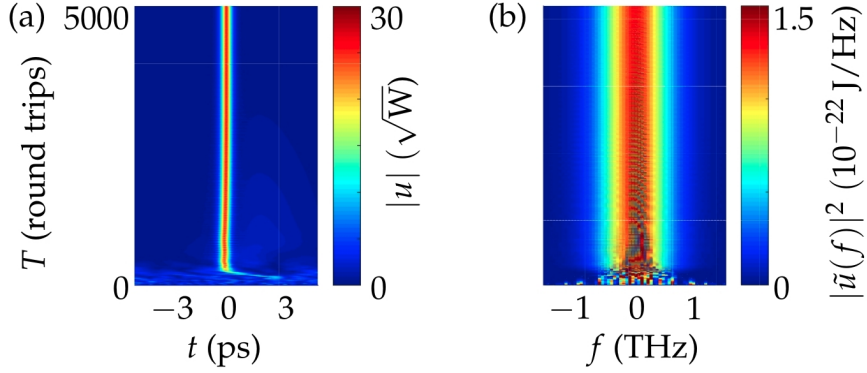


Figure 4.1: Starting from noise, the system of Eq. (1.1) evolves to a stable profile in the (a) time domain and (b) frequency domain, where $\tilde{u}(f) = \int_{-T_R/2}^{T_R/2} u(t) \exp(-2i\pi ft) dt$.

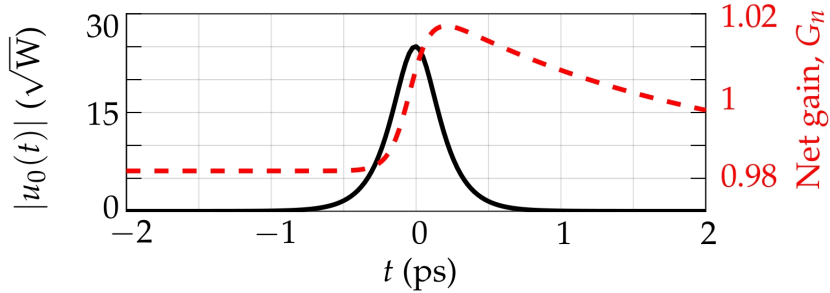


Figure 4.2: The stationary pulse u_0 and the net gain, $G_n = \exp [g(|u_0|) - l - \rho n(t)]$, which exhibits an asymmetric profile due to the SESAM. A net gain window exists when $G_n > 1$.

sidebands are generated nonlinearly, and a stable pulse forms.

The full-width-at-half-maximum (FWHM) of the stable pulse in Fig. 4.2 is 254 fs, the peak amplitude is $25.0 \text{ W}^{1/2}$, and the pulse energy is 181 pJ. The experimen-

tally-measured average laser output power is 4.88 mW with a pump power of 234 mW. The output coupling ratio is 9% [23], from which we estimate that the cavity pulse energy is 185 pJ.

4.2 Wake Mode Instability

As we previously discussed, wake modes can grow inside the net gain window that is visible in Fig. 4.2. As a wake mode grows, the dispersion carries it away from the pulse, so that it ultimately experience loss. Thus, dispersion is necessary to attenuate the wake modes [46]. The long response time of the SESAM relative to the pulse duration plays an important role here. When the SESAM response time becomes comparable to the pulse duration, as is the case in picosecond bulk lasers, the wake instability is no longer observed [61].

The pulse is destabilized by wake modes when the unsaturated gain becomes sufficiently large or the group-delay dispersion (GDD) β'' becomes sufficiently small. In Fig. 4.3, we show an example in which g_0 is increased to 13.5. We observe a quasi-periodic evolution in the time domain, as shown in Fig. 4.3(a). We show in four sub-figures, Figs. 4.3 (c), (d), (e), and (f), an example of the amplitude evolution profile in detail. A second pulse, ②, forms in the wake of the original pulse, ①, and grows at its expense, ultimately leading to the disappearance of the original pulse. A third pulse, ③, then begins to grow in the wake of pulse ②, and the process continues indefinitely [46]. We show the frequency domain in Fig. 4.3(b). The spec-

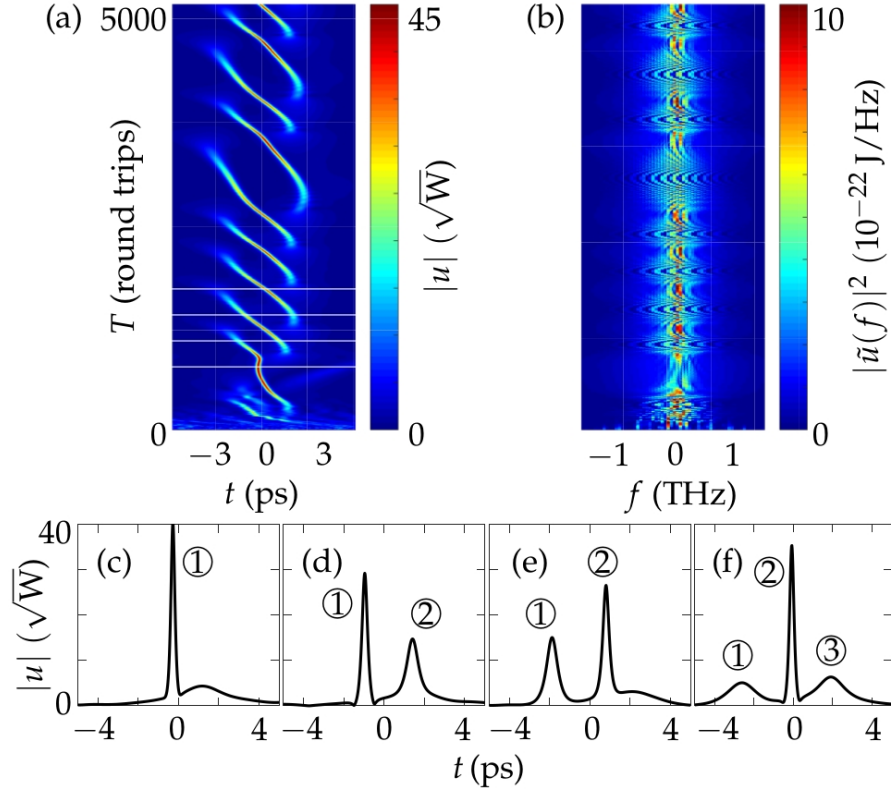


Figure 4.3: The evolution profile of the wake mode instability (a) in the time domain, and (b) in the frequency domain, (see Visualization 1), and the pulse amplitude profile at (c) $T = 823$, (d) $T = 948$, (e) $T = 1073$, and (f) $T = 1198$. The locations of profiles (c), (d), (e), and (f) are marked by white lines in (a).

trum has approximately the same width as in Fig. 4.1(b), but undergoes a complex and incoherent evolution. We show an animation of this evolution in Visualization 1. Thus, this instability sets a lower limit on the magnitude of the group velocity dispersion and an upper limit on the pump power (unsaturated gain) for stable op-

eration, which in turn set a lower limit on the pulse duration and an upper limit on the pulse energy. Hence, modelocked lasers that use slow saturable absorbers generally become unstable as the group delay dispersion approaches zero. By contrast, lasers using fast saturable absorbers can operate with net zero dispersion [7, 62–64].

We can accurately determine the threshold for the onset of the wake instability using the boundary tracking algorithms that are described in Chapter 2. In this approach, we find a stationary solution $[u_0, \phi, t_s]$ of Eq. (1.1), which corresponds to a modelocked pulse. We then linearize Eq. (1.1) about this solution, and we determine the eigenvalues (dynamical spectrum) and eigenvectors of this linearized equation. Accurately calculating these wake mode eigenvalues and the wake mode profiles is similar to solving the discrete modes that we have described in Sec. 2.2.1. We have shown an example of the eigenmode profiles in [11].

In Fig. 4.4, we show the dynamical spectrum near the origin for the SESAM laser with the same parameters that we used in Table 4.1. The spectrum has two branches corresponding to continuous wave perturbations, as well as four discrete eigenvalues that correspond to perturbations of the stationary pulse’s central time (λ_t), central phase (λ_ϕ), central frequency (λ_f), and amplitude (λ_a), respectively, similar to what is found in soliton perturbation theory [65]. However, there are two additional discrete eigenvalues λ_{w+} and λ_{w-} that correspond to the wake modes [11], as shown in Fig. 4.4.

As we mentioned in Chapter 2, the stationary pulse is unstable when any eigenvalue(s) have a positive real part [10]. Both λ_t and λ_ϕ remain at the origin due to the time and phase invariance of Eq. (1.1). We see from Fig. 4.4 that when

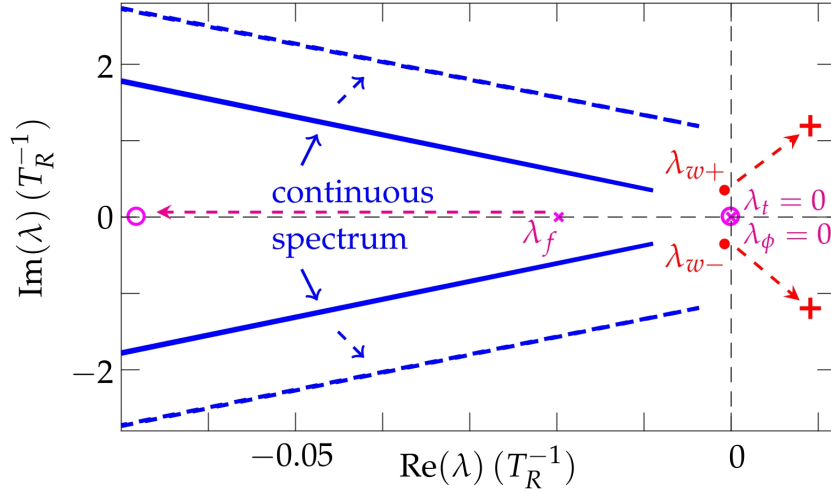


Figure 4.4: The variation of the dynamical spectrum when the unsaturated gain g_0 increases from 1.90 to 2.70. We find that $\lambda_{w\pm} = -7.75 \times 10^{-4} \pm 0.352i$ when $g_0 = 7.74$ and $\lambda_{w\pm} = 9.09 \times 10^{-3} \pm 1.19i$ when $g_0 = 13.5$. The dashed arrows indicate how the spectrum shifts as g_0 increases from 7.74 to 13.5. The eigenvalue $\lambda_a < -0.90$ is not shown here.

$g_0 = 7.74$, the real parts of the continuous spectrum are negative and the discrete eigenvalues λ_f and λ_a are both negative. In addition, the wake mode eigenvalues are given by $\lambda_{w\pm} = -7.75 \times 10^{-4} \pm 0.352i$, as shown in Fig. 4.4. Hence, the system is stable and close to the stability boundary in the parameter space. The wake modes are bounded modes that decay slowly in T than the repetition rate $1/T_R$, where the decay rate is given by

$$f_{\text{decay}} = \frac{\text{Re}(|\lambda_{w\pm}|)}{2\pi T_R}. \quad (4.3)$$

The stationary pulse becomes unstable when the unsaturated gain g_0 becomes sufficiently large. In Fig. 4.4, we use dashed arrows to show how the dynamical spectrum shifts when g_0 increases up to 13.5. We find that all eigenvalues have negative real parts except for the wake mode eigenvalues, for which $\lambda_{w\pm} = 9.09 \times 10^{-3} \pm 1.19i$. The positive real part of $\lambda_{w\pm}$ indicate that the wake modes will grow, destabilizing the stationary pulse.

In Fig. 4.5, we show the stable regions in the (g_0, β'') parameter space. When the group delay dispersion coefficient β'' varies from -0.03 ps^2 to zero, there exist two stability boundaries. For a given value of β'' , the pulse becomes unstable due to the background radiation (continuous modes) [10] (when g_0 becomes sufficiently small). In this case, the system gain is below the modelocking threshold. When g_0 becomes sufficiently large, the pulse becomes unstable due to the wake modes. The instability threshold for g_0 decreases as the system approaches zero dispersion. When $\beta'' = 0$, the pulse is in principle stable in a very narrow range of g_0 , $1.14 < g_0 < 1.18$. In practice, this range is so narrow that a laser that operated within it would be destabilized by noise and other perturbations. In addition, the pulse width of the stationary pulse is $\tau_p > 3 \text{ ps}$, which is longer than the SESAM recovery time, $T_A = 2 \text{ ps}$. This operating state of the SESAM is inefficient because the saturable absorption that the pulse experiences is strongly offset by the lower-level population recovery.

The real parts of the dynamical spectrum that we show in Fig. 4.4 indicate the growth rate of the eigenmodes, while the imaginary part of the spectrum indicates their phase shift per round trip with respect to the stationary pulse. In the

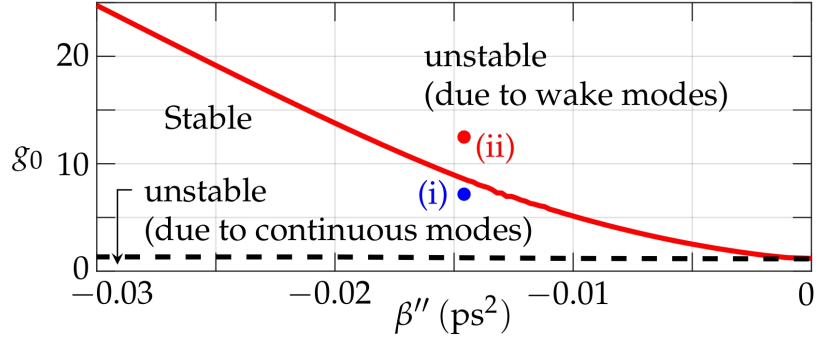


Figure 4.5: Stability boundaries in the parameter space of the unsaturated gain g_0 and the group velocity dispersion β'' . The points (i) and (ii) indicates the cases $g_0 = 7.74$ and $g_0 = 13.5$, respectively, with $\beta'' = -0.0144 \text{ ps}^2$.

presence of noise, the eigenmodes with non-zero imaginary eigenvalues introduce a frequency modulation of the modelocked spectrum, which can be observed in the power spectrum as sidebands. We have shown the profile of the sidebands in [58] when observed using a radio frequency (RF) spectrum analyzer. We described our model of the spectrum analyzer in Chapter 3.

Here, we show that the dynamical method with an averaged model accurately predicts the locations of the wake mode sidebands. The frequency offset of the wake mode sidebands can be predicted from the value of the imaginary part of $\lambda_{w\pm}$,

$$f_{\text{sb}} = \frac{\text{Im}(|\lambda_{w\pm}|)}{2\pi T_R}. \quad (4.4)$$

In Fig. 4.6, we show the variation of the output power of the SESAM laser, as well as the frequency offset of the sidebands with respect to each comb line as the unsaturated gain increases. We see that, as the pump power P_{pump} increases from

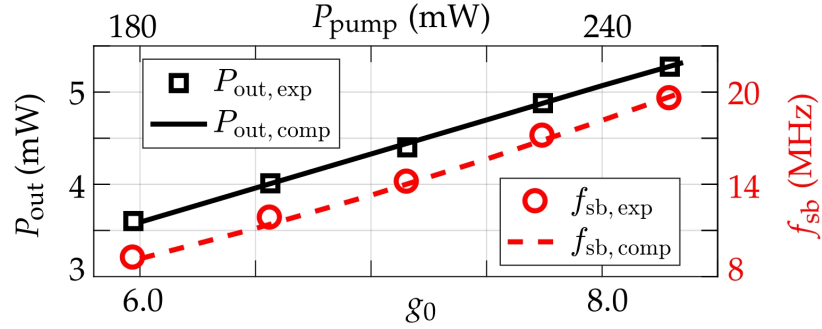


Figure 4.6: The variation of the output power P_{out} and the sidebands' frequency offset f_{sb} as the unsaturated gain g_0 increases.

The stationary pulse becomes unstable when $g_0 = 8.5$.

180 mW to 250 mW, the laser output power $P_{\text{out,exp}}$ increases almost linearly from 3.6 mW to 5.3 mW. Meanwhile, the frequency offset of the wake mode sidebands $f_{\text{sb,exp}}$ increases from about 9 MHz to about 20 MHz. There is good agreement between theory and experiment. We find that the laser becomes unstable due to the wake mode instability when $g_0 > 8.5$. In addition, we observe that the pump power is linearly proportional to g_0 , i.e., $P_{\text{pump}} \approx 30 \text{ mW} \times g_0$. The linear scale suggests that the upper state population of the erbium-doped fiber is not completely depleted in this case.

4.3 Summary

In this chapter, we have described the wake modes and their effect on stationary pulses in modelocked lasers with slow saturable absorbers using an averaged model. A gain window forms behind the pulse, and wake modes can grow in this

gain window. The modelocked pulses become unstable when the wake modes are not swept away from the pulse by dispersion or attenuated by the background loss. Using a dynamical analysis, we show that this instability occurs when the eigenvalues in the dynamical spectrum that correspond to the wake modes have a positive real part. When the laser parameters are close to the stability boundary for the wake modes, the wake modes generate sidebands in the output RF spectrum. We demonstrate that the dynamical spectrum can accurately predict the frequency offset of the wake mode sidebands. In the next chapter, we quantitatively model the growth of the sidebands' magnitude as the pump power increases using both the evolutionary approach and the dynamical approach.

CHAPTER 5

Evaluating the Impact of Noise

We will now add a perturbative noise source $s(t, T)$ to our modelocked laser models. The system equation of a modelocked laser system is a stochastic nonlinear equation,

$$\frac{\partial u}{\partial T} = \hat{F}(u)u + s, \quad (5.1)$$

where \hat{F} is a deterministic nonlinear operator and $s(t, T)$ is a random process. In the particular case of the HME, Eq. (1.1), we have

$$\hat{F}(u) = -i\phi - \frac{l}{2} + t_s \frac{\partial}{\partial t} + \frac{g(|u|)}{2} \left(1 + \frac{1}{2\omega_g^2} \frac{\partial^2}{\partial t^2} \right) - \frac{i\beta''}{2} \frac{\partial^2}{\partial t^2} + i\gamma|u|^2 + f_{\text{sa}}(u), \quad (5.2)$$

where $s(t, T)$ is a wide-sense stationary Gaussian process that represents the amplified spontaneous emission (ASE) noise from the gain medium [9].

When the noise term $s(t, T)$ is neglected in Eq. (1.1), and we assume that the

parameters satisfy the relations

$$\frac{\delta\beta''}{\gamma} = \frac{g(|u_0|)}{2\omega_g^2},$$

$$t_s = \beta''\omega_{\text{off}}\omega_g, \tag{5.3}$$

$$g(|u_0|) - l = -\frac{g(|u_0|)}{2\omega_g^2}(\gamma A_0^2 - \beta''\omega_0^2),$$

then we find that Eq. (1.1), or $\hat{F}(u) = 0$ as in Eq. (5.2), has the stationary solution [26],

$$u_0(t, T) = A_0 \text{sech}(t/\tau_0) \exp[-i\omega_0(t - t_0) + i\theta_0],$$

$$\omega_0 = \omega_{\text{off}}\omega_g, \tag{5.4}$$

$$\phi = \frac{1}{2}(\gamma A_0^2 - \beta''\omega_0^2),$$

$$\tau_0 = \sqrt{|\beta''|/\gamma}/A_0,$$

where $A_0 > 0$ is an arbitrary variable that determines both the amplitude and the duration of the stationary pulse, and where t_0 and θ_0 are the initial pulse centroid in t and the initial optical phase which can be arbitrary values. Given this special choice of parameters, soliton perturbation theory [38] can be applied to the HME to determine the stability of the stationary solution [9, 15, 45, 66]. In addition, with the same parameter choice, the HME can be reduced to two pairs of Gordon processes that describe the propagation dynamics of the pulse energy, phase, frequency, and central time, from which the phase jitter, timing jitter, frequency jitter, and energy fluctuations can be calculated analytically [9, 67]. These analytical results have been widely used to estimate the noise performance of passively modelocked laser systems.

There are two difficulties with this approach. The first is that the expression for $f_{\text{sa}}(u)$ in Eq. (1.4) is too simple to be realistic, and it predicts that the pulse

solution is stable in only a small region in the parameter space, which is contrary to experimental results [15, 44, 68]. More complex models that predict larger regions of stability and that better match the experiments have been studied [4, 18, 33–36, 69, 70]. However, with the exception of the work in [70], all this work relies on an evolutionary approach, which can be computationally inefficient and can lead to ambiguous results. Second, even given the expression for $f_{\text{sa}}(u)$, there is no reason to expect the special parameter relation that is given in Eq. (5.3) to hold. In fact, short-pulse lasers vary widely—using different types of gain media, saturable absorbers, and cavity designs. There is a need for computational tools that are sufficiently powerful to be able to cope with the broad range of short-pulse laser designs.

Despite the importance of characterizing the noise in short-pulse lasers, there have been relatively few computational studies of their noise performance. The computational studies that have been carried out use Monte Carlo simulations in which the evolution equations are repeatedly solved with different noise realizations [67, 71–73]. Convergence of this procedure is slow, and it is too computationally intensive to be used for systematic optimization.

In this chapter, we extend the work in [11] to study the noise performance of short-pulse lasers using dynamical methods. We describe in detail the computational procedure and quantitatively compare the computational performance of our dynamical approach with Monte Carlo simulations.

5.1 The Dynamical Method

In this section, we will briefly review the dynamical method that we have described thus far.

In the laser systems that we are considering, the evolution of the pulse envelope can be described by a nonlinear equation that has the form

$$\frac{\partial u(t, T)}{\partial T} = \hat{F}[u(t, T), u^*(t, T)] + s(t, T), \quad (5.5)$$

where $\hat{F}(u, u^*)$ is a nonlinear function of the wave envelope u and its complex conjugate u^* . In nearly all cases, the variable u^* appears with one power less than u in each term of F . That is the case for Eq. (1.1) as well as for the models of fast saturable absorption that were considered in [70]. It is also implicitly the case for the model of a slow saturable absorber as we discussed in Eqs. (4.1) and (4.2).

Following the discussion in Sec. 2.1.2, we obtain the linearized equation and the eigenvalue problem

$$\frac{\partial \Delta \mathbf{u}}{\partial T} = \mathbf{L} \Delta \mathbf{u} + \mathbf{s} = \lambda \Delta \mathbf{u} + \mathbf{s}, \quad (5.6)$$

where

$$\Delta \mathbf{u} = \begin{bmatrix} \Delta u \\ \Delta \bar{u} \end{bmatrix}, \quad \mathbf{L} = \begin{bmatrix} \mathbf{L}_{11} & \mathbf{L}_{12} \\ \mathbf{L}_{21} & \mathbf{L}_{22} \end{bmatrix}, \quad \mathbf{s} = \begin{bmatrix} s \\ s^* \end{bmatrix}, \quad (5.7)$$

and where $\mathbf{L}_{11} = \delta F / \delta u$, $\mathbf{L}_{12} = \delta F / \delta u^*$, $\mathbf{L}_{21} = \delta F^* / \delta u$, and $\mathbf{L}_{22} = \delta F^* / \delta u^*$ are functional derivatives. Again, if any eigenvalue(s) have a positive real part, the system is unstable.

In any practical laser system, the noise $s(t, T)$ is a small perturbation. Indeed, it is typically so small that it is necessary to artificially increase it in order to obtain reliable results from Monte Carlo simulations [4]. The essence of our method is that the amplitudes of the spectral components—the solutions to Eq. (5.6)—obey simple Langevin equations that can be solved for all times T . The means and variances of these amplitudes can then easily be found. After expanding the statistical quantities of interest such as the phase jitter, the timing jitter, and the energy fluctuation as a linear sum of these amplitudes, we obtain the means and variances of these statistical quantities.

5.1.1 Discretization

When we discretize the time domain t for computation, we use an evenly spaced grid of N points in t , whose spacing we denote as Δt , where $\Delta t = T_w/N$ and T_w is the duration of the computational time window.

Issues related to choosing Δt and N as well as discretizing the operator \mathbf{L} to ensure the accuracy of the solution have been discussed in [10]. Here, in order to ensure reasonable accuracy, we choose T_w so that it is approximately 100 times the duration of the modelocked pulse, and we choose $N \geq 1024$. We always choose T_w and N sufficiently large so that the visible impact on any plotted result is negligible.

In analytical studies of the stability and noise performance of passively mode-locked lasers, it is usual to choose an infinite domain in the fast time t , in which case the spectrum of \mathbf{L} has both continuous components (essential spectrum) as well

as discrete components (point spectrum) [10, 39]. In real-world lasers, the actual domain is periodic in the round trip time T_R , and in computational work, it is usual to study a time domain T_w that is small compared to T_R , so that $T_w \ll T_R$. As a consequence, the computational problem only has a point spectrum.

Once the system has been discretized, both $\Delta u(t)$ and $\Delta \bar{u}(t)$ become N -dimensional vectors in which $\Delta u_l = u(t_l)$ and $\Delta \bar{u}_l = \bar{u}(t_l)$, $l = 1, 2, \dots, N$. The vector $\Delta \mathbf{u}$ in Eq. (5.6) becomes a $2N$ -dimensional vector $\Delta \mathbf{u}$ in which the first N elements correspond to Δu_l , $l = 1, 2, \dots, N$ and the last N elements correspond to $\Delta \bar{u}_l$, $l = 1, 2, \dots, N$, i.e., $\Delta \mathbf{u} = [\Delta u_1, \Delta u_2, \dots, \Delta u_N, \Delta \bar{u}_1, \Delta \bar{u}_2, \dots, \Delta \bar{u}_N]^T$, where T denotes the transpose. The operator \mathbf{L} becomes a $2N \times 2N$ matrix [10].

5.1.2 Spectral Decomposition

We will denote a set of independent eigenvectors as $\mathbf{e}_j = [e_j, \bar{e}_j]^T$, where T denotes the transpose and $e_{jl} = e_j(t_l)$ and $\bar{e}_{jl} = \bar{e}_j(t_l)$, so that each eigenvector \mathbf{e}_j is a $2N$ -dimensional vector. In all the laser problems that we have considered, the set of eigenvectors \mathbf{e}_j is complete, i.e., there are $2N$ independent eigenvectors, which span the $2N$ -dimensional complex vector space upon which \mathbf{L} operates [74], so that we may decompose any $\Delta \mathbf{u}$ as

$$\Delta \mathbf{u} = \sum_{j=1}^{2N} c_j \mathbf{e}_j, \quad (5.8)$$

where the c_j are complex constants. We find that if λ_j is an eigenvalue, then so is $\lambda'_j = \lambda_j^*$ and if $\mathbf{e}_j = [e_j, \bar{e}_j]^T$, then the eigenvector corresponding to $\lambda'_j = \lambda_j^*$ is given by $\mathbf{e}'_j = [\bar{e}_j^*, e_j^*]^T$ [11]. In general $\bar{e}_j \neq e_j^*$. However, when λ_j is real, then we find

$$\bar{e}_j = e_j^*.$$

In order to find the c_j , given $\Delta \mathbf{u}$, we must define an inner product. For any two given vectors \mathbf{p} and \mathbf{q} in the $2N$ -dimensional space, the natural inner product becomes

$$\sum_{j=0}^N (p_j^* q_j + \bar{p}_j \bar{q}_j^*) \Delta t = \mathbf{p}^H \mathbf{q} \Delta t, \quad (5.9)$$

where \mathbf{p}^H is a $2N$ -dimensional row vector whose elements are complex conjugates of the vector \mathbf{p} .

We will denote the dual eigenvectors of the matrix \mathbf{L} as $\hat{\mathbf{e}}_j$. These are equal to the eigenvectors of \mathbf{L}^\dagger , the complex conjugate transpose of \mathbf{L} . The dual eigenvectors are normalized so that

$$\mathbf{e}_j^H \hat{\mathbf{e}}_k \Delta t = \delta_{jk}, \quad (5.10)$$

where δ_{jk} is the Krönecker delta-function. We now find that

$$c_j = \hat{\mathbf{e}}_j^H \Delta \mathbf{u}. \quad (5.11)$$

Since $\mathbf{L} \neq \mathbf{L}^\dagger$, so that \mathbf{L} is not self-adjoint, it is *NOT* generally the case that $\hat{\mathbf{e}}_j^H \hat{\mathbf{e}}_k \Delta t = \delta_{jk}$.

5.1.3 Noise Evolution

In this dissertation, we will consider white noise sources for which

$$\langle s(t, T) s^*(t', T') \rangle = D \delta(t - t') \delta(T - T'), \quad (5.12)$$

where $\langle \cdot \rangle$ denotes the emsemble average, and D is the diffusion coefficient. We also have $\langle s(t, T) s(t', T') \rangle = \langle s^*(t, T) s^*(t', T') \rangle = 0$. More complex noise sources can in

principle be built up using Eq. (5.12) as a starting point [75]. After discretization in t , Eq. (5.12) becomes

$$\langle s_l(T)s_m^*(T') \rangle = \langle s(t_l, T)s^*(t_m, T') \rangle = \frac{D}{\Delta t} \delta_{lm} \delta(T - T'), \quad (5.13)$$

where $s_l = s(t_l)$, and the $2N$ -dimensional vector \mathbf{s} becomes $\mathbf{s} = [s, \bar{s}]^T$, where $\bar{s}_l = s_l^*$.

After discretization, we can write the $2N$ -dimensional vector \mathbf{s} at any slow time T as

$$\mathbf{s}(T) = \sum_{j=1}^{2N} s_j(T) \mathbf{e}_j, \quad (5.14)$$

so that $s_j(T) = \hat{\mathbf{e}}_j^H \mathbf{s}(T)$. We now define D_{jk} using the relationship

$$\langle s_j(T)s_k^*(T') \rangle = (D\Delta t) \hat{\mathbf{e}}_j^H \hat{\mathbf{e}}_k \delta(T - T') \equiv D_{jk} \delta(T - T'), \quad (5.15)$$

where we note $D_{kj} = D_{jk}^*$.

In the presence of noise, the amplitudes of the spectral components of $\Delta \mathbf{u}$ that are defined in Eq. (5.8) evolve according to the simple Langevin equation

$$\frac{dc_j}{dT} = \lambda_j c_j + s_j, \quad (5.16)$$

where we note that $\text{Re}(\lambda_j) \leq 0$ in order for the modelocked pulse to be stable. Since we start from a stationary solution, we now have $\langle c_j(T=0) \rangle = 0$.

The covariances, which can be obtained by integrating Eq. (5.16) using the method of stochastic differential equations [76], become

$$\langle c_j(T)c_k^*(T) \rangle = -\frac{D_{jk}}{\lambda_j + \lambda_k^*} \left[1 - e^{(\lambda_j + \lambda_k^*)T} \right], \quad (5.17)$$

where we assume that the covariances are zero at $T = 0$. In the special case when $\lambda_j = \lambda_k = 0$, we obtain

$$\langle c_j(T)c_k^*(T) \rangle = D_{jk}T. \quad (5.18)$$

In the long-time limit as $T \rightarrow \infty$, Eq. (5.17) becomes

$$\langle c_j(T)c_k^*(T) \rangle = -\frac{D_{jk}}{\lambda_j + \lambda_k^*}. \quad (5.19)$$

The corresponding two-time correlation function as $T \rightarrow \infty$ is given by [76]

$$R_{jk}(\tau) = -\frac{D_{jk}}{\lambda_j + \lambda_k^*} [e^{\lambda_k^* \tau} \Theta(\tau) + e^{-\lambda_j \tau} \Theta(-\tau)], \quad (5.20)$$

where $\Theta(\tau)$ is the Heaviside step function that equals zero when $\tau < 0$, $1/2$ when $\tau = 0$, and 1 when $\tau > 0$. The corresponding power spectral density is given by the Fourier transform of $R_{jk}(\tau)$,

$$S_{jk}(f) = \frac{D_{jk}}{(\lambda_j - 2i\pi f)(\lambda_k^* + 2i\pi f)}, \quad (5.21)$$

Using Eqs. (5.17)–(5.19), it is possible to compute quantities of statistical interest such as the timing jitter and the phase jitter. Using Eqs. (5.20) and (5.21) it is then possible to calculate the power spectral densities of these quantities.

5.1.4 Noise Impact on Statistical Quantities of Interest

Given a statistical quantity of interest, $\Delta x(T)$, we begin by writing it as an inner product of an appropriate vector \mathbf{h}_x and the perturbation $\Delta \mathbf{u}(T)$,

$$\Delta x(T) = \mathbf{h}_x^H \Delta \mathbf{u}(T) \Delta t, \quad (5.22)$$

Some examples follow:

1. Energy jitter $\Delta w(T)$:

The energy jitter is given by

$$\begin{aligned}\Delta w(T) &= \int_{-T_R/2}^{T_R/2} dt [|u(t, T)|^2 - |u_0(t)|^2] \\ &= \int_{-T_R/2}^{T_R/2} dt [u_0(t)\Delta u^*(t, T) + u_0^*(t)\Delta u(t, T)],\end{aligned}$$

which becomes after discretization

$$\begin{aligned}\Delta w(T) &= \sum_{l=1}^N \Delta t [u_0(t_l)\Delta u^*(t_l, T) + u_0^*(t_l)\Delta u(t_l, T)] \\ &= \mathbf{h}_w^H \Delta \mathbf{u}(T) \Delta t\end{aligned}\tag{5.23}$$

where $\mathbf{h}_w = [u_0, u_0^*]^T$.

2. Frequency jitter $\Delta f_c(T)$ [77]:

We can calculate the change in the central frequency as

$$\Delta f_c(T) = \frac{1}{2iw_0} \int_{-T_R/2}^{T_R/2} dt \left[\frac{\partial u_0^*}{\partial t} \Delta u(t, T) - \frac{\partial u_0}{\partial t} \Delta u^*(t, T) \right],\tag{5.24}$$

which after discretization becomes

$$\Delta f_c(T) = \mathbf{h}_{f_c}^H \Delta \mathbf{u}(T) \Delta t,\tag{5.25}$$

where $\mathbf{h}_{f_c} = (i/w_0) [D_t u_0, D_t u_0^*]^T$, and D_t is a first-order differentiation matrix, which we obtain by using the Fourier transform to compute u_0 in the frequency domain, multiplying by the frequency, and then computing the inverse Fourier transform [78].

3. Timing and phase jitter:

The central time of a modelocked pulse is given by

$$\Delta t_c = \frac{1}{w_0} \int_{-T_R/2}^{T_R/2} dt t [u_0^*(t) \Delta u(t, T) + u_0(t) \Delta u^*(t, T)], \quad (5.26)$$

which after discretization becomes

$$\Delta t_c = \mathbf{h}_t^H \Delta \mathbf{u}(T) \Delta t, \quad (5.27)$$

where $\mathbf{h}_t = (1/w_0)[tu_0, tu_0^*]^T$.

From the timing jitter, we can define a phase jitter,

$$\Delta \psi = 2\pi \Delta t_c / T_R, \quad (5.28)$$

which corresponds to the phase jitter that is observed at radio frequencies after an optical signal is detected in a photodetector. In most experimental work, this quantity is simply referred to as the phase jitter. Paschotta [4] refers to it as the timing phase jitter to avoid confusion with the optical phase jitter, and we will do the same.

In general, for any vector \mathbf{h}_x , we can write

$$\mathbf{h}_x = \sum_{j=1}^{2N} h_{xj} \hat{\mathbf{e}}_j, \quad (5.29)$$

and combined with Eq. (5.22), the corresponding statistical quantity can be written as

$$\Delta x(T) = \Delta t \left(\sum_{j=1}^{2N} h_{xj} \hat{\mathbf{e}}_j \right)^H \sum_{k=0}^{2N} c_k(T) \mathbf{e}_k = \sum_{j=1}^{2N} h_{xj}^* c_j(T), \quad (5.30)$$

where the h_{xj} are defined by the expression

$$h_{xj} = \mathbf{e}_j^H \mathbf{h}_x \Delta t. \quad (5.31)$$

Following Eqs. (5.21) and (5.30), we can now calculate the power spectral density of $\Delta x(T)$,

$$S_x(f) = \sum_{j=1}^{2N} \sum_{k=1}^{2N} h_{x_j}^* h_{x_k} S_{jk}(f) = \sum_{j=1}^{2N} \sum_{k=1}^{2N} \frac{h_{x_j}^* h_{x_k} D_{jk}}{(\lambda_j - 2i\pi f)(\lambda_k^* + 2i\pi f)}, \quad (5.32)$$

in which we require $h_{x_l} = 0$ when $\lambda_l = 0$.

Defining $\delta c_j = dc_j/dT$, we have

$$\frac{d\Delta x}{dT} = \delta x(T) = \sum_{j=0}^{2N} h_{x_j}^* \delta c_j(T), \quad (5.33)$$

which approximates the change in $\Delta x(T)$ from one round trip to the next, since all statistical quantities of interest change slowly compared to the repetition time. The power spectral density of $\delta x(T)$ becomes

$$S_{\delta x}(f) = (2\pi f)^2 S_x(f). \quad (5.34)$$

The formalism in Eqs. (5.32) and (5.34) includes the contribution of the eigenvectors that correspond to the continuous spectrum, whose effects were neglected in the computational results in [79].

5.2 Noise Level Evaluation and Computational Efficiency Tests

Here, we compare the results of the Haus-Mecozzi method [9], the Monte Carlo method [67], and the dynamical method that we have described in Sec. 5.1. The statistical quantities that we will study are the energy jitter $\Delta w(T) = w(T) - w_0$, the frequency jitter $\Delta f_c(T) = f_c(T) - f_0$, and the timing phase jitter $\Delta t_c = t_c(T) - t_{c0}$, where w_0 , f_0 , and t_{c0} are the unperturbed energy, central frequency, and the central

time of the modelocked pulse. We first give a brief review of the three methods that we will compare. We then apply all three methods to the widely-used Haus modelocking equation (HME) and an averaged model of a SESAM fiber laser [23]. We show that the dynamical method provides significantly better agreement with the Monte Carlo method than does the Haus-Mecozzi method. We further show that the dynamical method is several orders of magnitude more computationally efficient than the Monte Carlo approach, where our metrics are the computational time and the memory (RAM) and storage usage.

5.2.1 Calculation Methods

We first review the three methods we use to calculate the noise impact on the statistical quantities of interest. These are: (1) the Haus Mecozzi method, which is analytical, (2) the Monte Carlo simulation method, which repeatedly solves the evolution equations with different noise realizations, and (3) the dynamical methods that we described in Sec. 5.1.

5.2.1.1 The Haus-Mecozzi Method

The Haus modelocking equation (HME) is the simplest and most widely used model for modelocked laser systems. We have presented the HME in Eqs. (1.1)–(1.4). In their analytical method, Haus and Mecozzi begin by assuming that the modelocked pulse $u_0(t)$ has a hyperbolic-secant pulse shape and—like the soliton solutions for the nonlinear Schrödinger equation—is completely characterized by

four parameters: the pulse energy and its central time, central phase, and central frequency. They next apply soliton perturbation theory to calculate the phase evolution in the presence of noise, and they show that the evolution of the pulse energy fluctuation Δw , the central optical phase fluctuation $\Delta\theta$, the central frequency fluctuation Δf_c , and the central time fluctuation Δt_c are governed by four stochastic differential equations [4,9],

$$\begin{aligned}
d\Delta w/dT &= r_w \Delta w + s_w, \\
d\Delta\theta/dT &= r_\theta \Delta w + s_\theta, \\
d\Delta f_c/dT &= r_f \Delta f_c + s_f, \\
d\Delta t_c/dT &= r_t \Delta f_c + s_t,
\end{aligned} \tag{5.35}$$

where the growth/decay coefficients are all real quantities,

$$\begin{aligned}
r_w &= 2\delta A_0^2 - g_1 w_0 + 2g_1 A_0^2 / (6\omega_g^2 \tau_0), \\
r_\theta &= \gamma A_0^2 / w_0, \\
r_f &= -g_{\text{sat}} / (3\omega_g^2 \tau_0^2), \\
r_t &= \beta'',
\end{aligned} \tag{5.36}$$

and for which $g_1 = g_{\text{sat}}^2 / (g_0 P_{\text{sat}} T_R)$, $g_{\text{sat}} = g(|u_0(t)|)$, and $w_0 = 2A_0^2 \tau_0$ is the energy of the modelocked pulse. The diffusion coefficients are defined as $\langle s_x(T), s_x^*(T') \rangle = D_x \delta(T - T')$ for $x = w, \theta, f, t$,

$$\begin{aligned}
D_w &= 2w_0 D, \\
D_\theta &= 2D(1 + \pi^2/12) / (3w_0), \\
D_f &= 2D / (3w_0 \tau_0^2), \\
D_t &= \pi^2 \tau_0^2 D / (6w_0),
\end{aligned} \tag{5.37}$$

where D is defined in Eqs. (5.12) and (5.13).

The stochastic differential equations in Eq. (5.35) can be solved analytically.

The variances of $\Delta w(T)$, $\Delta f_c(T)$, and $\Delta t_c(T)$ become

$$\begin{aligned}
\sigma_w^2(T) &= \langle |\Delta w(T)|^2 \rangle = -D_w(1 - e^{2r_w T})/(2r_w) \xrightarrow{T \rightarrow \infty} -D_w/(2r_w), \\
\sigma_{f_c}^2(T) &= \langle |\Delta f_c(T)|^2 \rangle = -D_f(1 - e^{2r_f T})/(2r_f) \xrightarrow{T \rightarrow \infty} -D_f/(2r_f), \\
\sigma_{t_c}^2(T) &= \langle |\Delta t_c(T)|^2 \rangle = (r_t^2 D_f / r_f^2 + D_t)T + 2r_t^2 D_t(1 - e^{r_f T})/r_f^3 \\
&\quad - r_f^2 D_t(1 - e^{2r_f T})/(2r_f^3) \xrightarrow{T \rightarrow \infty} D_t T + (1/3)D_f r_f^2 T^3,
\end{aligned} \tag{5.38}$$

which indicates that the variances of energy and the frequency will remain constrained as $T \rightarrow \infty$, while the variance of the central time is unbounded. In experiments, the timing phase jitter is defined by the central time drift between two consecutive round trips [4], which we approximate as $\delta t_c = d\Delta t_c/dT$.

The Langevin equations that we introduced in Eq. (5.16) and the variances of the statistical quantities that we introduced in Eq. (5.19) effectively generalize Eqs. (5.35) and (5.38) to any modelocked pulse waveform and any governing equation that has the form of Eq. (5.5). The power spectral densities for Δw , Δf_c , and the phase jitter—which can be derived from the timing phase jitter δt_c —become [4, 9],

$$\begin{aligned}
S_w(f) &= \frac{D_w}{r_w^2 + (2\pi f)^2}, \\
S_{f_c}(f) &= \frac{D_f}{r_f^2 + (2\pi f)^2}, \\
S_\psi(f) &= \frac{S_{\delta t_c}(f)}{(T_R f)^2} = \frac{r_t^2 D_f}{(T_R f)^2 [r_f^2 + (2\pi f)^2]} + \frac{D_t}{(T_R f)^2}.
\end{aligned} \tag{5.39}$$

5.2.1.2 The Monte Carlo Simulation Method

For a given set of parameters, we carry out a large number of Monte Carlo simulation runs with independent noise realizations. In each simulation run, we solve the laser evolution equation, Eq. (1.1), using a variant of the split-step method [37]. We use the local error to adjust the propagation step sizes [50]. We use N_{mc} to denote the number of simulation runs, and we use N_R to denote the number of round trips in each run. For a given statistical quantity $\Delta x(T)$, we obtain a time series $\Delta x[k] = \Delta x(kT_R)$, $k = 1, 2, \dots, N_R$.

We finally evaluate the power spectrum of a given time series $\Delta x[k]$ using the discrete-time Fourier transform and the ensemble average over all the runs,

$$\bar{S}_h(f) = \frac{1}{N_{\text{mc}}N_R} \sum_{n=1}^{N_{\text{mc}}} |\text{DTFT} \{\Delta x[k]\}|^2, \quad (5.40)$$

where in this study we set $N_{\text{mc}} = 600$, and $N_R = 12000$.

5.2.1.3 The Dynamical Method

In Sec. 5.1, we have described the derivation and the implementation of the dynamical method.

5.2.2 Application to Modelocked Systems

We now compare the three different methods that we summarized in Sec. 5.2.1. In Secs. 5.1 and 5.2.1.1, we formulated the dynamical method and the Haus-Mecozzi method in terms of the normalized frequency. In order to plot the noise spectrum

in terms of the physical frequency f_{phys} , we substitute

$$f = f_{\text{phys}}T_R. \quad (5.41)$$

5.2.2.1 The Haus Modelocking Equation

We first perform a comparison of the computational efficiency of these three methods with the HME [9], given in Eqs. (1.1)–(5.4), and setting

$$D = g(|u_0|)h\nu_0T_R, \quad (5.42)$$

where h is Planck’s constant, and ν_0 is the central frequency of the optical field. The computations are carried out using Matlab® on a desktop workstation, Dell® Precision Tower 7910 which uses an Intel® Xeon(R) CPU E5-2630 v4 with 10 cores. The system memory is 16 GB. The operation system is Ubuntu 16.04 LTS. Matlab® uses about 500 MB when it is started without running any programs. We use the parameters from [4] and show them in Table 5.1.

We propagate the laser system for 15000 round trips and we observe that the statistical properties of the noise-related quantities—the pulse energy, the central frequency, and the rate of change of round trip time—appear stationary after 3000 round trips. The propagation of the variances of Δw , Δf_c , and Δt_c are shown in Fig. 5.1. The variances of Δw and Δf_c eventually reach an asymptote, while the variance of Δt_c grows indefinitely, which agrees with Eq. (5.38).

In Fig. 5.2 we show the power spectral densities that we obtain. All spectra are single-sided spectra [4]. In Fig. 5.2(a) we plot the energy noise as $10 \log_{10} [S_w(f)/w_0^2]$, the frequency noise as $10 \log_{10} [S_{f_c}(f)/\nu_0^2]$, and the phase noise as $10 \log_{10} [S_\psi(f)]$

Parameter	Value	Parameter	Value	Parameter	Value
T_R	10 ns	g_0	0.603	ω_g	20 T rad/s
γ	1/MW	ν_0	282 THz	l	0.0563
$P_{\text{sat}}T_R$	2 nJ	β''	-0.003 ps ²	δ	0.046/MW
w_0	20 nJ	A_0	$182.5 \sqrt{\text{W}}$	τ_0	0.3 ps

Table 5.1: The parameters we use to evaluate the noise levels. These parameters are the same as in [4].

which is consistent with Fig. 1 in [4]. For all three power spectral densities, the agreements of the three methods is excellent.

In Fig. 5.2, we plot the spectrum from 1 Hz to 10⁸ Hz. The Haus-Mecozzi method produces analytical predictions and thus can be used at any frequency resolution. The dynamical method can also be used at any frequency resolution. When evaluating the noise spectrum in the Monte Carlo method, we assign $N_{\text{mc}} = 600$ and $N_R = 12000$, which enables us to show the frequency range from about 8 kHz to 50 kHz. Any increase in the frequency resolution greatly increases the computational load when using the Monte Carlo method, which imposes a practical limit on the frequency resolution that can be obtained.

The time and memory cost performances of the Monte Carlo and dynamical methods are summarized in Table 5.2. We obtain a good agreement with the Haus-Mecozzi and dynamical methods when we use the Monte Carlo method with 600

Approach	# of cores	Time cost	Memory usage	Storage usage
A single run	1	7.8 s	535 MB	1.1 MB
600 runs	6	784 s	2.87 GB	245.8 MB
Dynamical	1	< 3 sec	967 MB	141.5 MB

Table 5.2: Comparison of the computational efficiency of the Monte Carlo and dynamical methods for evaluating the noise performance of the Haus modelocking equation. We integrate the system for 15000 round trips on each simulation run of the Monte Carlo method. The tests are coded in Matlab[®], which has a memory overhead of 500 MB that is included in the memory usage.

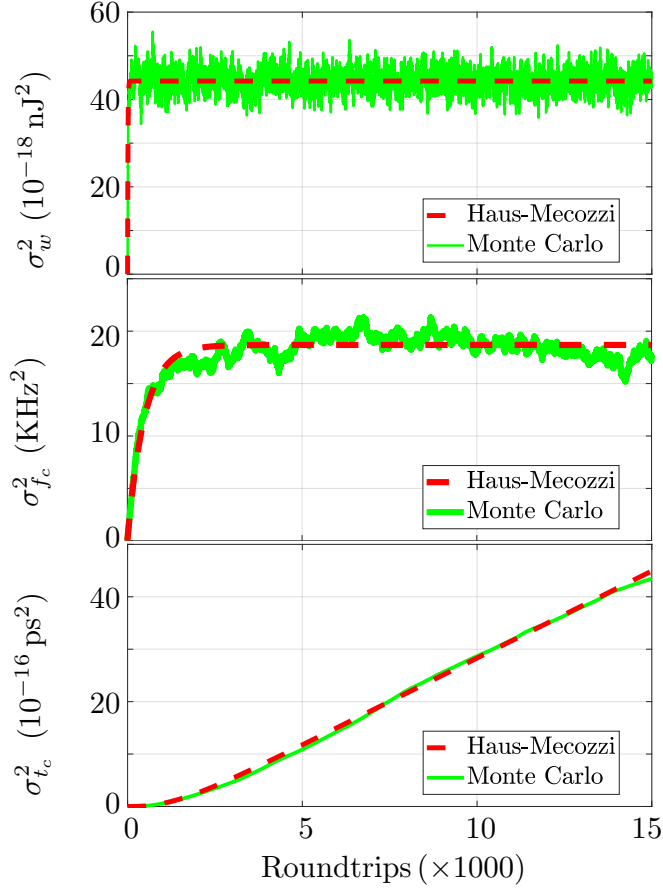


Figure 5.1: Comparison between the Haus-Mecozzi and Monte Carlo methods, where $\sigma_w^2(T)$, $\sigma_{f_c}^2(T)$, and $\sigma_{t_c}^2(T)$ are propagation-dependent variances of the pulse energy w , central frequency f_c , and the central time t_c . The Haus-Mecozzi method results are from Eq. (5.38).

simulation runs. The total CPU time cost is about $(784 \times 6 = 4704)$ sec, which is about 1 hour and 18 min. The memory usage per core $(2870/6 \approx 478)$ MB, which is less than that for a single run (535 MB) because the overhead of parallel computing is spread when more nodes are used. More memory might be required if a finer

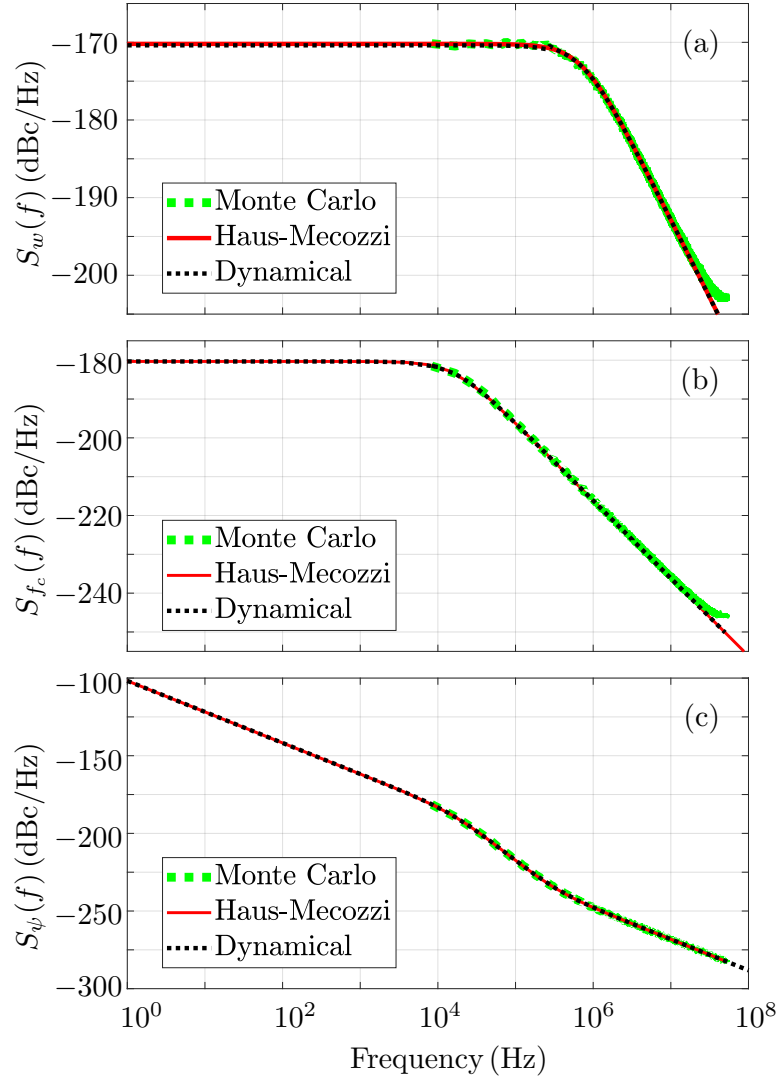


Figure 5.2: Noise spectra of (a) the energy jitter, (b) the frequency jitter, and (c) the timing phase jitter that we obtain from the Monte Carlo, Haus-Mecozzi, and dynamical methods. The agreement is excellent and the results in (c) agree with Fig. 1 in [4].

discretization of $u(t, T)$ in both t and T is needed. The storage usage is low (less than 1 GB) in the Monte Carlo simulations since we only save the pulse parameters, f_c , w , and t_c , instead of saving the pulse profile for each iteration.

The dynamical method has a far greater computational efficiency than does the Monte Carlo method. The dynamical method is able to cover a larger frequency range than does the Monte Carlo method in less than 3 sec of computational time. In the example shown here, we calculated 80 frequencies from 1 Hz to 80 Hz. The dynamical method uses more memory in a single core than does the Monte Carlo method, but the total memory use is still less than 1 GB.

5.2.2.2 The SESAM Laser

Next, we consider a case that has no known analytical solution. Here, we model a laser with a semiconductor saturable absorption mirror (SESAM), in which saturable absorber responds slowly compared to the time duration of the modelocked pulse [45] Typical time scales are picoseconds for the response time of the SESAM and 100–200 femtoseconds for the pulse duration, as we show in Table 5.3 [47]. The central wavelength of the output pulse is 1564 nm. The system can be described using Eqs. (1.1), (1.3), (4.1), (4.2) and (5.42), which we re-write as

$$\begin{aligned} \frac{\partial u}{\partial T} = & -i\phi u + t_s \frac{\partial u}{\partial t} + \frac{g}{2} \left(1 + \frac{1}{2\omega_g^2} \frac{\partial^2}{\partial t^2} \right) u - \frac{l}{2} u - i \frac{\beta''}{2} \frac{\partial^2 u}{\partial t^2} \\ & + i\gamma |u|^2 u - \frac{\rho}{2} nu + s(t, T), \end{aligned} \tag{5.43}$$

$$g(|u|) = g_0 / [1 + P_{av}(|u|) / P_{sat}],$$

$$\frac{\partial n}{\partial t} = \frac{1-n}{T_A} - \frac{|u(t, T)|^2}{w_A} n,$$

Parameter	Value	Parameter	Value	Parameter	Value
T_R	3.33 ns	w_A	157 pJ	P_{sat}	9.01 mW
g_0	7.74	ρ	0.0726	β''	-0.0144 ps ²
ω_g	30 ps ⁻¹	T_A	2.00 ps	γ	0.00111 W ⁻¹
l	1.05				
A_0	$25.2\sqrt{W}$	τ_0	143 fs	w_0	0.182 nJ

Table 5.3: The values of parameters we use in Eq. (5.43). The stationary pulse parameters A_0 , τ_0 , and w_0 are obtained computationally and thus are separated from the rest.

where $P_{\text{av}}(|u|) = \int_{-T_R/2}^{T_R/2} |u(t, T)|^2 dt / T_R$.

In Fig. 5.3, we show the evolution of the variances of Δw , Δf_c , and Δt_c . To compute the variances using the Haus-Mecozzi method, we use the stationary pulse parameters that we obtained computationally by propagating the evolution equations. The Haus-Mecozzi method makes an accurate prediction for the variances of the energy Δw and the frequency Δf_c . However, the Haus-Mecozzi method underestimates the variance of the central time Δt_c by a factor of 300, as shown in Fig. 5.3.

In Fig. 5.4, we show the power spectral densities of Δw , Δf_c , and Δt_c that we derived using these three methods. Both the Haus-Mecozzi method and the dynamical method yield good agreement for the background noise level with the

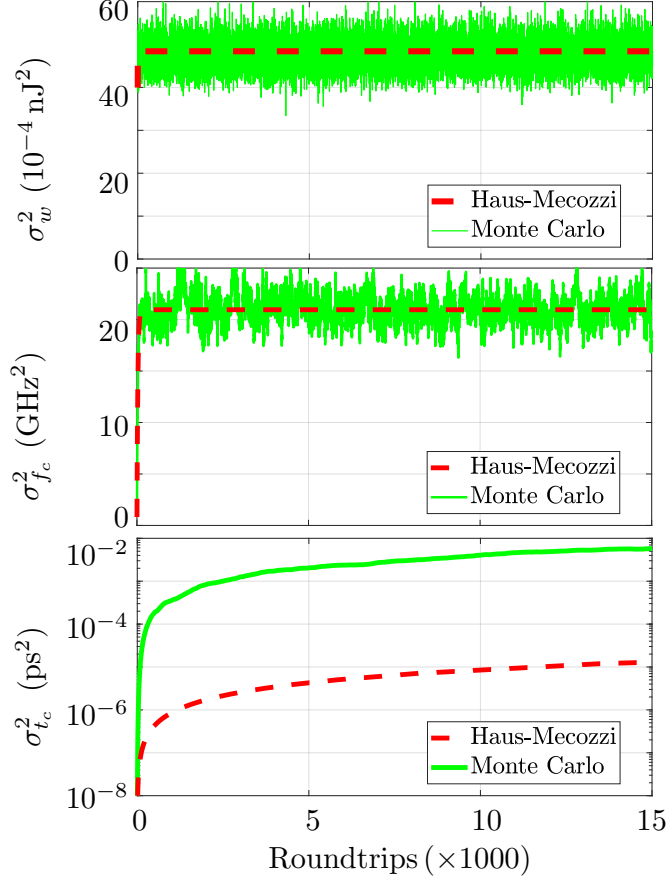


Figure 5.3: Comparison between the Haus-Mecozzi and Monte Carlo methods for the SESAM fiber laser, where $\sigma_w^2(T)$, $\sigma_{f_c}^2(T)$, and $\sigma_{t_c}^2(T)$ are propagation-dependent variances of the pulse energy Δw , central frequency Δf_c , and the central time Δt_c . We obtain the Haus-Mecozzi method results by substituting the computational stationary pulse solution parameter from Table 5.3 into Eq. (5.38).

Monte Carlo method. However, the Haus-Mecozzi method completely misses the sideband that is present in each of the power spectral densities. We have shown [58]

that the output power spectrum of the SESAM fiber laser features a sideband that is located between 15 MHz to 20 MHz as the pump power changes. In the Monte Carlo simulations, the sideband appears in all three power spectral densities, as shown in Fig. 5.4. The dynamical method is able to predict the height of the sidebands successfully. Hence, the dynamical method provides an accurate calculation of the noise levels for a wider group of modelocked lasers than does the Haus Mecozzi method.

We observe that the Monte Carlo method consistently overestimates the noise level at higher frequencies, which is due to aliasing. We have defined the output signals of the laser cavity as a continuous-time random process. However, in order to calculate the discrete-time Fourier transform, given in Eq. (5.40), the output signal of the laser is recorded once per round trip, which sets an upper limit equal to the Nyquist frequency, which equals $1/(2T_R) = 150$ MHz. Since our noise source is wide-band, noise with frequencies higher than 150 MHz will leak into our evaluation band and cause the evaluated noise level to raise. The Monte Carlo results will converge to the noise level that is obtained using the dynamical method when we record more times during one round trip, which increases the memory and post-processing load.

We again carry out a computational efficiency test, and we show the results in Table 5.4. Here, the Monte Carlo experiments are carried out using Matlab® and 512 cores on a cluster [59]. The CPUs are all quad-core Intel Nehalem X5560 processors (2.8 GHz, 8 MB cache) with 3 GB per core on average. All nodes are running Red Hat Enterprise Linux 6.4. We propagate the pulse for 15000 rountrips, and we only save the data for the pulse parameters instead of the entire pulse.

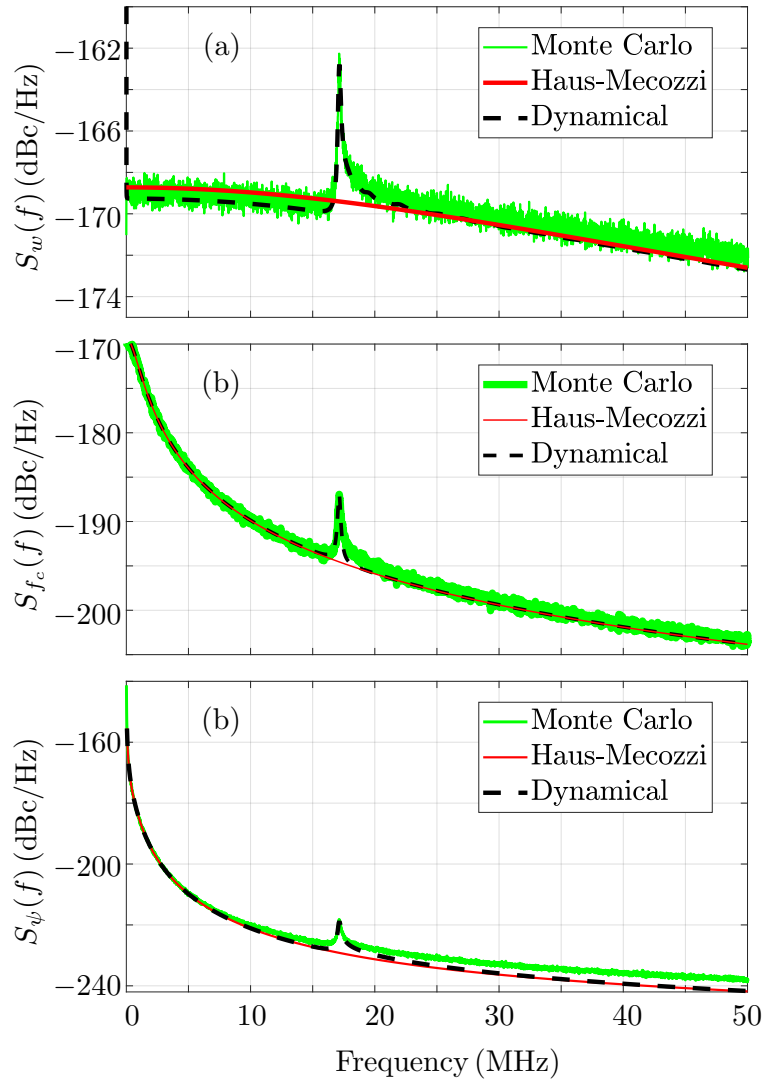


Figure 5.4: The power spectral density of (a) the energy jitter, (b) the frequency jitter, and (c) the timing phase jitter that we obtain from the Monte Carlo, Haus-Mecozzi, and dynamical methods.

The entire computation requires about 20 min and uses 256 computing cores. Each simulation takes more than 300 MB on each computing core, and we saved 1.7 MB

Approach	# of cores	Time cost	Memory usage	Storage usage
256 runs	256	20 min	314 MB/process	1.7 MB/process
Dynamical	1	< 4 min	900 MB	144 MB

Table 5.4: Comparison of the computational efficiency of the Monte Carlo and dynamical methods for evaluating the noise performance of the SESAM modelocking model. We integrate the system for 2×10^5 round trips in each simulation run of the Monte Carlo method.

of data on the hard drive.

By comparison, the dynamical method is carried out on the same desk workstation as in Sec. 5.2.2.1: a Dell® Precision Tower 7910 that uses an Intel® Xeon(R) CPU E5-2630 v4 and has 10 cores. The combined computational cost of solving for the stationary solution and obtaining the power spectral density is less than 4 min, and the computation uses very reasonable memory and storage. Again, the improvement in the computing efficiency is large. Compared to the Monte Carlo simulation method, the dynamical method requires only 1/1280 of the CPU time, 1/90 of the memory, and 1/3 of the storage space.

5.3 Conclusions

Over the last three decades, short-pulse lasers—and more particularly passively modelocked lasers—have been the subject of continued experimental interest. Robust and low-noise passively modelocked lasers are key components in frequency combs. As passively modelocked lasers have become more complex, the Haus-Mecozzi method has become increasingly inadequate to analyze the noise performance of these lasers. As one example, we studied a SESAM fiber laser and showed that this method greatly underestimates the timing phase noise. By contrast, Monte Carlo simulations can yield accurate results, and this method is intuitive and easy to implement. However, it requires large computing resources, which makes its use for parameter optimization difficult.

Based on dynamical systems theory, we have developed a dynamical methods theory that is able to calculate the noise impact accurately and rapidly. As we have shown in our examples, it is as accurate as Monte Carlo simulations, and is about three orders of magnitude faster computationally, while requiring less memory and storage. Therefore, this dynamical method is a powerful tool that can play a useful role in optimizing the design of short-pulse lasers.

As an example, the Matlab® code that calculates the power spectral density of the timing phase jitter, shown in Fig. 5.4(c), is available at [<http://photonics.umbc.edu/software.html>].

CHAPTER 6

Laser Cavity Design Optimization

As we stated in the Introduction, key goals when modeling a passively mode-locked laser are to find a region in the laser's adjustable parameter space where the laser can operate stably and then to produce an output pulse with an optimal profile. For the SESAM fiber laser that we model [23, 47], our goal is to optimize the cavity design to achieve higher output power, larger bandwidth, and lower sidebands than in the experiments. In this chapter, we carry out parameter studies using the root-finding method and the dynamical method that we developed in previous chapters.

In Chapter 4, we showed that the wake mode instability can occur when the response time of a saturable absorber is longer than the output pulse duration and when the unsaturated gain, g_0 , becomes sufficiently large or the group delay dispersion, β'' , becomes sufficiently close to zero [45, 47]. In Fig. 4.5, we showed the region of stable operation in the parameter space of (g_0, β'') . In this chapter, we further quantify how the output power and power spectral density (PSD) of the SESAM laser is limited by the wake mode instability. We also showed in Chapter 5 that the

wake modes are primarily responsible for the experimentally-observed sidebands in the PSD for both energy and phase. In this chapter, we further quantify how the output power and power spectral density (PSD) of the SESAM laser is limited by the wake mode instability and quantify the energy PSD due to the wake modes.

In Fig. 4.5, we showed that the wake mode instability occurs when the unsaturated gain becomes sufficiently large. Thus, this limit on the unsaturated gain increases when the cavity loss increases, which happens, for example, when the output coupling ratio increases. Here, we show in detail how this stability limit, the output power, and the noise are affected by increasing the output coupling ratio. We finally show that this modification can lead to smaller wall-plug powers and better power efficiency.

6.1 Optimizing the Laser Cavity

The lumped model that we describe in chapter 3 accurately captures the behavior of each cavity component and thus provides a good reference for checking specific parameters in our optimization study. However, the computational results for wake mode sidebands in the RF spectrum that we have shown in Fig. 3.7 requires a computation time for each set of parameters that is about 2 hours on a desktop computer. By comparison, the dynamical method that we developed to evaluate the noise level of a modelocked laser—an averaged model in which we average the action of the components over one round trip in the laser—takes only minutes on a desktop computer [11, 80]. A more detailed discussion of a lumped model and an

averaged model can be found in [11]. Using the averaged model that we describe in Chapter 4, we earlier found and showed in Fig. 4.5 the region of stable operation as the unsaturated gain g_0 and the group delay dispersion β'' vary [47], which we show again in Fig. 6.1.

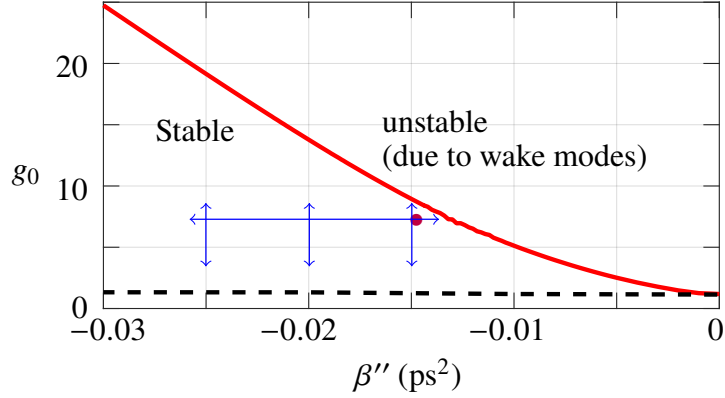


Figure 6.1: When the output coupling ratio $t_{oc} = 9\%$, the stability boundaries in the parameter space of the unsaturated gain g_0 and the group delay dispersion β'' . The purple dot indicates the cases $g_0 = 7.74$ and $\beta'' = -0.0144 \text{ ps}^2$ which corresponds to the experimental pulse as $P_{\text{pump}} = 237 \text{ mW}$. In Sec. 6.1.1, we perform parameter studies along the directions as indicated by the blue arrows.

In Chapter 5, we have demonstrated that this procedure is orders of magnitudes faster computationally than techniques that solve the evolution equations [80]. In this section, we use the results of our parameter study to optimize the comb parameters. Our goal is to increase the average output power, P_{out} , which equals the

output pulse energy divided by the round-trip time

$$P_{\text{out}} = \frac{t_{\text{oc}}}{T_R} \int_{-T_R/2}^{T_R/2} |u_0(t)|^2 dt, \quad (6.1)$$

while not significantly narrowing the comb bandwidth, i.e., broadening the pulse duration. We first use the stable output pulse that we obtained using the averaged model in [47] as the reference pulse, for which the output coupling ratio $t_{\text{oc}} = 9\%$, $g_0 = 7.74$, and $\beta'' = -0.0144 \text{ ps}^2$, as indicated by the purple dot in Fig. 6.1. This pulse has an average output power of 4.9 mW and a FWHM duration of 260 fs. In Sec. 6.1.1, we will show how the pulse profiles and noise level change as we change g_0 and β'' , as indicated by the blue arrows in Fig. 6.1.

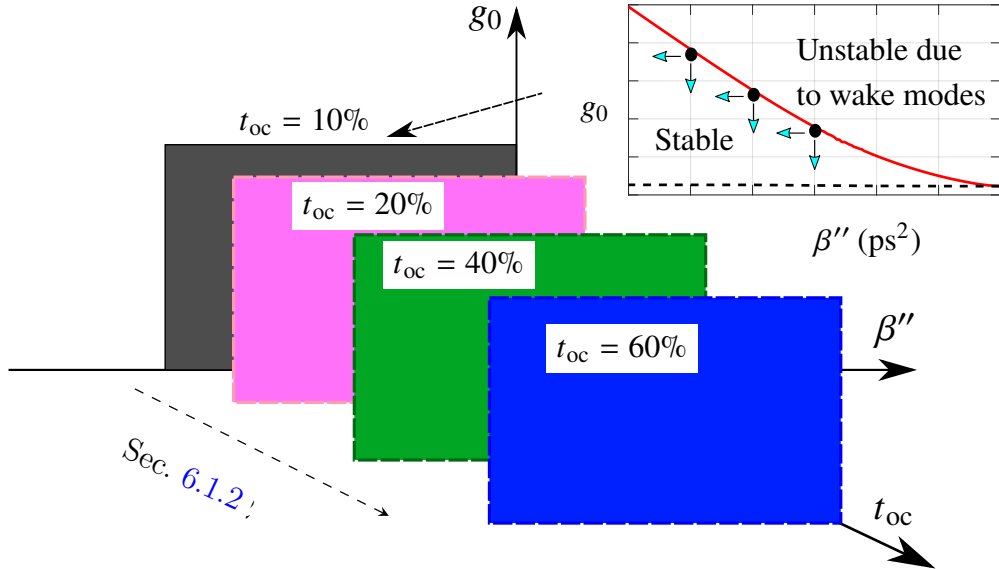


Figure 6.2: An illustration of the parameter space and an example of the search directions that we used to perform the optimization study in Sec. 6.1.2.

In [81], we showed that the average output power can be increased by increasing the pump power and the output coupling ratio, t_{oc} . Here, in Sec. 6.1.2, we adapt this technique for use with the averaged model in order to obtain a more energetic, shorter, and less noisy pulse solution. We show an illustration of the parameter space in Fig. 6.2. We choose four different values of t_{oc} (10%, 20%, 40%, and 60%) and calculate the variation of profiles and the PSD of the stable pulse. The smallest value of t_{oc} is close to the experimental value of 9%. For a given value of t_{oc} , we will vary either g_0 or β'' and compare the pulse energy, duration, and the PSD.

6.1.1 When $t_{oc} = 9\%$

We first show how the pulse profiles and the PSD of the energy fluctuations, $S_w(f)$, change for a given output coupling ratio; $t_{oc} = 9\%$, for example, we perform parameter studies along the directions as indicated by the blue arrows that we show in Fig. 6.1.

6.1.1.1 Variation of Pulse Profiles When g_0 Changes

In Fig. 6.3, we show the variation of the pulse profiles, in which w_0 is the intra-cavity pulse energy and τ_p is the full-width-half-maximum (FWHM) pulse duration. We vary the unsaturated gain with three different values of β'' , -0.015 ps^2 , -0.020 ps^2 , and -0.025 ps^2 . When $g_0 \geq 9.0$ and $\beta'' > -0.015 \text{ ps}^2$, the laser becomes unstable due to the wake modes. When $\beta'' < -0.015$, the laser remains stable for some values of $g_0 > 9.0$, as we will show in the next section. For given values of β'' ,

the pulse energy w_0 increases linearly in Fig. 6.3, and the pulse duration τ_p decreases as the unsaturated gain g_0 increases. We also observe that the pulse energy w_0 stays almost unchanged when β'' varies, while the FWHM pulse duration τ_p increases by a factor of 1.6 as β'' changes from -0.015 ps^2 to -0.025 ps^2 .

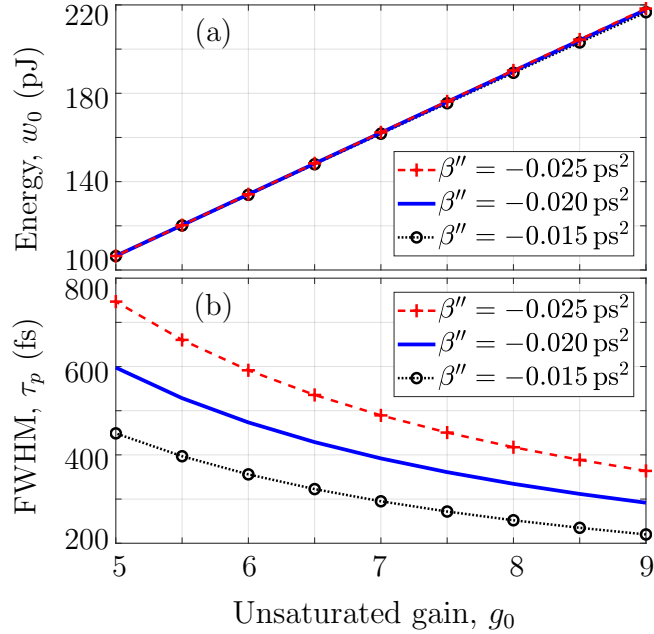


Figure 6.3: (a) The intra-cavity pulse energy w_0 and (b) the FWHM pulse duration τ_p as a function of the unsaturated gain g_0 , for three values of group delay dispersion β'' .

The wake modes can induce sidebands that are visible in the energy PSD as we show in Fig. 3.7. In Fig. 6.4, we show the PSD $S_w(f)$ as a function of g_0 that we computed using the dynamical method [11]. Here, we plot the PSD in dBc/Hz,

$$S_w(f) \text{ [dBc/Hz]} = 10 \log \frac{S_w(f)}{w_0 f_{\text{FSR}}}, \quad (6.2)$$

where the repetition frequency $f_{\text{FSR}} = 1/T_R = 300 \text{ MHz}$.

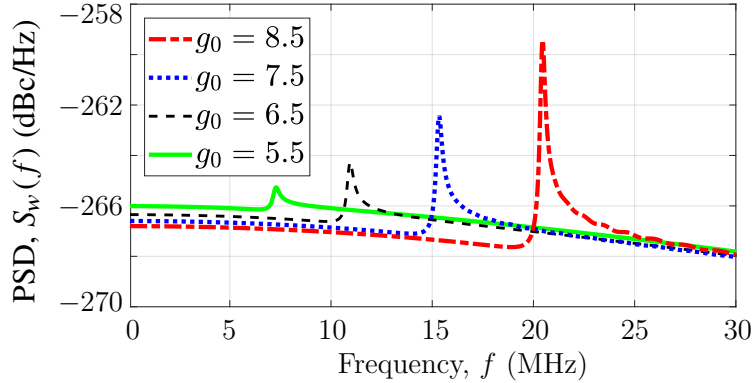


Figure 6.4: Variation of the wake mode sidebands when the unsaturated gain g_0 increases with $\beta'' = -0.015 \text{ ps}^2$.

In Fig. 6.4, we show the energy PSD $S_w(f)$ when the unsaturated gain g_0 increases for a fixed value of the group delay dispersion, $\beta'' = -0.015$. The wake modes become unstable when $g_0 \geq 9.0$. As g_0 increases from 5.5 and approaches the stability limit, the frequency offset of the sideband increases from about 7.5 MHz to 20.5 MHz, and the peak magnitude of the sideband grows from nearly zero to about 9 dBc/Hz above the background noise. The sideband profile is non-Lorentzian, which is consistent with the RF sideband spectra that we show in Fig. 3.7. This asymmetry occurs because both the discrete and the continuous modes in the dynamical system contribute to the PSD [80].

6.1.1.2 Variation of Pulse Profiles When β'' Changes

In Fig. 6.5, we show how the pulse profiles change as β'' changes when $g_0 = 7.74$. We observe that the pulse energy is almost constant at 180 pJ, which corre-

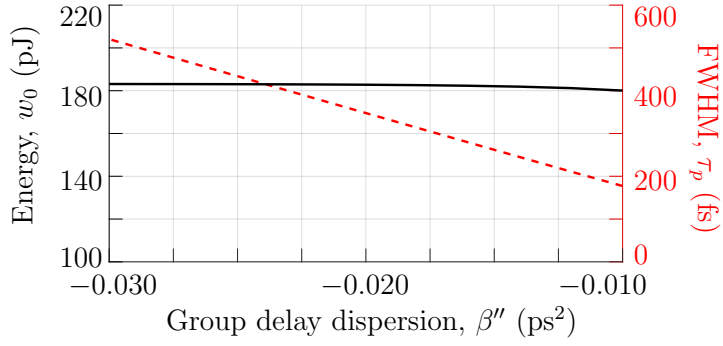


Figure 6.5: The intra-cavity pulse energy w_0 and the FWHM pulse duration τ_p as a function of the group delay dispersion β'' with $g_0 = 7.74$.

sponds to an average output power of about 4.9 mW. The FWHM pulse duration increases almost linearly—from about 510 ps to about 180 ps—as β'' changes from -0.010 ps^2 to -0.030 ps^2 . Hence, by tuning the group delay dispersion close to zero, we can obtain pulses with broader bandwidth.

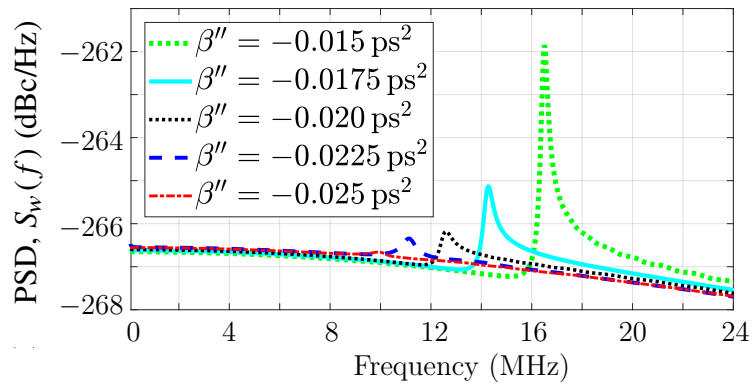


Figure 6.6: Variation of the wake mode sidebands when the group delay dispersion increases with $g_0 = 7.74$.

In Fig. 6.6, we show the PSD of the energy fluctuations when β'' changes and g_0 is constant. As β'' becomes less negative; increasing from $\beta'' = -0.025 \text{ ps}^2$ to $\beta'' = -0.015 \text{ ps}^2$, we observe that the frequency offset of the sideband increases from about 10.0 MHz to 16.5 MHz, and the peak magnitude of the sideband increases from zero to about 5 dBc/Hz above the background.

From the results in Figs. 6.4 and 6.6, we conclude that we can obtain a high-power comb output by either increasing the system gain or making group delay dispersion more negative, but at the cost of narrowing the bandwidth and increasing the wake mode sidebands. We also conclude that it is preferable to suppress the sidebands by making the group delay dispersion more negative rather than by decreasing the pump power. With this choice, the pulse duration increases, but the pulse energy remains almost unchanged as shown in Fig. 6.5.

6.1.2 When t_{oc} Changes

The SESAM fiber laser utilizes a piece of erbium-doped fiber (EDF) as the gain medium. In experiments, the unsaturated gain g_0 can be increased by increasing the pump power of the EDF, the doping concentration, or the geometry and the length of the EDF [51]. We assume that the length of the EDF is unchanged, and thus the roundtrip time T_R —and the repetition frequency f_{FSR} (300 MHz)—is unchanged.

6.1.2.1 Adjusting the Unsaturated Gain

In Fig. 6.7, we show how the output pulse's average power and duration change with respect to the unsaturated gain g_0 for given values of group-delay dispersion β'' . We focus on cases when g_0 increases and the system approaches the onset of wake mode instability, which we mark using black dots in Fig. 6.7. We use solid lines to denote the variation of the average output power P_{out} and dashed lines to denote the variation of the FWHM output pulse duration τ_p . As indicated in Fig. 6.2, we set the output coupling ratio t_{oc} as (a) 10%, (b) 20%, (c) 40%, and (d) 60%.

In each sub-figure of Fig. 6.7, we observe the wake mode instability occurs as g_0 increases with fixed values of β'' . The instability limit on g_0 increases as β'' increases. This result is consistent with the stability region that we have shown in [47]. In addition, we also observe that the instability limit for g_0 is further increased when the output coupling ratio t_{oc} increases. For example, for the case $\beta'' = -0.015 \text{ ps}^2$, the largest value of g_0 for stable operation is $g_0 = 8.5$ when $t_{\text{oc}} = 9\%$, as shown in Fig. 6.1. By comparison, when $t_{\text{oc}} = 20\%$, this limit becomes $g_0 = 11.0$ as shown in Fig. 6.7(b).

In the parameter regimes that we show in Fig. 6.7, the average output power P_{out} increases approximately linearly, while the FWHM pulse duration decreases with the growth of the unsaturated gain g_0 . The shortest pulse that we obtained is 153 fs with an average output power of 31 mW, which occurs when $t_{\text{oc}} = 20\%$, $\beta'' = -0.025 \text{ ps}^2$, and $g_0 = 22.5$.

When $t_{\text{oc}} = 9\%$, we showed in Fig. 6.4 that the magnitude of the wake modes

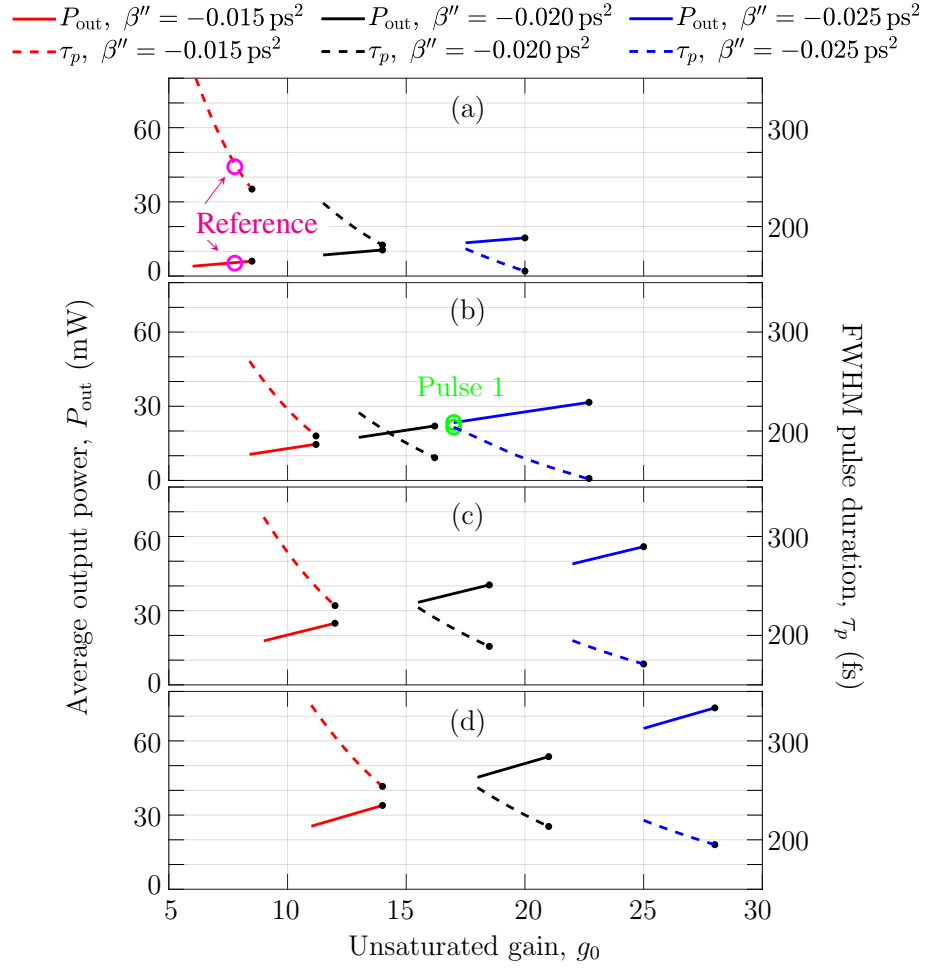


Figure 6.7: The output pulse profiles when the unsaturated gain g_0 varies for given values of the group delay dispersion β'' and the output coupling ratio t_{oc} . We set the output coupling ratio t_{oc} equal to (a) 10%, (b) 20%, (c) 40%, and (d) 60%. The black dots indicate the onset of the wake mode instability. The magenta and the green circles correspond respectively to the reference pulse and Pulse 1, which we show in Fig. 6.9.

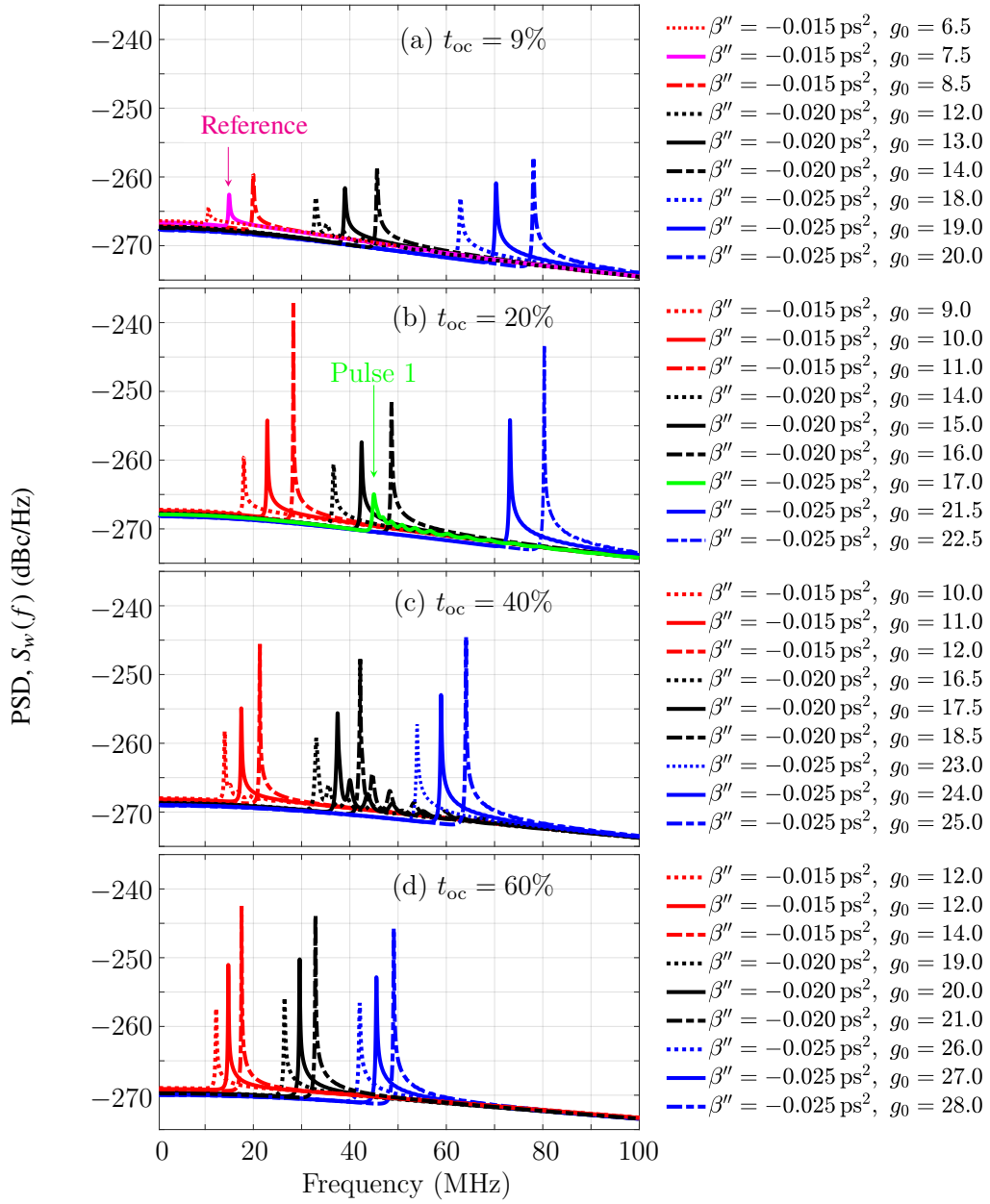


Figure 6.8: The energy PSD when g_0 , β'' , and t_{oc} vary. The green line in (b) shows the energy PSD that corresponds to Pulse 1, shown in Fig. 6.9.

grows when g_0 approaches the onset of wake mode instability. A similar behavior appears at other values of t_{oc} , as we show in Fig. 6.8. We select three values of g_0 for each case of (β'', t_{oc}) that we show in Fig. 6.7. We observe that both the magnitude and the offset frequency of the sidebands grow as g_0 increases. When $t_{oc} = 20\%$, we obtain the output pulse with the shortest duration, but it also has the highest wake mode sidebands.

It is possible to suppress the wake mode sidebands by decreasing the value of g_0 , which corresponds to decreasing the pump power in experiments. In our simulations, the peak of the sidebands decrease to below 5 dBc/Hz above the background noise when $g_0 = 17.0$, $t_{oc} = 20\%$, and $\beta'' = -0.025 \text{ ps}^2$, as shown in Fig. 6.7(b) in green. We call this output “Pulse 1,” and its profile is shown in Fig. 6.9.

In Fig. 6.9, we show a comparison of the magnitudes of Pulse 1, Pulse 2, which we will introduce in Sec. 6.1.2.2, and the reference pulse. Pulse 1 has an average output power of 23.4 mW and a FWHM pulse duration of 203.9 fs. This is about 22% shorter and three times more energetic than the reference pulse, and its maximum PSD is about -265 dBc/Hz , which is about 3 dBc/Hz lower than the reference pulse, as shown in Fig. 6.8(a) and (b).

6.1.2.2 Adjusting the Group Delay Dispersion

We have shown that, for a given value of group delay dispersion, we can obtain an output comb that is more powerful and has smaller sidebands than the reference pulse by adjusting the output coupling ratio and the unsaturated gain. We have

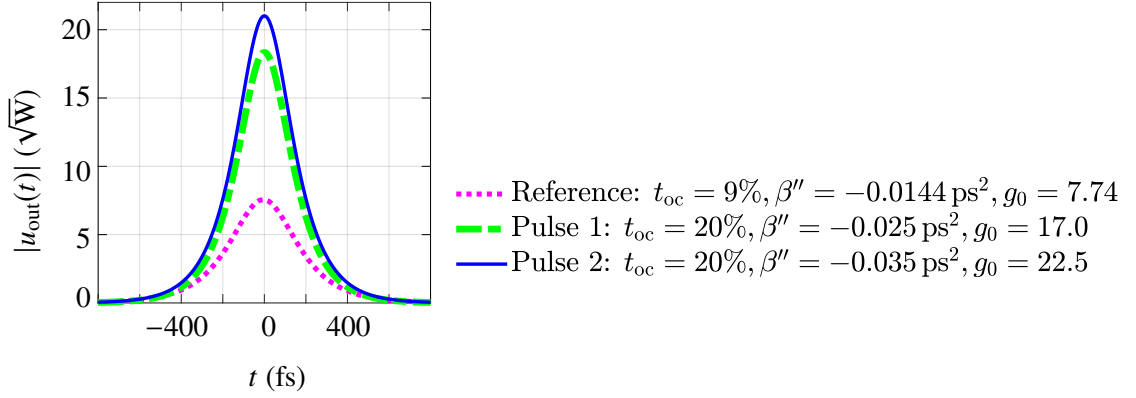


Figure 6.9: The optimal pulse profiles that we find using the averaged model.

shown in Fig. 6.5 that the pulse energy stays almost unchanged when only the group delay dispersion varies. Thus, we can apply this approach to obtain even more energetic output pulses.

In Fig. 6.10, we show that the average output power and output pulse duration change as a function of the group-delay dispersion β'' for different values of the unsaturated gain g_0 . For any given (t_{oc}, g_0) , we find that the average output power remains almost unchanged while the FWHM pulse duration decreases linearly when the group delay dispersion increases (decreases in magnitude). These results are consistent with the results in Fig. 6.5. We see again that among the cases that we investigated, the shortest pulse (153 fs) appears when $t_{oc} = 20\%$, $g_0 = 22.5$, and $\beta'' = -0.025 \text{ ps}^2$, as shown in Fig. 6.10(b).

In Fig. 6.11, we show the variation of the energy PSD. For any given parameter pair (t_{oc}, g_0) , we observe that the magnitude of the wake mode sidebands decreases

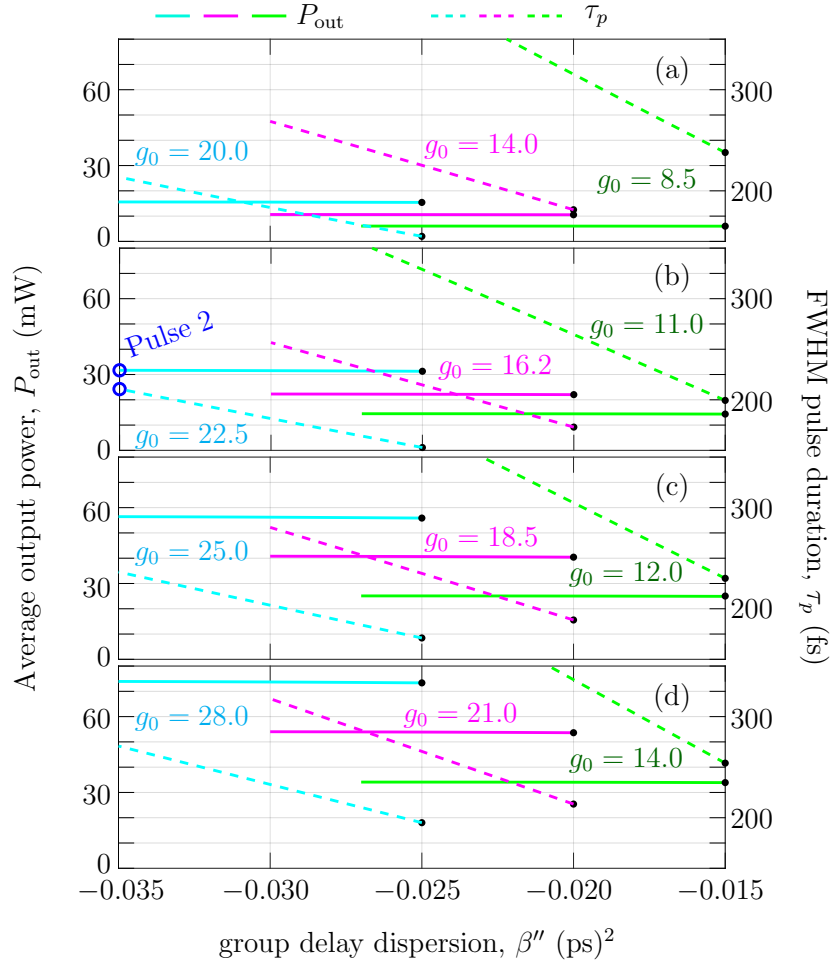


Figure 6.10: Variation of the stable output pulse profile when the group delay dispersion β'' , approaches zero for given values of unsaturated gain g_0 and output coupling ratio t_{oc} : (a) $t_{oc} = 10\%$, (b) $t_{oc} = 20\%$, (c) $t_{oc} = 40\%$, and (d) $t_{oc} = 60\%$. The black dots indicate the onset of the wake mode instability. The blue circles correspond to Pulse 2, shown in Fig. 6.9.

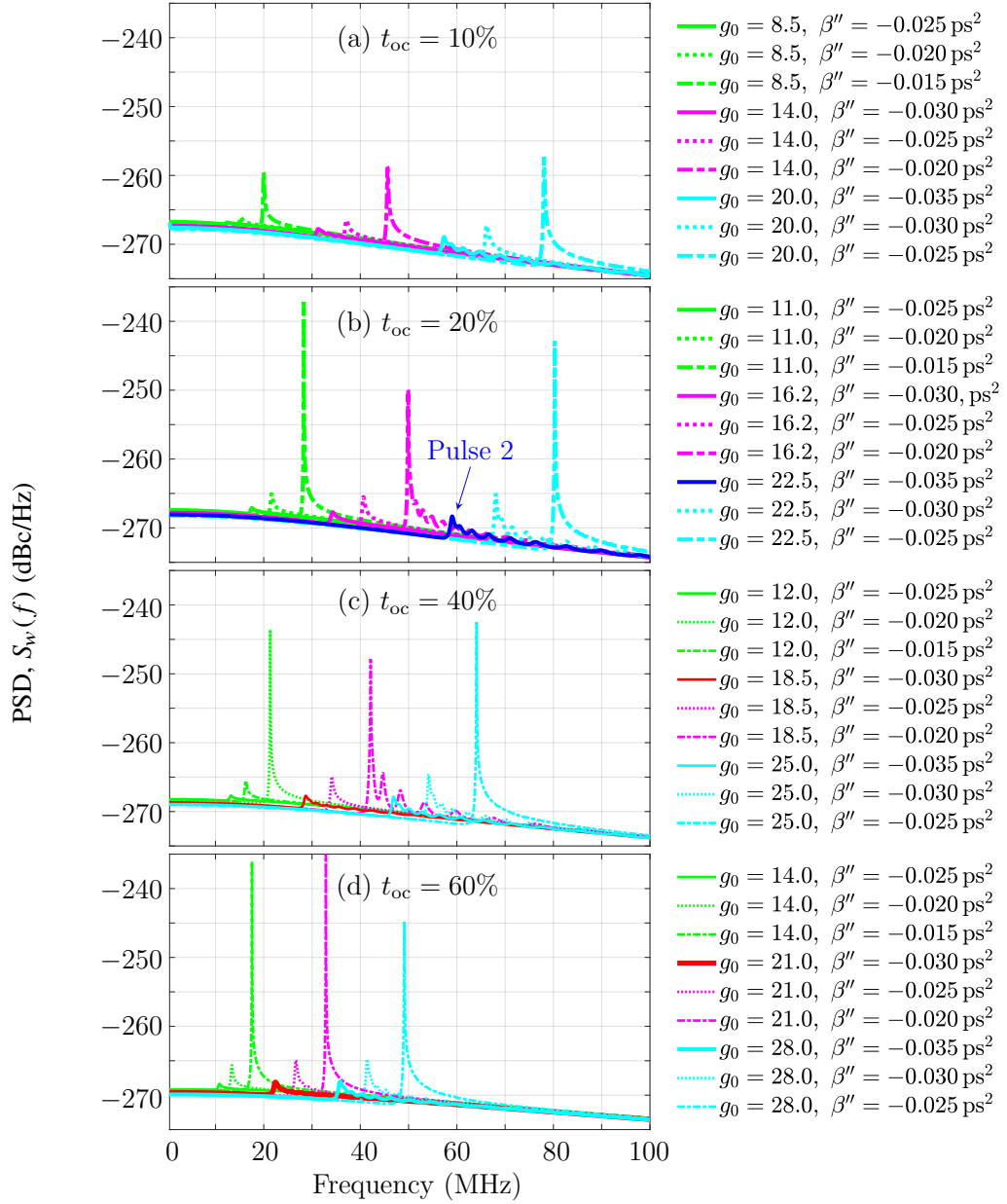


Figure 6.11: Variation of the wake mode sidebands when the output coupling ratio t_{out} changes. The blue line in (b) shows the energy jitter profile corresponding to Pulse 2, shown in Fig. 6.9.

significantly and can even vanish when the dispersion decreases by 0.010 ps^2 . For the case when $t_{oc} = 20\%$ and $g_0 = 22.5$, which we mark using blue circles in Fig. 6.11(b), we observe that the sideband’s magnitude is less than 5 dBc/Hz above the background when $\beta'' = -0.035 \text{ ps}^2$. More importantly, the FWHM pulse duration is 211 fs , which is about 20% shorter than the reference pulse (260 fs), while the average output power is still 31.7 mW , which is about five times more energetic than the reference pulse. This pulse, referred to here as “Pulse 2” is even more energetic than Pulse 1. We show a comparison of Pulse 1, Pulse 2, and the reference pulse in Fig. 6.9.

6.2 Validating the Optimization Study

We now return to the lumped model to validate the predictions of the averaged model for the optimized system parameters and more accurately calculate the predicted pulse profiles.

Our results in Sec. 6.1 show that by increasing the output coupling ratio t_{oc} , we can obtain output combs with a larger average output power and bandwidth than in the reported experiments. However, our results are based on two assumptions: (1) the length of the gain fiber—and thus the roundtrip time—remains unchanged, and (2) the unsaturated gain increases linearly with the pump power. These assumption are not necessarily valid in experimental systems. When the erbium-doped fiber is well-saturated, the unsaturated gain cannot increase indefinitely. Thus, in the SESAM laser cavity, the erbium fiber is not able to provide sufficient gain due to its

limited length. In order to obtain a larger cavity gain without changing the round trip time, we increase the doping concentration in the EDF by 50%.

In Fig. 6.12, we show the pulse profiles and their RF spectrum using the lumped model that we described in Chapter 3. Based on the variation of the pulse profiles with β'' as shown in Fig. 6.9, we calculate the pulse profiles using two more negative values of group velocity dispersion, $\beta_2 = -0.0534 \text{ ps}^2/\text{m}$ and $\beta_2 = -0.0730 \text{ ps}^2/\text{m}$.

In Fig. 6.12(a), we show the calculated pulse profiles. We have described the case when $t_{oc} = 9\%$ and $\beta_2 = -0.300 \text{ ps}^2/\text{m}$ in Fig. 3.4, in which the average output power is 4.8 mW, the intracavity pulse energy is 186 pJ, and the FWHM duration is 311 fs. When we set $t_{oc} = 20\%$ and $\beta_2 = 0.534 \text{ ps}^2/\text{m}$, we can obtain an average output power of 18.9 mW, which corresponds to an intracavity pulse with an energy of $w_0 = 518.5 \text{ nJ}$ and a FWHM duration of 321 fs. This output pulse profile has four times the energy of the current experimental output pulse and has a similar pulse duration. This result is consistent with the prediction using the averaged model for Pulse 1 in Fig. 6.9.

By comparison, when we set $t_{oc} = 20\%$ and $\beta_2 = -0.730 \text{ ps}^2/\text{m}$, we can obtain an average output power of 28.9 mW, which features an intra-cavity pulse of $w_0 = 617.8 \text{ nJ}$ and a FWHM duration of 286 fs. This output pulse profile is about 5 times more energetic than the current experimental output pulse, and has a pulse duration that is about 10% shorter. This result is consistent with the prediction for Pulse 2 in Fig. 6.9.

In Fig. 6.12(b), we show the calculated RF spectra that correspond to the

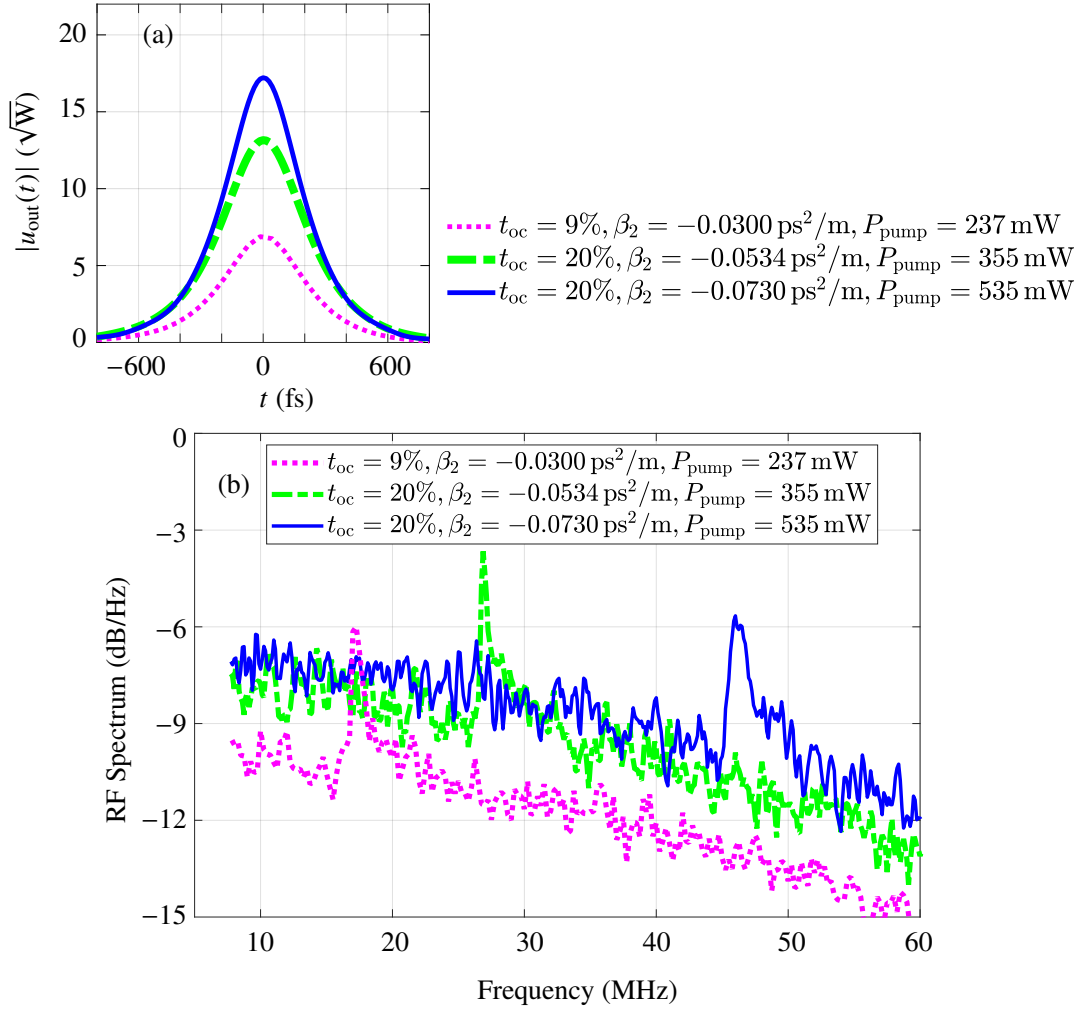


Figure 6.12: (a) The calculated optimal pulses and (b) their RF spectra using the lumped model. The reference pulse and its RF spectrum are consistent with our results in Sec. 6.1. In order to provide sufficient cavity gain, we set the doping concentration N_e of the erbium fiber equal to $5.21 \times 10^{25} \text{ cm}^{-3}$ when $\beta_2 = -0.0534 \text{ ps}^2$ and $\beta_2 = -0.0730 \text{ ps}^2$.

optimal pulse profiles, and we also show the experimental pulse spectra for comparison. Compared to the experimental setup, the output coupling ratio is increased from 9% to 20%, which leads to an increase in the system loss. The increased system gain causes the ASE noise level to rise, which raises the background noise level, as shown in Fig. 6.12(b). In all three cases that we consider, the wake mode sidebands remain about 4 dB above the background noise level, which is similar to the current experimental observation. In addition, the frequency offset increases when β_2 increases, which is consistent with the prediction using the averaged model that is shown in Fig. 6.11. However, there is a difference in the frequency offset of about 15 MHz between the averaged model and the lumped model. This difference is due to the inaccurate approximation of the gain profile in the averaged model, which is significantly simpler than the gain spectrum of erbium fibers [51].

6.3 Increasing the Power Efficiency

We use here the lumped model that we have described in Chapter 3, which is closely related to the experimental parameters. We carry out a computational study to optimize the power efficiency while maintaining a high average output power. The parameters we vary include the pump power P_{pump} , the length of the erbium-doped fiber L_{EDF} , and the output coupling ratio t_{oc} . The doping level N_e is set as the experimental value as given in Table 3.1. We find that, compared to current experimental parameters, a higher level of the output coupling ratio and a longer gain fiber length will improve the power efficiency and the average output

power. We define the power efficiency as

$$\eta_{\text{out}} = P_{\text{out}}/P_{\text{pump}}. \quad (6.3)$$

Again, our simulation is based on the configuration of the soliton comb laser that is illustrated in Fig. 4.2.

In Fig. 6.13, we show the results of our optimization study. As shown in Figs. 2(a) and (b), we set $L_{\text{EDF}} = 15.0$ cm and $t_{\text{oc}} = 15\%$ which are consistent with experiments. When the pump power increases from 60 mW to 120 mW, we find that P_{out} increases from about 1.76 mW to 3.80 mW, while η_{out} only improved slightly from 2.94% to 3.17%. This level of power efficiency is similar to experimental results. By comparison, we find that both P_{out} and η_{out} increase when we increase the output coupling ratio, as shown in Figs. 2(a) and (b). For example, when $P_{\text{pump}} = 100$ mW and t_{oc} increases to 50%, then the average output power increases to 6.33 mW. The power efficiency is double what is obtained when $t_{\text{oc}} = 15\%$.

Increasing t_{oc} yields similar improvements of average output power and efficiency when $L_{\text{EDF}} = 25.0$ cm and 32.5 cm for pump power at which stable output pulses can be obtained. However, there is a limit on the pump power in each case, which corresponds to an instability threshold. The instability is due to the wake modes when the stationary pulse duration τ_p is much shorter than the SESAM recovery time T_A [45, 47], i.e., $\tau_p/T_A \ll 1$, or to continuous wave breakthrough when $\tau_p/T_A \simeq 1$ [10]. When we increase the length of the erbium-doped fiber from 15.0 cm to 25.0 cm and then to 32.5 cm, the gain increases, which indicates that the absorption of the pump light is not complete when $L_{\text{EDF}} < 25.0$ cm. The under-utilization

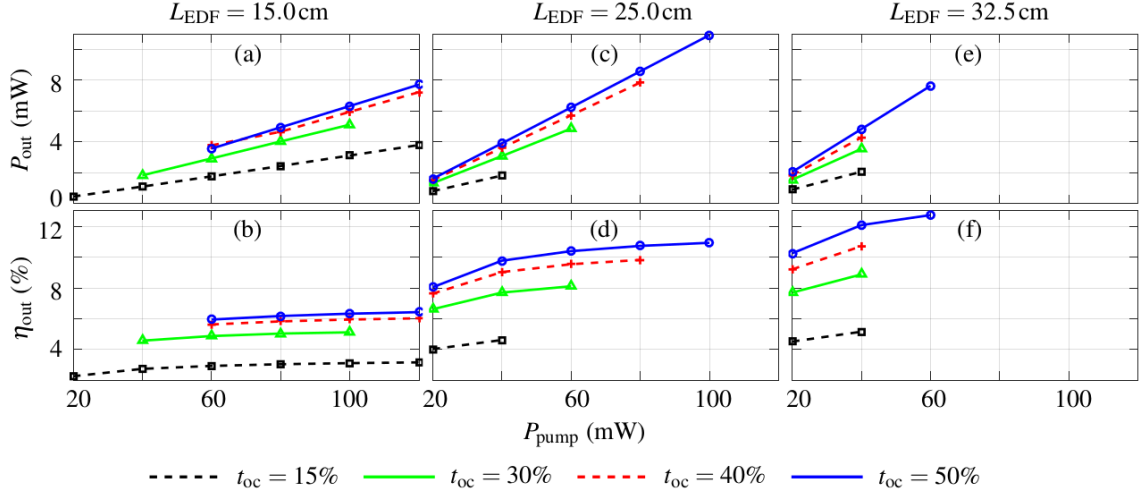


Figure 6.13: The calculated average output power P_{out} and power efficiency η_{out} with different levels of pump power P_{pump} and output coupling ratios t_{oc} , where the lengths of erbium-doped fiber $L_{\text{EDF}} = 15.0 \text{ cm}$ in (a) and (b), $L_{\text{EDF}} = 25.0 \text{ cm}$ in (c) and (d), and $L_{\text{EDF}} = 32.5 \text{ cm}$ in (e) and (f).

of the pump signal is also confirmed in experiments in which the pump signal is detected at the output coupler. Hence, one can obtain a similar level of gain by using a longer piece of erbium-doped fiber while decreasing the pump power, which leads to improved of power efficiency.

In Figs. 6.13(c) and (d), we also observe that when $t_{\text{oc}} = 15\%$ and when $P_{\text{pump}} > 40 \text{ mW}$, the wake mode instability occurs. This limit increases when the output coupling ratio t_{oc} increases. When $L_{\text{EDF}} = 25.0 \text{ cm}$ and $t_{\text{oc}} = 15\%$, the allowed power for the pump signal is less than 60 mW . The pump power threshold increases as t_{oc} increases. When $t_{\text{oc}} = 50\%$, the output comb remains stable

when P_{pump} equals 100 mW, leading to an average output power of 10.9 mW. Fixing $P_{\text{pump}} = 40$ mW and increasing t_{oc} from 15% to 50%, we find that the power efficiency η_{out} increases from 4.6% to 9.8%. The power efficiency continues to increase up to about 11% when P_{pump} increases to 100 mW, beyond which the wake mode instability occurs.

It is possible to improve the power efficiency by using a longer piece of erbium-doped fiber while lowering the pump power. However, this approach does not always lead to a higher average output power. As shown in Figs. 6.13(e) and (f), where $L_{\text{EDF}} = 32.5$ cm, the highest level of power efficiency that we can achieve is 12.7% when $t_{\text{oc}} = 50\%$ and $P_{\text{pump}} = 60$ mW. The wake mode instability occurs when P_{pump} further increases, corresponding to $P_{\text{out}} = 7.64$ mW, which is lower than the maximum average output power we can obtain when $L_{\text{EDF}} = 25.0$ cm, as shown in Fig. 6.13(c). A similar behavior occurs with other values of t_{oc} that we show in Figs. 6.13(e) and (f). Our simulations suggest that the length of the erbium-doped fiber should be increased to 25.0 cm and the output coupling ratio should be increased to 50%, in which case it should be possible to double the average output power and triple the power efficiency compared to the current experimental results.

6.4 Conclusions

In this chapter, we have carried a computational study to optimize the cavity design of a SESAM fiber comb laser. The goal was to increase the average output power and shorten the output pulse duration while suppressing the wake mode side-

bands. We have found that by increasing the output coupling ratio, the unsaturated gain, and the negative group delay dispersion, we can obtain a pulse that is 5 times more energetic and 10% shorter in duration than the observed experimental results while the sidebands in the PSD remain below 5 dB above the background noise level.

Combined with the simulations that have been done in [81], we find that increasing the output coupling ratio can both increase the average output power and decrease the wall-plug power of comb sources. In laser design, going back to the earliest lasers, it is usually assumed that it is desirable to keep the output coupling low in order to maximize the intra-cavity power and make good use of the gain medium. However, in a fiber laser, large intra-cavity power can lead to instabilities that are avoided by reducing the gain fiber length, which leads to under-utilization of the pump and poor power efficiency. From the standpoint of power efficiency, it is better in these cases to increase the gain fiber length and the output coupling. That is the case for the SESAM laser that we studied here.

CHAPTER 7

Conclusion

Modelocked lasers have been, and will continue to be an important optical source for frequency combs. Accelerating the design and optimization process has become increasingly important in product development. In this dissertation, we have conducted research that is aimed at facilitating the design and optimization of modelocked lasers. We have developed dynamical methods that can greatly improve the computational efficiency compared to the traditional evolutionary simulation approaches.

The theoretical background of the dynamical methods is dynamical system theory. We have developed boundary tracking algorithms to determine the regions of stable operation of a modelocked laser model rapidly and unambiguously in a large range of parameter space. By treating the stationary pulse solution of a modelocked laser as a fixed point in a nonlinear system, we can utilize well-developed root-finding algorithms, and we can use standard eigen-analysis routines to determine the stability of the modelocked pulses. We have applied the boundary tracking algorithm to multiple laser models, and we have found rich dynamical structures.

These results can provide significant insights into the instability mechanisms of these modelocked laser systems.

As an extension of this approach, we developed a dynamical method to determine the output noise of modelocked laser systems. By treating the noise source as perturbations, we can decompose the noise sources into eigenmodes of the linearized system, each of which has a simple evolution Langevin equation that can be solved analytically. Statistical quantities of interest like the timing phase jitter or the power spectral density of the amplitude and phase noise can then be evaluated accurately and rapidly. Compared to the widely used Monte Carlo method, the dynamical method is more than 1000 times faster and uses fewer computing resources, making it possible to evaluate statistical quantities of interest within minutes on a desktop computer. This approach should make it possible to design optimized laser sources much more quickly.

To date, the dynamical methods that we have developed are based on averaged models. At this point, one can think seriously about how to extend this approach to lumped models to provide a better connection to experimental parameters—especially those of the gain medium. In this case, the equilibrium solution will not be stationary as it passes through the laser in one round trip; it will only be periodically stationary. Thus, it is necessary to perform root-finding, linearization, and eigen-analysis on a periodic system. Holzlöhner et al. [82] and Deconninck and Kutz [83] have discussed algorithms for carrying out this task. However, more work needs to be done to adapt this approach for use in laser design.

Appendix A: Variables

Notation	Page	Definition
A_0	62	Peak amplitude of u
c_j	68	The amplitude of perturbation j
C	19	A stability boundary
D	67	Autocorrelation coefficient of S
f	40	Frequency
\mathbf{e}	66	An eigenvector of \hat{L}_0
$\hat{\mathbf{e}}$	67	An eigenvector of \hat{L}_0^\dagger

f_0	12	Unsaturable absorption coefficient of a saturable absorber
f_{ab}	12	Saturable absorption function
f_c	70	Central frequency
f_{decay}	56	Decay rate of the wake mode sidebands in T
f_{sa}	4	Nonlinear gain of fast saturable absorption
f_{sb}	58	Frequency offset of the wake mode sidebands from a comb tooth
g	3	Saturated gain coefficient
\hat{g}	38	Saturated gain operator
g^*	38	Gain coefficient of erbium-doped fiber
g_0	4	Unsaturated gain
h, \hbar	77	Planck's constant
h_x, \mathbf{h}_x	69	A statistical quantity of interest and its corresponding vector
j	66	An integer used in a counting scheme
k	67	An integer used in a counting scheme

l	68	Linear background loss coefficient
L_0	15	Linearized operator in its matrix form
L_{EDF}	36	Length of a section of erbium-doped fiber
n	39	Normalized lower-state population of the SESAM
n_2	38	Normalized upper-state population in erbium-doped fiber
N	65	Number of points in discretization
P_{ab}	12	Saturation power of a saturable absorber
P_{av}	4	Average power
P_k	38	Signal power of k th channel in erbium-doped fiber
P_{out}	59, 91	Average output power of the SESAM fiber comb laser
P_{pump}	47	Pump power of erbium-doped fiber
P_{sat}	4	Saturation power of the gain medium
r_x	74	The growth coefficient in a Gordan process
$R_{jk}(T)$	69	The cross-correlation of $c_j(T)$ and $c_k(T)$

$s(t, T)$	61	The added ASE noise over each round trip
$s_j(T)$	61	The amplitude of $\mathbf{s}(T)$ that is projected in direction \mathbf{e}_j
$S_x(f)$	61	The power spectral density of the stationary random process $x(T)$
t	3	Retarded time
t_c	3	Centroid time of a pulse
t_{oc}	91	Output coupling ratio of the SESAM laser
t_s	3	Shift of u in t over each roundtrip
T_w	42	Width of computational time window
T	3	Slow time of propagation
T_A	5	Response time of the SESAM
T_R	2	Roundtrip time of the laser cavity
u and \mathbf{u}	3, 15	Complex electric field envelope and its vector form
u_0	14	u as a part of a stationary solution
\mathbf{u}^H	67	The complex conjugate transpose of \mathbf{u}

Δu and $\Delta \bar{u}$	15	Perturbations to u_0 and u_0^*
Δv and Δw	24	Perturbations to u_0 and u_0^* , linear combinations of Δu and $\Delta \bar{u}$
w_A	36	Saturation energy of a SESAM
x^*	14	The complex conjugate of variable x
x_n	4	Normalized quantity x
$\tilde{\omega}$	9	The frequency domain representation of x
z	37	Propagation distance in the fiber
α	38	Absorption due to material absorption
β_2	38	Group velocity dispersion coefficient
β''	3	Group delay dispersion
γ	3	Kerr nonlinearity coefficient
δ	3	Cubic coefficient of fast saturable absorption
Δt	65	Interval of t in discretization
$\delta(x)$	67	Dirac δ -function in x

δ_{jk}	67	Kronecker δ -function
η	42	Conversion efficiency of a photodetector
η_{out}	108	Power efficiency of the SESAM fiber comb laser
ζ	39	Erbium-doped fiber saturation parameter
$\theta(t)$	62	Optical phase
$\Theta(t)$	69	Heaviside step-function
λ	15	Growth rate of perturbations, eigenvalues of \hat{L}_0
μ and ν	13	Coefficients in fiber-based fast saturable absorption models
ρ	39	Saturable absorption of a SESAM
σ	4	Quintic coefficient of the fast saturable absorber
ϕ	4	Phase rotation per unit T
$\Delta\psi$	71	Timing phase noise
ω_g	4	Gain bandwidth
τ_p	2	Duration of a pulse

Bibliography

- [1] B. R. Washburn, R. W. Fox, N. R. Newbury, J. W. Nicholson, K. Feder, P. S. Westbrook, and C. G. Jørgensen, “Fiber-laser-based frequency comb with a tunable repetition rate,” *Opt. Express* **12**, 4999–5004 (2004).
- [2] N. R. Newbury and B. R. Washburn, “Theory of the frequency comb output from a femtosecond fiber laser,” *IEEE J. Quantum Electron.* **41**, 1388–1402 (2005).
- [3] C. Cihan, E. Beyatli, F. Canbaz, L. J. Chen, B. Sumpf, G. Erbert, A. Leitenstorfer, F. X. Kärtner, A. Sennaroglu, and U. Demirbas, “Gain-matched output couplers for efficient kerr-lens mode-locking of low-cost and high-peak power cr:l:saf lasers,” *IEEE J. Sel. Top. Quant. Electron.* **21**, 94–105 (2015).
- [4] R. Paschotta, “Noise of mode-locked lasers (Part I): Numerical model,” *Appl. Phys. B* **79**, 153–162 (2004).
- [5] F. Kärtner, U. Morgner, T. Schibli, R. Ell, H. A. Haus, J. Fujimoto, and E. Ippen, “Few-cycle pulses directly from a laser,” in “Few-Cycle Laser Pulse Generation and Its Applications,” F. Kärtner, ed. (Springer, 2004).

- [6] M. E. Fermann, “Ultrafast fiber oscillators,” in “Ultrafast Lasers: Technology and Applications,” M. E. Fermann, A. Galvanauskas, and G. Sucha, eds. (Marcel Dekker Incorporated, 2002).
- [7] N. N. Akhmediev, J. M. Soto-Crespo, and P. Grelu, “Roadmap to ultra-short record high-energy pulses out of laser oscillators,” *Phys. Lett. A* **372**, 3124–3128 (2008).
- [8] J. M. Soto-Crespo, N. N. Akhmediev, and V. V. Afanasjev, “Stability of the pulselike solutions of the quintic complex Ginzburg-Landau equation,” *J. Opt. Soc. Am. B* **13**, 1439–1449 (1996).
- [9] H. Haus and A. Mecozzi, “Noise of mode-locked lasers,” *IEEE J. Quantum Electron.* **29**, 983–996 (1993).
- [10] S. Wang, A. Docherty, B. S. Marks, and C. R. Menyuk, “Boundary tracking algorithms for determining the stability of mode-locked pulses,” *J. Opt. Soc. Am. B* **31**, 2914–2930 (2014).
- [11] C. R. Menyuk and S. Wang, “Spectral methods for determining the stability and noise performance of passively modelocked lasers,” *Nanophotonics* **5**, 332–350 (2016).
- [12] S. A. Diddams, A. Bartels, T. M. Ramond, C. W. Oates, S. Bize, E. A. Curtis, J. C. Bergquist, and L. Hollberg, “Design and control of femtosecond lasers for optical clocks and the synthesis of low-noise optical and microwave signals,” *IEEE J. Sel. Top. Quantum Electron.* **9**, 1072–1080 (2003).

- [13] S. A. Diddams, “The evolving optical frequency comb,” *J. Opt. Soc. Am. B* **27**, B51–B62 (2010).
- [14] J. Ye and S. Cundiff, *Femtosecond Optical Frequency Comb: Principle, Operation and Applications* (Springer, 2006).
- [15] T. Kapitula, J. N. Kutz, and B. Sandstede, “Stability of pulses in the master mode-locking equation,” *J. Opt. Soc. Am. B* **19**, 740–746 (2002).
- [16] J. N. Kutz, “Mode-locked soliton lasers,” *SIAM Review* **48**, 629–678 (2006).
- [17] F. X. Kärtner, J. A. der Au, and U. Keller, “Mode-locking with slow and fast saturable absorbers—what’s the difference?” *IEEE J. Sel. Top. Quantum Electron.* **4**, 159–168 (1998).
- [18] H. A. Haus, “Theory of mode locking with a fast saturable absorber,” *J. Appl. Phys.* **46**, 3049–3058 (1975).
- [19] H. A. Haus, “Theory of mode locking with a slow saturable absorber,” *IEEE J. Quantum Electron.* **11**, 736–746 (1975).
- [20] N. R. Newbury and B. R. Washburn, “Theory of the frequency comb output from a femtosecond fiber laser,” *IEEE J. Quantum Electron.* **41**, 1388–1402 (2005).
- [21] S. Yefet and A. Peér, “A review of cavity design for Kerr lens mode-locked solid-state lasers,” *Appl. Sci.* **3**, 694 (2013).

- [22] C. G. Durfee, T. Storz, J. Garlick, S. Hill, J. A. Squier, M. Kirchner, G. Taft, K. Shea, H. Kapteyn, M. Murnane, and S. Backus, “Direct diode-pumped Kerr-lens mode-locked Ti:sapphire laser,” *Opt. Express* **20**, 13677–13683 (2012).
- [23] L. C. Sinclair, I. Coddington, W. C. Swann, G. B. Rieker, A. Hati, K. Iwakuni, and N. R. Newbury, “Operation of an optically coherent frequency comb outside the metrology lab,” *Opt. Express* **22**, 6996–7006 (2014).
- [24] D. Popa, Z. Sun, T. Hasan, W. B. Cho, F. Wang, F. Torrisi, and A. C. Ferrari, “74-fs nanotube-mode-locked fiber laser,” *Appl. Phys. Lett.* **101**, 17–19 (2012).
- [25] S. Husaini and R. G. Bedford, “Graphene saturable absorber for high power semiconductor disk laser mode-locking,” *Appl. Phys. Lett.* **104**, 161107 (2014).
- [26] H. A. Haus, “Mode-locking of lasers,” *IEEE J. Sel. Top. Quant.* **6**, 1173–1185 (2000).
- [27] S. Strogatz, *Nonlinear Dynamics and Chaos: With Applications to Physics, Biology, Chemistry and Engineering* (Perseus Books, 1994).
- [28] L. Landau and E. Lifshitz, *Fluid Mechanics* (Butterworth-Heinemann, 1987). Translated from Russian.
- [29] L. Landau, E. Lifshitz, and L. Pitaevskiĭ, *Electrodynamics of Continuous Media* (Butterworth-Heinemann, 1995). Translated from Russian.
- [30] A. Chong, J. Buckley, W. Renninger, and F. Wise, “All-normal-dispersion femtosecond fiber laser,” *Opt. Express* **14**, 10095–10100 (2006).

- [31] S. Wang, B. S. Marks, and C. R. Menyuk, “Comparison of models of fast saturable absorption in passively modelocked lasers,” *Opt. Express* **24**, 20228–20244 (2016).
- [32] H. A. Haus, “Theory of mode locking with a fast saturable absorber,” *J. Appl. Phys.* **46**, 3049–3058 (1975).
- [33] C.-J. Chen, P. K. A. Wai, and C. R. Menyuk, “Soliton fiber ring laser,” *Opt. Lett.* **17**, 417–419 (1992).
- [34] H. Leblond, M. Salhi, A. Hideur, T. Chartier, M. Brunel, and F. Sanchez, “Experimental and theoretical study of the passively mode-locked ytterbium-doped double-clad fiber laser,” *Phys. Rev. A* **65**, 063811 (2002).
- [35] A. Komarov, H. Leblond, and F. Sanchez, “Multistability and hysteresis phenomena in passively mode-locked fiber lasers,” *Phys. Rev. A* **71**, 053809 (2005).
- [36] A. Komarov, H. Leblond, and F. Sanchez, “Quintic complex Ginzburg-Landau model for ring fiber lasers,” *Phys. Rev. E* **72**, 025604 (2005).
- [37] S. Wang, A. Docherty, B. S. Marks, and C. R. Menyuk, “Comparison of numerical methods for modeling laser mode locking with saturable gain,” *J. Opt. Soc. Am. B* **30**, 3064–3074 (2013).
- [38] D. J. Kaup, “Perturbation theory for solitons in optical fibers,” *Phys. Rev. A* **42**, 5689–5694 (1990).

- [39] T. Kapitula, J. N. Kutz, and B. Sandstede, “The Evans function for nonlocal equations,” *Indiana Univ. Math. J.* **53**, 1095–1126 (2004).
- [40] S. Wang, B. S. Marks, and C. R. Menyuk, “Nonlinear stabilization of high-energy and ultrashort pulses in passively modelocked lasers,” *J. Opt. Soc. Am. B* **33**, 2596–2601 (2016).
- [41] N. N. Akhmediev and A. Ankiewicz, *Dissipative Solitons* (Springer, 2005).
- [42] V. V. Afanasjev, “Soliton singularity in the system with nonlinear gain,” *Opt. Lett.* **20**, 704–706 (1995).
- [43] M. Y. Sander, J. Birge, A. Benedick, H. M. Crespo, and F. X. Kärtner, “Dynamics of dispersion managed octave-spanning titanium:sapphire lasers,” *J. Opt. Soc. Am. B* **26**, 743–749 (2009).
- [44] T. Fortier, D. Jones, J. Ye, and S. Cundiff, “Highly phase stable mode-locked lasers,” *IEEE J. Sel. Top. Quantum Electron.* **9**, 1002–1010 (2003).
- [45] F. Kärtner, I. Jung, and U. Keller, “Soliton mode-locking with saturable absorbers,” *IEEE J. Sel. Top. Quantum Electron.* **2**, 540–556 (1996).
- [46] S. Wang, C. R. Menyuk, L. Sinclair, I. Coddington, and N. R. Newbury, “Soliton wake instability in a SESAM modelocked fiber laser,” in “CLEO: 2014,” (Optical Society of America, 2014), p. SW3E.4.

- [47] S. Wang, S. Droste, L. C. Sinclair, I. Coddington, N. R. Newbury, T. F. Caruthers, and C. R. Menyuk, “Wake mode sidebands and instability in mode-locked lasers with slow saturable absorbers,” *Opt. Lett.* **42**, 2362–2365 (2017).
- [48] “PM erbium-doped singlemode fiber,” www.opto-works.co.jp/specialityfibre/PM%20EDF.pdf. Accessed: 2017-08-01.
- [49] “SAMTM data sheet SAM-1550-21-2ps-x, $\lambda = 1550$ nm,” <http://www.batop.com/products/saturable-absorber/saturable-absorber-mirror/saturable-absorber-mirror-1550nm.html>.
- [50] O. V. Sinkin, R. Holzlöhner, J. Zweck, and C. R. Menyuk, “Optimization of the split-step fourier method in modeling optical-fiber communications systems,” *J. Lightwave Technol.* **21**, 61 (2003).
- [51] C. R. Giles and E. Desurvire, “Modeling erbium-doped fiber amplifiers,” *J. Lightwave Technol.* **9**, 271–283 (1991).
- [52] R. M. Mu, V. S. Grigoryan, C. R. Menyuk, G. M. Carter, and J. M. Jacob, “Comparison of theory and experiment for dispersion-managed solitons in a recirculating fiber loop,” *IEEE J. Sel. Top. Quantum Electron.* **6**, 248–257 (2000).
- [53] Y. Hu, B. S. Marks, C. R. Menyuk, V. J. Urick, and K. J. Williams, “Modeling sources of nonlinearity in a simple p-i-n photodetector,” *J. Lightwave Technol.* **32**, 3710–3720 (2014).

- [54] K. J. Williams, R. D. Esman, and M. Dagenais, “Nonlinearities in p-i-n microwave photodetectors,” *J. Lightwave Technol.* **14**, 84–96 (1996).
- [55] “Spectrum Analysis Basics—Application Note 150,” <http://www.keysight.com/main/editorial.jsp?cc=US&lc=eng&ckey=459160&id=459160&cmpid=zzfindappnote150>. Accessed: 2017-08-04.
- [56] C. Rauscher, *Fundamentals of Spectrum Analysis* (Rohde & Schwarz, 2001).
- [57] T. W. Parks and C. Burrus, *Digital Filter Design* (Wiley, 1987).
- [58] S. Wang, C. R. Menyuk, S. Droste, L. Sinclair, I. Coddington, and N. R. Newbury, “Wake mode sidebands and instability in comb lasers with slow saturable absorbers,” in “CLEO 2016,” (Optical Society of America, 2016), p. SM3H.5.
- [59] “High performance computing facility: System description,” <http://hpcf.umbc.edu/system-description/>. Accessed: 2017-10-26.
- [60] L. Sinclair, I. Coddington, W. C. Swann, and N. R. Newbury, “Stabilization of the offset frequency of an all polarization-maintaining fiber Erbium frequency comb,” in “CLEO: 2013,” (Optical Society of America, 2013), p. CTu1I.5.
- [61] U. Keller, K. J. Weingarten, F. X. Kartner, D. Kopf, B. Braun, I. D. Jung, R. Fluck, C. Honninger, N. Matuschek, and J. A. der Au, “Semiconductor saturable absorber mirrors (SESAM’s) for femtosecond to nanosecond pulse generation in solid-state lasers,” *IEEE J. Sel. Top. Quantum Electron.* **2**, 435–453 (1996).

- [62] Y. Shen, J. Zweck, S. Wang, and C. R. Menyuk, “Spectra of short pulse solutions of the cubic-quintic complex Ginzburg-Landau equation near zero dispersion,” *Stud. Appl. Math.* **137**, 238–255 (2016).
- [63] Y. Song, C. Kim, K. Jung, H. Kim, and J. Kim, “Timing jitter optimization of mode-locked Yb-fiber lasers toward the attosecond regime,” *Opt. Express* **19**, 14518–14525 (2011).
- [64] L. Nugent-Glandorf, T. A. Johnson, Y. Kobayashi, and S. A. Diddams, “Impact of dispersion on amplitude and frequency noise in a Yb-fiber laser comb,” *Opt. Lett.* **36**, 1578–1580 (2011).
- [65] H. A. Haus and Y. Lai, “Quantum theory of soliton squeezing: A linearized approach,” *J. Opt. Soc. Am. B* **7**, 386–392 (1990).
- [66] J. N. Kutz and B. Sandstede, “Theory of passive harmonic mode-locking using waveguide arrays,” *Opt. Express* **16**, 636–650 (2008).
- [67] R. Paschotta and U. Keller, “Passive mode locking with slow saturable absorbers,” *Appl. Phys. B* **73**, 653–662 (2001).
- [68] W. H. Renninger, A. Chong, and F. W. Wise, “Dissipative solitons in normal-dispersion fiber lasers,” *Phys. Rev. A* **77**, 023814 (2008).
- [69] M. J. Ablowitz, T. P. Horikis, S. D. Nixon, and D. J. Frantzeskakis, “Dark solitons in mode-locked lasers,” *Opt. Lett.* **36**, 793–795 (2011).

- [70] S. Wang, B. S. Marks, and C. R. Menyuk, “Comparison of models of fast saturable absorption in passively modelocked lasers,” *Opt. Express* **24**, 20228–20244 (2016).
- [71] J. Werner and T. P. Lee, “Monte Carlo simulation of mode-locked semiconductor diode lasers,” *Appl. Phys. Lett.* **57**, 1236–1238 (1990).
- [72] O. Hess and T. Kuhn, “Spatio-temporal dynamics of semiconductor lasers: Theory, modelling and analysis,” *Prog. Quantum Electron.* **20**, 85–179 (1996).
- [73] P. Qin, S. Wang, M. Hu, and Y. Song, “Effective removal of gordon-haus jitter in mode-locked fiber lasers,” *IEEE Photonics J.* **10**, 1500208 (2017).
- [74] L. Trefethen and D. Bau, *Numerical Linear Algebra* (SIAM, 1997).
- [75] A. Docherty, C. R. Menyuk, J. P. Cahill, O. Okusaga, and W. Zhou, “Rayleigh-scattering-induced RIN and amplitude-to-phase conversion as a source of length-dependent phase noise in OEOs,” *IEEE Photonics J.* **5**, 5500514 (2013).
- [76] P. K. A. Wai and C. R. Menyuk, “Polarization mode dispersion, decorrelation, and diffusion in optical fibers with randomly varying birefringence,” *J. Lightwave Technol.* **14**, 148–157 (1996).
- [77] V. S. Grigoryan, C. R. Menyuk, and R. M. Mu, “Calculation of timing and amplitude jitter in dispersion-managed optical fiber communications using linearization,” *J. Lightwave Technol.* **17**, 1347–1356 (1999).

- [78] J. A. Weideman and S. C. Reddy, “A matlab differentiation matrix suite,” *ACM Trans. Math. Softw.* **26**, 465–519 (2000).
- [79] C. Menyuk, S. Wang, and T. Carruthers, “A dynamical perspective on noise in passively modelocked lasers,” in “Frontiers in Optics 2017,” (Optical Society of America, 2017), p. JTu3A.57.
- [80] S. Wang, T. F. Carruthers, and C. R. Menyuk, “Efficiently modeling the noise performance of short-pulse lasers with a computational implementation of dynamical methods,” *J. Comput. Phys.* **xx**, xxxx–xxxx (2018).
- [81] S. Wang, C. R. Menyuk, S. Droste, L. Sinclair, I. R. Coddington, and N. Newbury, “Optimizing the power efficiency of a sesam fiber comb laser,” in “CLEO 2017,” (Optical Society of America, 2017), p. SF1C.2.
- [82] R. Holzlohner, C. R. Menyuk, W. L. Kath, and V. S. Grigoryan, “A covariance matrix method to compute bit error rates in a highly nonlinear dispersion-managed soliton system,” *IEEE Photon. Technol. Lett.* **15**, 688–690 (2003).
- [83] B. Deconinck and J. N. Kutz, “Computing spectra of linear operators using the Floquet Fourier Hill method,” *J. Comput. Phys.* **219**, 296–321 (2006).

